X-RAY ROCKING CURVE AND FERROMAGNETIC RESONANCE INVESTIGATIONS OF ION-IMPLANTED CRYSTALS

Thesis by

Virgil S. Speriosu

In Partial Fulfillment of the Requirements

for the Degree of

Doctor of Philosophy

California Institute of Technology

Pasadena, California

1983

(Submitted January , 1983)

Considerate la vostra semenza:
Fatti non foste a viver come bruti,
Ma per seguir virtude e conoscenza.

Dante

Acknowledgements

During my two and a half years of apprenticeship with Chuck Wilts, he has taught me some things that go beyond the details of magnetism. Simply by watching him I have learned the usefulness of the following attitudes. First, make sure you have done your experiment correctly. Second, have the honesty to accept what it says, no matter how weird it may sound at first. Third, have faith that there is an explanation and do not easily give up looking for it.

I thank Tom Kobayashi for introducing me to ion implantation in garnet and for trusting in me at a time when few others were willing to go that far. Howard Glass taught me much of what I know of x-ray diffraction. He and Lavada Moudy are largely responsible for the easy access I have had to one of Rockwell International's laboratories. I thank Chris Bajorek of the International Business Machines Corporation for considering me worthy of a predoctoral fellowship, and I thank Bob Scranton for its renewal. Tim Gallagher, Kochan Ju and H. Ben Hu of IBM supplied the samples for and encouraged a large part of this thesis. Jim Campbell suggested the use of and provided us with an HP 9826 computer.

I thank Professor M-A. Nicolet for his interest in the x-ray rocking curve method, for encouraging its application to semiconductors, and for pointing out the most promising

area for this application. The expertise of Bruce Paine and Leszek Wielunski in ion implantation and Rutherford back-scattering has added considerably to this thesis. Joyce Lidell and Michell Parks have typed the papers presented here. My wife Michelle did little typing but much encouraging.

Finally, I thank my parents. As far as I am concerned, it all started with them.

Abstract

A kinematical model for general Bragg case x-ray diffraction in nonuniform films is presented. The model incorporates depth-dependent strain and structure factor. For ion-implanted crystals the change in structure factor attributed to damage is calculated using a spherically symmetric Gaussian distribution of incoherent atomic displacements. Profiles of strain and structure factor are obtained by fitting experimental rocking curves. The method is applicable to ion-implanted, diffused and multilayer crystalline structures such as heterojunctions and superlattices.

A comparison is made between profiles of strain and incoherent atomic displacements obtained from rocking curves and from Rutherford backscattering spectrometry in a $Gd_3Ga_5O_{12}$ crystal implanted with 100 keV Ne^+. The ranges of sensitivity of the two techniques overlap for about one decade in implantation dose up to the amorphous threshold. X-ray diffraction was found to be most sensitive to low damage levels while backscattering was found to be most sensitive to high damage levels. The two techniques are in excellent agreement on the near-surface strain, but differ significantly at depths below ≈500A. The discrepancy is attributed to errors caused by steering of channelled particles in backscattering spectrometry. The profiles of number of displaced atoms agree within a factor of two.

The rocking curve method is combined with analysis of ferromagnetic resonance (FMR) spectra for characterization of crystalline and magnetic properties of [111]-oriented Gd,Tm,Ga:YIG films implanted with Ne^+, He^+, and H_2^+. For each implanted species the range of doses begins with easily-analyzed effects and ends with paramagnetism or amorphousness. Profiles of normal strain, lateral strain and damage were obtained. For maximum strains up to 1.3% the behavior of the strain with annealing is nearly independent of implanted species or dose. Magnetic profiles obtained before and after annealing were compared with the strain profiles. The local change in uniaxial anisotropy field ΔH_k with increasing strain shows an initially linear rise for both He^+ and Ne^+, in quantitative agreement with the magnetostriction effect estimated from the composition. For strain values between 1% and 1.5%, ΔH_k saturates and for increasing strain, ΔH_k decreases to nearly zero when the material becomes paramagnetic. For peak strains greater than 1.3% for He^+ and 1.1% for Ne^+ the relation between uniaxial anisotropy and strain is not unique. Behavior of the saturation magnetization $4\pi M$, the exchange constant A and the cubic anisotropy H_1 was elucidated. For H_2^+ implantation the total ΔH_k consists of a magnetostrictive contribution due to strain and of a comparable excess contribution associated with the local concentration of hydrogen. The profile of excess ΔH_k agrees with calculated LSS range. The presence of hydrogen results in a reduction of $4\pi M$ not attributable to strain or damage. With increasing

annealing temperature the excess ΔH_k diminishes and above 400°C the only component of ΔH_k is magnetostrictive.

Crystalline properties of Si-implanted [100] GaAs, Si, and Ge were studied by the rocking curve method. Sharp qualitative and quantitative differences were found between the damage in GaAs on one hand and Si and Ge on the other. At a moderate damage level the GaAs crystal undergoes a transition from elastic to plastic behavior. The plastically deformed region presents a barrier to epitaxial regrowth and is consistent with the well-known high defect density in regrown GaAs.

Table of Contents

Chapter I

Introduction

The contents of this thesis are addressed to specialists in x-ray diffraction and ferromagnetic resonance, especially as the latter may be applied to the study of ion-implanted crystals. Some of the results are of immediate interest to manufacturers of devices using magnetic garnet as host material. There is no need to include an introductory description of garnets, semiconductors, magnetism, ion implantation, x-ray diffraction or ferromagnetic resonance since these are well treated in textbooks and the references cited in the following chapters. Instead this will present my own modest contributions to these areas. As will be evident in the following chapters, I am the sole author of only one of the papers. I have the pleasure to acknowledge again the active participation of my advisor, Professor C.H. Wilts, and of other collaborators whose efforts made this thesis possible.

The most important development presented here is in the area of x-ray diffraction in monocrystals with properties that may vary with depth. The double-crystal, Bragg case, rocking curve method is well suited for measuring the structural properties of such crystals. In this method a beam of x-rays is collimated, partially polarized and rendered nearly monochromatic by diffraction in a stationary first crystal. The

beam then impinges on the crystal to be studied and following diffraction emerges at the same surface. This distinguishes the Bragg case from the Laue case where the diffracted beam exits through a different surface. The sample crystal is rotated finely about the Bragg condition while the diffracted intensity is measured. The diffracted intensity normalized to that of the incident beam is the reflecting power; the reflecting power vs. angle is the rocking curve. For thick, nearly perfect crystals one must consider the multiplicity of scattering of x-rays before they emerge from the crystal. This has been successfully treated by the dynamical theory. In nearly perfect crystals whose properties nevertheless vary with depth, the dynamical calculation is rather complicated. My contribution consists of the realization that for most monocrystals of technological importance the diffraction of x-rays is described with sufficient accuracy by the kinematical (single-scattering) theory. The mathematical simplicity of this theory (see Chapter II) has enabled me to use the rocking curve method more extensively than anyone else for the study of ion-implanted crystals. The displacements of target atoms due to interactions with the ion beam are separable into coherent and incoherent components. The coherent component is a deformation of the unit cell (strain), while the incoherent component (damage) changes the value of the structure factor. In ion-implanted crystals the strain and damage vary with depth, producing an oscillatory rocking curve whose angular extent is typically about one degree.

For thick perfect crystals the range of nonzero reflecting power is measured in arcseconds. By using a computer to fit experimental rocking curves I have obtained strain and damage profiles for various crystals implanted with a range of species, energies, and doses. Chapter II gives the derivation of the equations used in the calculation and several examples of the method applied to ion-implanted garnets. The chapter is unchanged from its published form and suffers from inadequate treatment of the relation between damage and strain. For the helium implantations studied in this chapter the damage is too low for an accurate determination of its profile, and hence the linearity between damage and strain is overstated. This matter was treated more carefully in subsequent work reported in Chapter IV, where the linearity between damage and strain was established more strongly through use of more highly damaged crystals.

In addition to ion-implanted monocrystals, the rocking curve method and the kinematical interpretation of the rocking curve are applicable to the characterization of crystals modified by diffusion and to epitaxial multilayer structures such as heterojunctions and superlattices. Although such applications are not described in detail an example is included in which the strain profile was determined in order to match the published experimental rocking curve of such a structure. The authors of that paper, being unaware of the power of this method, did not attempt a

detailed interpretation of their data.

Until now Rutherford backscattering spectrometry has been the most frequently used tool for measuring damage in ion-implanted crystals. In perfect crystals for certain directions of incidence (channels) a well-collimated beam of high-energy α particles or protons can penetrate to several microns with very little deflection or backscattering. In a damaged crystal a fraction of the beam is backscattered. The backscattering yield is a measure of crystalline quality. This method has several advantages: it is nearly non-destructive, is experimentally easy and interpretation of experimental data is relatively straightforward. These advantages of Rutherford backscattering are shared by the x-ray rocking curve method, which is even more nearly non-destructive. In addition, the apparatus needed for x-ray measurements is much simpler than Van der Graaf or other accelerators and it is not necessary to do diffraction in vacuum. However, backscattering has gained wide acceptance while the rocking curve method is relatively unknown as a tool for measuring damage in implanted crystals. A comparison of the two methods in terms of sensitivity and richness of information might remedy this situation.

Such a comparison is made in Chapter III for a $Gd_3Ga_5O_{12}$ crystal implanted with neon ions with a dose range of one decade, the highest dose being sufficient to render the

crystal amorphous. The choice of this crystal was made because of the initial uncertainty concerning the overlap of the ranges of sensitivity for the two methods. It is now clear (Chapter V) that other crystals (Si, Ge, GaAs, InP, YIG, etc.) would have served as well, if not better. The comparison is made of the strain and damage profiles determined by the two techniques. For strain the x-ray method is superior in accuracy and detail; in fact the strain measured by backscattering is accurate only at the surface. For damage they are not easily compared because they measure different things: backscattering probes direct space while x-ray diffraction probes reciprocal space. Uncertainties in the radial distribution of the channelled beam and in the scattering potential introduce uncertainties in the number of displaced atoms deduced from backscattering yield. In x-ray diffraction a particular distribution of atomic displacements must at first be assumed in order to calculate the structure factor. Comparison of calculated and measured magnitudes of the structure factor then provides moments of the distribution of displacements. Thus the comparison of the numbers of displaced atoms obtained from backscattering yield and rocking curve requires that a number of reasonable assumptions be made. With such assumptions the two measures of damage agree within a factor of two, which suggests that both measures are in fact related to the real damage of the crystal.

A major portion of my thesis (Chapter IV) is concerned with magnetic properties of implanted garnet. These properties are the saturation magnetization $4\pi M$, the exchange stiffness A, the uniaxial and cubic anisotropies H_k and H_1, the gyromagnetic ratio γ, and the damping parameter α. All of these parameters are phenomenological, with meanings derived either directly from measurement or from their use in the Landau-Lifshitz equation. Despite their phenomenological nature, these parameters are essential for predicting the behavior of implanted systems such as bubble memories, filters or delay lines, and a comparison or correlation with strain and damage is significant. This provides information about the relative importance of dopant chemistry compared to strain and damage in the implanted lattice.

Magnetic properties of implanted garnets have been studied by several techniques, of which ferromagnetic resonance (FMR) is the most promising. The FMR spectra of such crystals can be very rich, with absorption peaks of varying amplitudes and occuring in a range of several thousand oersteds of applied magnetic field. For a given implanted element with increasing dose the number of detectable absorption peaks at first increases from one (virgin material) to a maximum of 10 or 15, and finally decreases to 5 or less. The amplitudes and locations of these peaks vary in a complex fashion with dose. The FMR spectrum is interpreted in terms of magnetic excitations called spinwaves whose local wave

equation is the linearized Landau-Lifshitz equation expanded to include the exchange interaction. The solutions of this eigenvalue equation provide mode amplitudes and values of applied field for resonance. If magnetic properties vary with depth in an arbitrary way, the equation becomes complicated and its solutions cannot be written in terms of the known closed-form functions. C.H. Wilts has recently developed a numerical method for calculating the spinwave spectrum of a material with depth-dependent properties. By matching calculated and experimental spectra, profiles of magnetic parameters can be obtained. Wilts has done this for low dose cases where the profiles are unimodal and the corresponding spectra are relatively easily interpreted. I have used this method to obtain magnetic properties at high damage levels, where the interpretation of the spectra is difficult. The solution of this problem was greatly facilitated by comparing the magnetic structure with the strain profiles obtained from x-ray diffraction. The detailed behavior of magnetic and crystalline properties with dose and annealing for neon, helium and hydrogen implantation is presented in Chapter IV. Without repeating this information, I can state here that many of the basic features of implanted garnet, as determined by combining x-ray and FMR techniques, are substantially different from the picture obtained with the less accurate methods used earlier.

It is well known that implantation and annealing conditions for optimum recrystallization and electrical characteristics of highly damaged ("amorphous") GaAs must be different from those used for Si and Ge. The prevailing explanation for the difference has been the loss of stoichiometry in GaAs due to differences in ion energy transfer to Ga versus As. According to this view the deep portion of the layer is Ga-enriched while the outer portion is As-enriched. However the difference seems too small to be the plausible source of poor regrowth. Other features, such as the insensitivity of the regrowth to implanted species and the initial high-quality regrowth at the interface with unimplanted material, have not been explained. Rutherford backscattering measurements have not shown any qualitative difference between the damage in GaAs on one hand and Si or Ge on the other. In Chapter V the rocking curve method is applied to Si-implanted GaAs, Si and Ge. Although the study is very brief, it is sufficient to show that with increasing dose the evolution of strain and damage in GaAs is qualitatively different from that in Si or Ge. The difference implies a different structure of the implanted layer in GaAs vs. Si or Ge. In GaAs the highly damaged outer region and the little damaged inner region are separated by a layer containing extended defects. The existence of this layer depends on the local strain regardless of the implanted species. The layer presents a barrier to epitaxial regrowth and is consistent with the observation of high defect density in regrown GaAs films.

Chapter II

Kinematical x-ray diffraction in nonuniform crystalline films

An expression for the reflecting power of nonuniform crystals is derived from the perfect crystal dynamical theory. Profiles of strain and damage in ion-implanted garnets and in an epitaxial multilayer structure are obtained by fitting experimental rocking curves.

Kinematical x-ray diffraction in nonuniform crystalline films: Strain and damage distributions in ion-implanted garnets

V. S. Speriosu[a)]
California Institute of Technology, Pasadena, California 91125

(Received 23 March 1981; accepted for publication 22 June 1981)

A kinematical model for general Bragg case x-ray diffraction in nonuniform films is presented. The model incorporates depth-dependent strain and spherically symmetric Gaussian distribution of randomly displaced atoms. The model is applicable to ion-implanted, diffused, and other single crystals. Layer thickness is arbitrary, provided maximum reflecting power is less than ~6%. Strain and random displacement (damage) distributions in He^+-implanted Gd, Tm, Ga:YIG, and Ne^+-implanted $Gd_3Ga_5O_{12}$ are obtained by fitting the model to experimental rocking curves. In the former crystal the layer thickness was 0.89 μm with strain varying between 0.09 and 0.91%. In the latter crystal a wide range of strain and damage was obtained using successively higher doses. In each case layer thickness was 1900 Å, with 2.49% strain corresponding to 0.40-Å standard deviation of random displacements. The strain distributions were strictly linear with dose. The same, closely linear relationship between damage and implantation-induced strain was determined for both crystals.

PACS numbers: 61.10. — i, 61.70. — r, 61.70.Tm

I. INTRODUCTION

Bragg case x-ray diffraction is a well-established method for characterizing crystalline properties of films obtained by various growth techniques. The diffracted intensity profiles (rocking curves) are highly sensitive to depth-dependent strain and damage distributions as well as lateral variations, but much of the information available in the rocking curves is generally not extracted. Part of the difficulty is due to lack of phase detection, which precludes direct inversion of the rocking curve. The remaining difficulty is the complexity of the dynamical theory of diffraction in nonuniform crystals.[1–3] At the cost of long computation time, strain profiles in diffused[4–6] and ion-implanted[7] layers were obtained by fitting dynamical theory calculations to experimental rocking curves.

The kinematical theory for symmetric reflections,[8] which involves much simpler mathematics, has offered a considerable reduction in computation time. The application[9] of the Patterson series[10] to this theory yielded parameters such as mean strain, damage, and layer thickness. In another approach, detailed strain and damage distributions were obtained by fitting a kinematical theory model to rocking curves of successively etched samples.[11,12] However, both approaches were limited to symmetric reflections which provide a limited amount of information.

In this paper a general Bragg case kinematical expression for the reflecting power of nonuniform films is obtained from the uniform single-crystal dynamical theory.[13] Depth-dependent strain distributions are represented by a set of independently but coherently diffracting laminae oriented parallel to the surface. Each lamina incorporates many unit cells and has uniform strain. In addition to coherent atomic displacements, random displacements (damage) are treated through their effect on the mean structure factor in each lamina. The range of validity of the kinematical approximation is shown to include most cases of technological importance. The relative sensitivity to strain, damage, and layer thickness is demonstrated. Using this model, strain and damage distributions are obtained by fitting rocking curves of He^+-implanted Gd, Tm, Ga:YIG, and Ne^+-implanted gadolinium gallium garnet (GGG). In the former crystal three different strain and damage distributions were created by single and multiple implantations. Rocking curves of symmetric and asymmetric reflections were fitted. The latter crystal was implanted with single doses resulting in a wide range of strain and damage. Symmetric reflection rocking curves corresponding to each dose were fitted.

II. THE KINEMATICAL MODEL

The plane-wave dynamical theory[13] predicts that for unit electric-field amplitude incident on the surface of an isolated, uniform, nonabsorbing, single-crystal plate, the diffracted amplitude at the same surface is

$$E_D = e^{-i2\pi(\mathbf{K}_0^e + \mathbf{B}_H)\cdot\mathbf{r}} D_D, \tag{1}$$

$$D_D = i\,\frac{F_H}{|F_H|}\sqrt{|b|}\times\frac{\sin\left[A\,(Y^2-1)^{1/2}\right]}{(Y^2-1)^{1/2}\cos\left[A\,(Y^2-1)^{1/2}\right]+iY\sin\left[A\,(Y^2-1)^{1/2}\right]}, \tag{2}$$

where the following definitions apply: $\mathbf{K}_0^e$ = incident external wavevector, $|\mathbf{K}_0^e| = 1/\lambda$, $\mathbf{B}_H$ = reciprocal lattice vector, $\mathbf{r}$ = vector from origin (chosen on the surface), F_H = structure factor, $b = \gamma_0/\gamma_H$; γ_0, γ_H are direction cosines of incident and diffracted wavevectors, respectively, from the inward normal to the surface;

$$A = \frac{e^2}{mc^2}\,\frac{\lambda\,|F_H|}{V}\,\frac{t}{(|\gamma_0\gamma_H|)^{1/2}}, \tag{3}$$

where e^2/mc^2 = classical electron radius, V = volume of

[a)]IBM predoctoral fellow.

 0021-8979/81/106094-10$01.10

unit cell, t = plate thickness,

$$Y = \frac{[(1-b)/2]\psi_0 + (b/2)\alpha}{(\sqrt{}|b|)|\psi_H|}, \tag{4}$$

$$\psi_{0,H} = -\frac{e^2}{mc^2}\frac{\lambda^2}{\pi}\frac{F_{0,H}}{V},$$

$$\alpha = -2\Delta\theta \sin 2\theta_B,$$

$$\Delta\theta = \theta - \theta_B,$$

θ_B = Bragg angle.

Equations (2)–(4) are valid only for σ polarization. For π polarization F_H is replaced by $F_H \cos 2\theta_B$.

If the plate thickness and/or the structure factor are sufficiently small, corresponding to $A \ll 1$, Eq. (2) reduces to the kinematical limit:

$$D_K = i\frac{F_H}{|F_H|}(\sqrt{}|b|)e^{-iAY}\frac{\sin(AY)}{Y}. \tag{5}$$

Equations (3) and (4) apply to unstrained and undamaged lattice. If the lattice is strained in a direction perpendicular to the sample surface, the corresponding change in Eq. (4) is

$$\Delta\theta \rightarrow \Delta\theta + \epsilon^{\perp}[|\gamma_H|(1-\gamma_H^2)^{1/2} + \gamma_H^2 \tan\theta_B]. \tag{6}$$

Here $\epsilon^{\perp}$ is the strain and the correction includes changes in the direction and magnitude of the reciprocal lattice vector. Equation (6) can be easily extended to include lateral strain. However, the requirement of lattice match between film and substrate generally does not allow lateral strain.

In ion-implanted crystals, a significant fraction of atoms may be displaced from lattice positions. The statistical distribution of displacements $\Delta\mathbf{r}_j$ away from lattice j is described by a function $\rho(\Delta\mathbf{r}_j)$. Such a distribution will result in a mean structure factor

$$\langle F_H\rangle = \sum_j f_j \int d^3r \rho(\Delta\mathbf{r}_j) e^{-i2\pi\mathbf{B}_H\cdot(\mathbf{r}_j+\Delta\mathbf{r}_j)}, \tag{7}$$

where f_j is the atomic scattering factor for site j, located at $\mathbf{r}_j$ in undamaged crystal. If the same spherically symmetric Gaussian form is assumed for all sites, the mean structure factor becomes

$$\langle F_H\rangle = \exp\left(-\frac{8\pi^2}{\lambda^2}\sin^2\theta_B U^2\right)F_H^0 = e^{-W}F_H^0, \tag{8}$$

where F_H^0 corresponds to undamaged crystal and U is the standard deviation of displacements. This correction to F_H^0 is the well-known Debye-Waller factor.[13] Its form can be readily modified for other $\rho(\Delta\mathbf{r}_j)$ distributions, but, for simplicity, in this paper a spherically symmetric Gaussian $\rho(\Delta\mathbf{r}_j)$ is assumed.

Strain and damage distributions are represented by a set of discrete laminae oriented parallel to the surface. Each lamina contains a large number of unit cells, but is sufficiently thin so that extinction[13] and normal absorption within the lamina are negligible. Each lamina has its own uniform strain $\epsilon^{\perp}$ and random displacement standard deviation U. Dynamical interactions among different laminae are neglected, as is the effect of extinction on the incident wave. The total diffracted amplitude is then the sum of coherently interfering functions of the type shown in Eq. (5), adjusted for phase lags and normal absorption during traversal through the crystal. Although usually extinction is stronger than normal absorption,[13] for depth-dependent strain distributions the latter can be more important. With these considerations, the total amplitude from N laminae is

$$E_N = i\frac{F_H}{|F_H|}(\sqrt{}|b|)\sum_{j=1}^{N} a_j e^{-i(A_jY_j+\phi_j)}\frac{\sin(A_jY_j)}{Y_j}, \tag{9}$$

where

$$a_j = \exp\left[-\mu\frac{\gamma_0+|\gamma_H|}{2|\gamma_0\gamma_H|}\sum_{i=j+1}^{N} t_i\right]; \quad a_N = 1,$$

$$\mu = \frac{2\lambda}{V}\frac{e^2}{mc^2}\,\mathrm{Im}\,(F_0),$$

t_i = thickness of lamina i,

$$\phi_j = 2\sum_{i=1}^{j-1} A_i Y_i; \quad \phi_1 = 0,$$

and the previously defined variables Y and A are now subscripted to indicate dependence on strain and damage. In addition, since Eq. (9) will be used to determine strain relative to virgin crystal, the refraction correction $[(1-b)/2]\psi_0$ in the definition of Y [Eq. (4)] is neglected.

In principle the total amplitude due to laminar structure and substrate is

$$E_T = E_N + a_1 e^{-i2A_1Y_1}E_s, \tag{10}$$

where E_s is the dynamical result for a thick, aborbing, perfect crystal. However, the observed rocking curves of thick, supposedly uniform crystals are frequently broader than predicted for perfect crystals. The discrepancy is due to lattice parameter variations and, to a lesser extent, Compton and thermal diffuse scattering. For the purpose of fitting rocking curves of thin surface layers, the discrepancy in the substrate intensity can be removed by using a function which matches it in the angular range of interest. In addition, the relatively wide substrate peak implies that its amplitude does not have a well-defined phase. Therefore, the total calculated intensity should be only the sum of layer and substrate intensities. The total reflecting power is

$$R_T = \frac{1+\cos^4 2\theta_B}{1+\cos^2 2\theta_B}\frac{|\gamma_H|}{\gamma_0}E_N E_N^* + R_s, \tag{11}$$

where the first factor represents the relative abundance of σ- and π-polarization in double-crystal diffractometry, $|\gamma_H|/\gamma_0$ relates intensity to power, and R_s is the substrate reflecting power.

Because of the approximations made in arriving at Eq.(11), it cannot be indiscriminately applied to films of arbitrarily large thickness. As thickness increases, particularly if the strain distribution is constant, dynamical effects become dominant. It is therefore important to consider the range of validity of the kinematical theory. For constant strain and $A \lesssim 0.25$, the kinematical [Eq. (5)] and dynamical [Eq. (2)] amplitudes are in extremely close agreement. The upper limit corresponds to about 6% reflecting power. For $0.25 \lesssim A \lesssim 1$, the kinematical expression yields a sharper and more peaked curve, but the discrepancy is not more than

~15%. Choosing 6% reflecting power as the upper limit of validity and considering only the strongest reflections, the corresponding layer thickness is 2000 – 4000 Å for crystals such as Si, Ge, GaAs, and magnetic garnet. This range is for constant strain. If the strain is depth-dependent, as is true of ion-implanted, diffused, and other films, the range of validity for the kinematical theory can be several times larger. Dynamical effects depend strongly on the Bragg condition, $Y = 0$, being satisfied throughout the layer; this does not happen in nonuniform films. Since the thickness for which the kinematical model is valid varies with the strain distribution, a definite upper limit cannot be given. However, the agreement with dynamical theory for $R_T \lesssim 6\%$ suggests that rocking curves with maxima up to this value can be safely interpreted kinematically. For typical distributions this value of R_T corresponds to ~1-μm total thickness.

III. ROCKING CURVE SENSITIVITY TO STRAIN, LAYER THICKNESS, AND DAMAGE

Expression (9) for the diffracted amplitude, taken to the integral limit, is proportional to the Fourier transform of the strain and damage distributions. However, the lack of phase detection precludes direct inversion of the rocking curve. The distributions can be obtained by fitting the rocking curve with Eq. (11) evaluated for assumed distributions. A good fit of the data is then taken to mean that the actual distributions were found. Since the validity of this assumption cannot be mathematically proved, it is useful to examine the rocking curve sensitivity to strain and damage. Figure 1(a) shows two strain distributions obtainable by He^+-implantation in garnet. The distributions are plotted versus distance from the interface with the unstrained substrate. The number of laminae is such that further subdivision does not affect the calculated rocking curve. The distributions have the same thickness but differ by $\pm 5\%$ in their detailed shapes, i.e., distribution 1 (dashed) is slightly sharper. It is assumed that there is no damage, i.e., $U_j \equiv 0$ for all laminae. The corresponding calculated rocking curves for Cu K_α (444) are shoown in Fig. 1(b). The structure in the range $-0.24 \text{ deg} \lesssim \Delta\theta \lesssim -0.04 \text{ deg}$ is entirely due to the strain distributions of Fig. 1(a). For $|\Delta\theta| \lesssim 0.03$ deg, the substrate reflecting power, obtained from dynamical theory, is dominant.

Although rocking curves 1 and 2 are qualitatively very similar, there are large differences in the positions of their maxima and minima. The differences indicate a high sensitivity to strain distribution and furnish the confidence that a distribution yielding a good fit of the data is not only unique, but also highly accurate. The accuracy depends on the particular strain distribution, and ranges from $\pm 5\%$ to $\pm 2\%$ strain for layer thicknesses between ~2000 Å and ~6000 Å.

Similar accuracy exists for the total strained layer thickness. For uniform strain, Eq. (5) relates the thickness to the period of oscillation. For depth-dependent strain, the period is no longer constant [see Fig. 1 (b)]. For positive strain, at a given $\Delta\theta$ it roughly measures the thickness for which the strain is greater than the value obtained by setting the right side of Eq. (6) equal to zero. For example, the period between -0.06 deg and -0.03 deg yields the total layer thickness in Fig. 1(a).

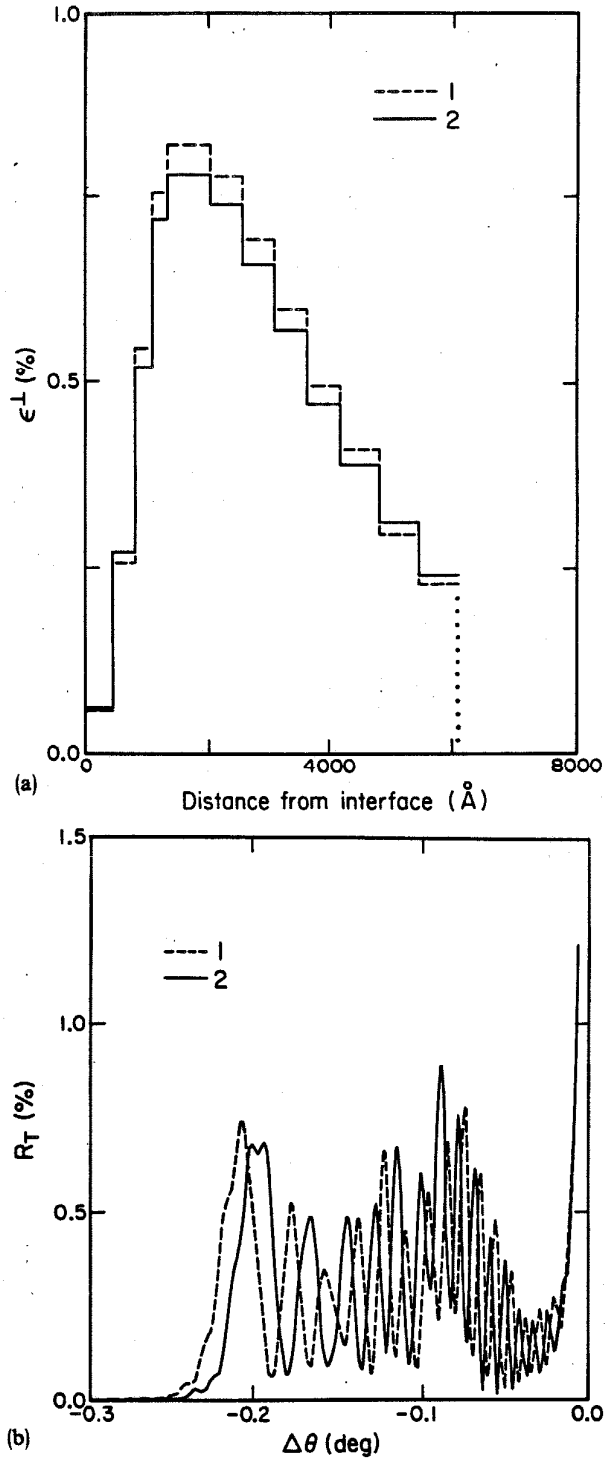

FIG. 1. (a) Strain distribution (dashed) obtainable by He^+-implantation in garnet. The solid line is a $\pm 5\%$ variation. The distributions are plotted vs distance from the interface with unstrained substrate. (b) Calculated Cu K_α (444) rocking curves corresponding to the strain distributions of Fig. 1(a). The angle $\Delta\theta$ is referred to the location of the substrate peak.

The theoretical sensitivity to the damage parameter U is considerably less than to strain and thickness. For uniform

strain and damage, the reflecting power goes as e^{-2W}, where W is proportional to U^2 [Eq. (8) and (11)]. From this

$$\Delta U \sim \frac{1}{U}\frac{\Delta R_T}{R_T} \tag{12}$$

so that for low U the relative uncertainty is quite large. At moderate to high damage levels the sensitivity improves, approaching that for strain.

IV. EXPERIMENT

A series of ⟨111⟩ Gd, Tm, Ga: YIG samples subjected to three He^+-implantation conditions was supplied by an external source.[14] The films were grown by LPE on 0.5-mm-thick Czochralski-grown ⟨111⟩ $Gd_3Ga_5O_{12}$ (GGG), were about 0.9 μm thick, and had a quoted composition $\{Gd_{0.84}Tm_{1.17}Y_{0.99}\}[Fe_2](Ga_{0.39}Fe_{2.61})O_{12}$. Implantation was done at room temperature, several degrees off ⟨111⟩ axis and with current densities of $\sim 0.1\ \mu A/cm^2$. The implantation conditions were 140 keV, 3×10^{15} He^+/cm^2 (denoted here as FI); FI + 70 keV, 1.4×10^{15} He^+/cm^2 (≡FII);FII + 30 keV, 9×10^{14} He^+/cm^2(≡FIII). According to a model[15] relating certain magnetic properties to nuclear energy loss, the three conditions should yield increasingly uniform properties with depth. For each implanation condition a series of samples was made by ion milling to successively greater depths. In addition, several duplicates of as-implanted samples were provided. The size of these samples was $\sim 4\times4$ mm^2.

As will be shown, the He^+ doses resulted in relatively low levels of damage. In order to explore the validity of the kinematical diffraction model over a wider range of damage, a series of GGG samples, provided by another source,[16] was implanted at room temperature with 100-keV Ne^+ at 0, 0.5, 1.0, 2.0, and 6.0×10^{14} atoms/cm^2. These samples will be denoted as PI through PV. The orientation, thickness, and growth-method of the virgin GGG were the same as for the magnetic film subtrates.

Double-crystal rocking curves were obtained using the appartus shown in Fig. 2. X-rays from a Cu target operated at 40 keV, 20 mA are collimated by a $\sim 0.5\times1$-mm^2 slit and undergo Bragg diffraction by the stationary first crystal. The diffracted beam is partially polarized, has a lateral divergence of not more than ~25 arc sec, and consists of the K_α line. The beam is then diffracted by the sample which is continuously rotated at 0.2 arc sec/sec in the neighborhood of the Bragg condition. In addition to the $\Delta\theta$ variation, the sample can be rotated in azimuth prior to measurement. In symmetric reflections this rotation provides information about sample curvature and lateral uniformity. The radiation is measured by a stationary "wide-open" Na I (Tl) detector with pulse-height analysis electronics. Typical counting rate for the beam incident on the sample was $\sim 10^5$ cps. The measured reflections were (444), (888), and (880), the latter with both asymmetries. The sample and the first crystal (a piece of ⟨111⟩ GGG) were set for the same reflection and asymmetry.

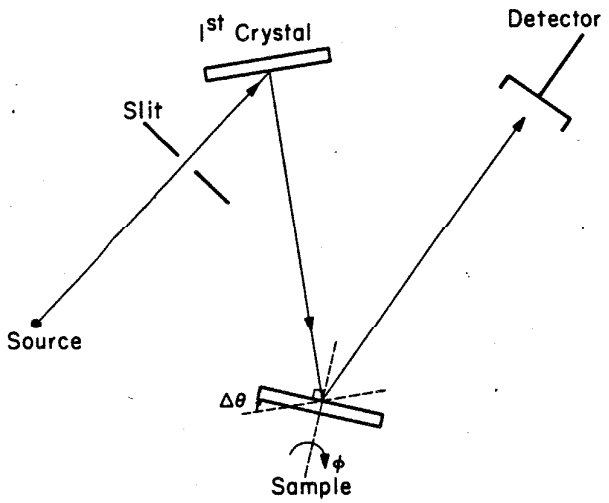

FIG. 2. Double-crystal x-ray diffraction apparatus.

V. RESULTS

A. He^+-implanted Gd, Tm, Ga:YIG

Figure 3(a) shows the experimental (dashed) and calculated (solid) rocking curves of sample FI, implanted with 140 keV, 3×10^{15} He^+/cm^2. Curves labeled 0 correspond to as-implanted material, while curves 1 and 2 are of samples which were ion milled to mechanically determined[14] depths of ~2500 and ~6800 Å, respectively. It should be noted that the curves belong to different samples cut from the same wafer. The reported uniformity of implanation across the wafer was about ± 5%. Differences in experimental rocking curves of as-implanted samples also indicate lateral variations of up to ± 5%. Unless data are taken of the same sample before and after milling, lateral variations will limit the agreement of experimental and calculated curves corresponding to different depths. Consequently the primary objective was to obtain strain and damage distributions which produce the best fit to the unmilled rocking curve. The distributions were built from the bottom up, using curves 2 and 1, together with the quoted milled depth, only as guides. Even so, the final distributions, shown in Fig. 3(b), yield rocking curves which match all three experimental curves quite well. The discrepancy in curves 1 can be removed by lowering the strain by about 5%.

Since strain is defined relative to the GGG substrate, the strain distribution [solid line in Fig. 3(b)] includes a region, 2800 Å thick, of constant strain. Its source is the lattice parameter difference between the LPE film and substrate. At greater distances from the interface, the total strain is the sum of the constant value and the implantation-induced strain. At any depth, the uncertainty in strain is not more than ± 2% of the maximum strain. The distribution [dashed in Fig. 3(b)] for the damage parameter U is linear with implantation-induced strain. That is, $U_j = 0.18\,\epsilon_j^{\perp}$, with $\epsilon_j^{\perp}$ in percent and U_j in Å. Because of the relatively large uncertainity (± 15%) in U at this damage level, some deviation from linearity cannot be ruled out. However, the average U is determined by closely matching the integrated experimental reflecting power $\int R_T d(\Delta\theta)$. In addition, the details of the rocking curves are best simulated by similar $\epsilon^{\perp}$

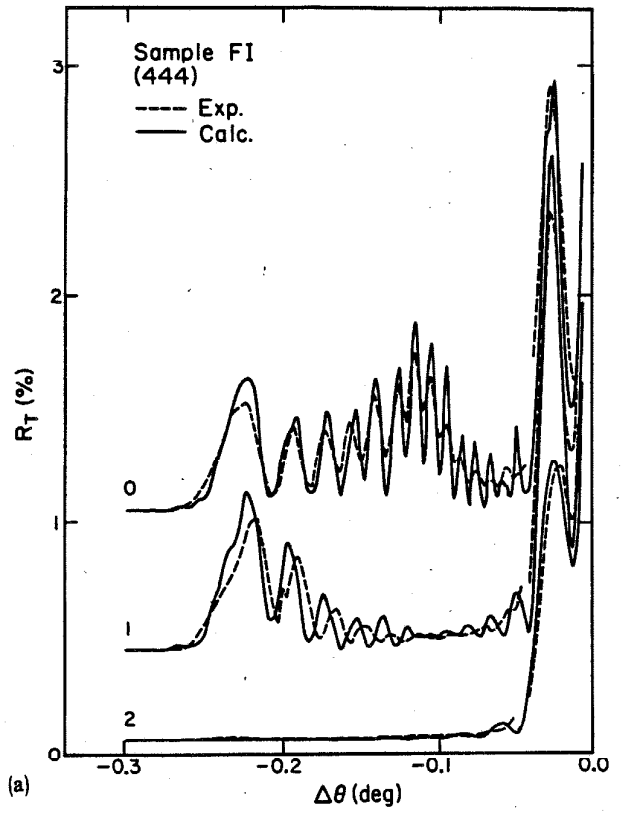

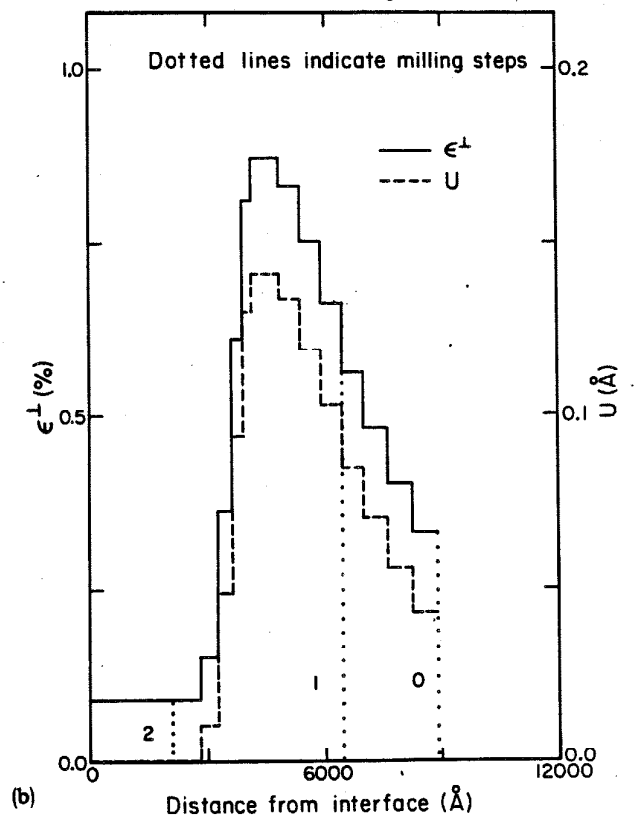

FIG. 3(a) Experimental (dashed) and calculated (solid) (444) rocking curves of sample FI (140 keV, 3×10^{15} He^{+}/cm^{2}). Curve 0 is from unmilled material; curves 1 and 2 correspond to progressively deeper milling. The curves are vertically displaced for clarity. (b) Strain (solid) and damage parameter U (dashed) distributions in sample FI. The vertical dotted lines indicate milling steps and are labeled to show correspondence with the data of (a).

and U distributions. In particular, the maximum $\epsilon^{\perp}$ and the maximum U occur at the same depth.

Rocking curves of sample FI (unmilled), obtained with (888) and (880) reflections, are shown in Fig. 4 and 5(a). Both curves are qualitatively similar to the (444) curve, but there are important differences. In (888) the $\Delta\theta$ range is about three times greater, the maximum reflecting power is an order of magnitude less, and the number of oscillations is almost twice as large as in (444). In (880), with $\gamma_0 > |\gamma_H|$, the $\Delta\theta$ range is reduced eight-fold with respect to (888), while the reflecting power is almost the same as for (444). Yet as shown by the agreement with calculation, both curves correspond to the strain and damage distributions of Fig. 3(b).

The more rapid oscillations of the calculated (888) and (880) curves have larger amplitude than in the experimental curves. The discrepancy is due to the assumption of planar uniformity in the sample and the neglect of incident beam divergence. In (444) the incident beam divergence is much less than the period of oscillation, but in (880), with $\gamma_0 > |\gamma_H|$, they are comparable. The convolution of the plane-wave solution with the incident beam, approximated here as a Gaussian with 6-arc sec standard deviation, produces the calculated curve in Fig. 5(b). The agreement with data is very good. For the (880) reflection with opposite asymmetry, $\gamma_0 < |\gamma_H|$, the incident beam divergence is again negligible compared to the period of oscillation. Although not shown in these figures, the plane-wave calculation, based on the strain and damage of Fig. 3(b), agrees equally well with the data.

The (444) rocking curves of samples FII (double im-

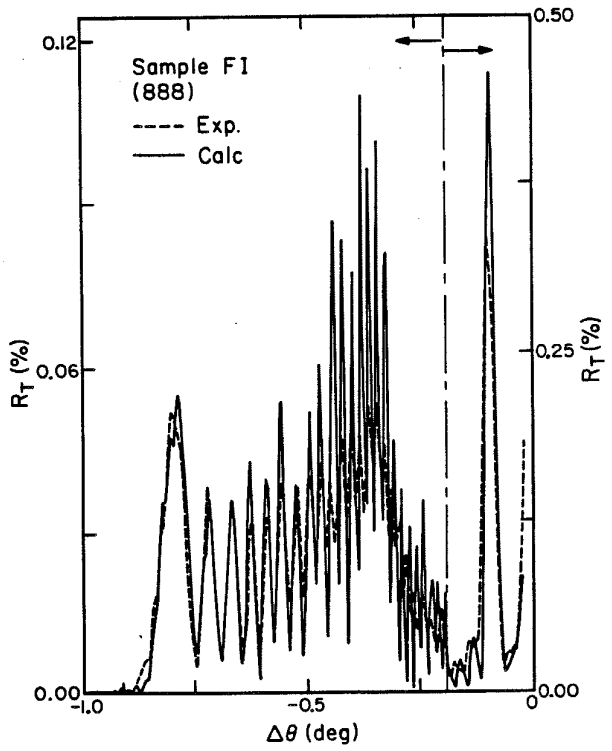

FIG. 4. Experimental (dashed) and calculated (solid) (888) rocking curve of sample FI.

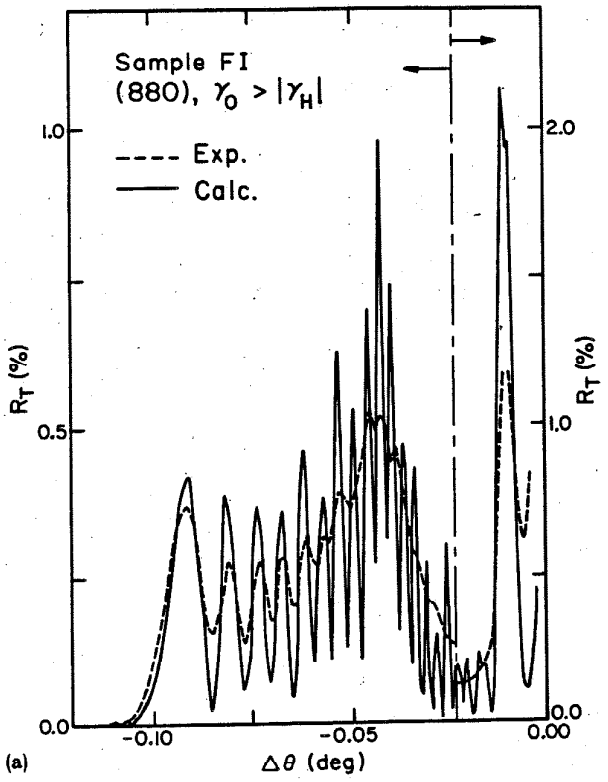

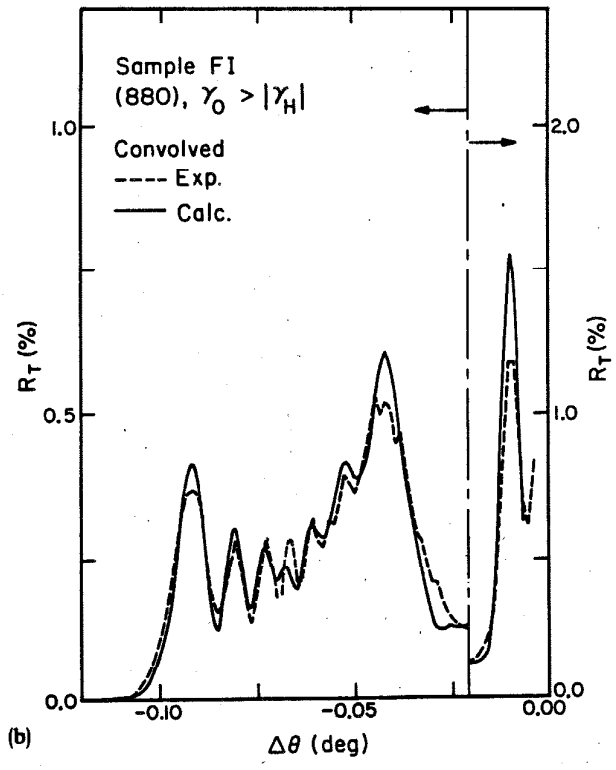

FIG. 5(a) Experimental (dashed) and calculated (solid) (880), $\gamma_0 > |\gamma_H|$, rocking curve of sample FI. (b) Same as (a) after the plane-wave solution was convolved with a Gaussian of 6-arc sec standard deviation.

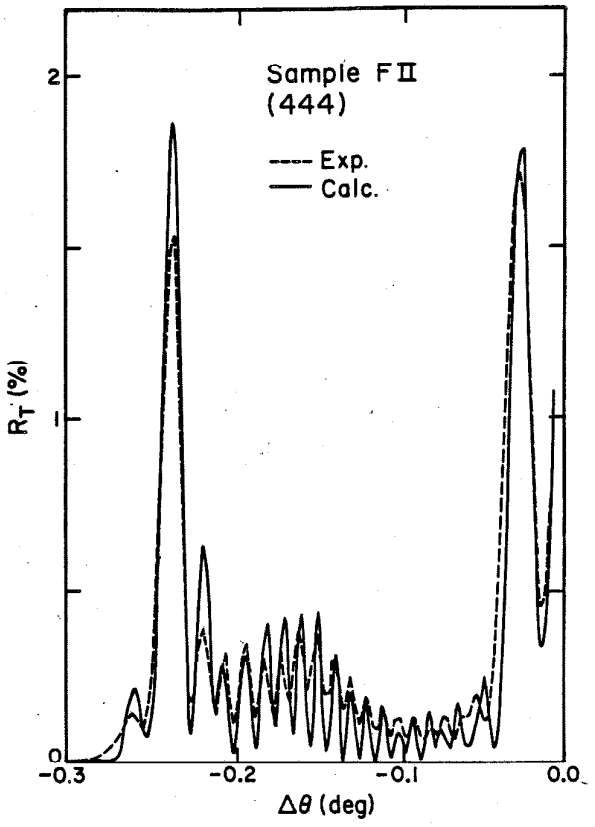

FIG. 6. Experimental (dashed) and calculated (solid) (444) rocking curves of sample FII, implanted with 140 keV, 3×10^{15} He^+/cm^2 + 70 keV, 1.4×10^{15} He^+/cm^2.

planation) and FIII (triple implanation) are shown in Fig. 6 and 7, respectively. The two curves exhibit a continuous change from the FI data [curve 0 in Fig. 3(a)]. The peak at $\Delta\theta \approx -0.24$ deg is becoming sharper and more intense, while the reflecting power in the range -0.22 deg $\lesssim \Delta\theta \lesssim -0.05$ deg is diminishing. The strain distributions corresponding to this behavior are shown in Fig. 8. For clarity, the damage distributions have been omitted. In each case, the relationship between damage and implanation-induced strain is the same as in Fig. 3(b). It is evident that a given depth strain and damage are unaffected by shallower implantation. The rocking curve of another unmilled FIII sample was significantly different from the data in Fig. 7. For that sample the strain distribution was much more uniform, with surface value of ~0.8%, instead of the 0.57% shown in Fig. 8.

B. Ne^+-implanted GGG

Experimental and calculated rocking curves of 100-keV Ne^+-implanted GGG are shown in Figs. 9(a)–(e). The doses were 0, 0.5, 1.0, 2.0, and 6.0×10^{14} atoms/cm^2, respectively. The angle axis is the same for all cases, but the reflecting power varies by an order of magnitude. The experimental rocking curve of the virgin sample [Fig. 9(a)] is well enough represented by the dynamical result for nonabsorbing crystals, but no special significance should be attached to this. If

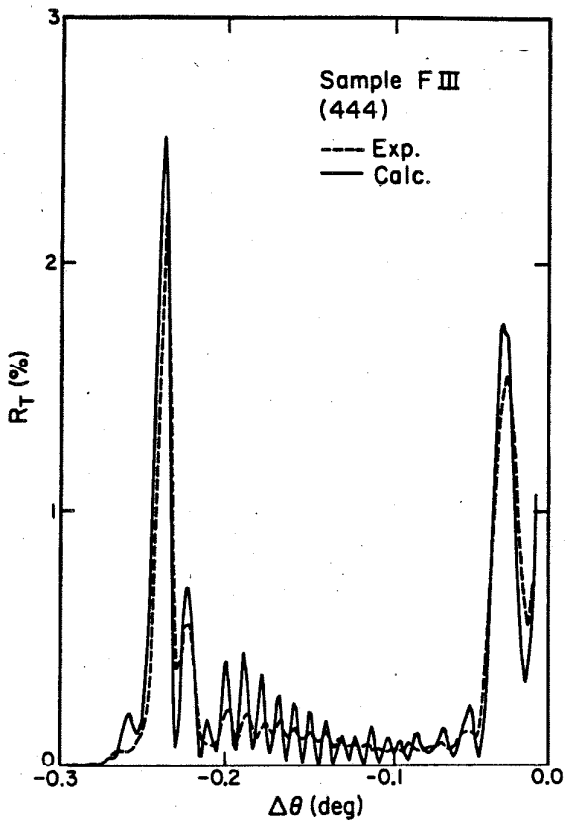

FIG. 7. Experimental (dashed) and calculated (solid) (444) rocking curves of sample FIII, implanted with 140 keV, 3×10^{15} He^+/cm^2 + 70 keV, 1.4×10^{15} He^+/cm^2 + 30 keV, 9×10^{14} He^+/cm^2.

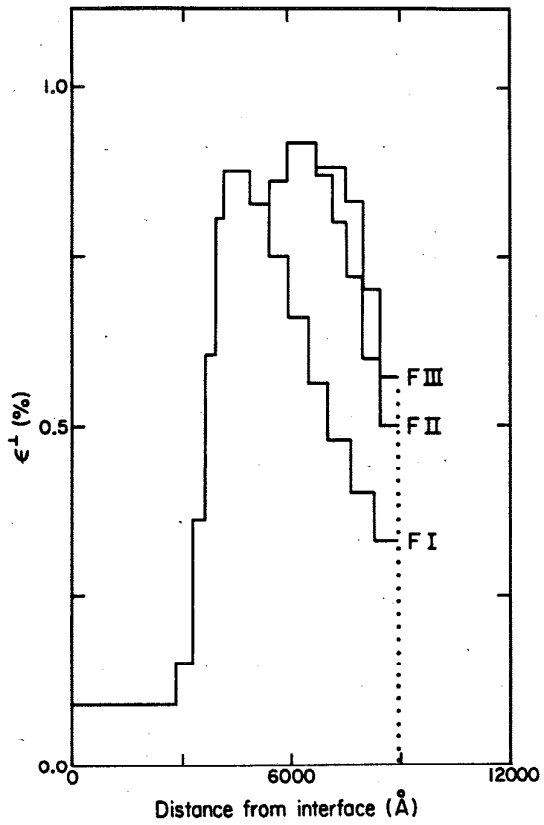

FIG. 8. Strain distributions of samples FI, FII, and FIII.

absorption is taken into account, the dynamical curve is considerably narrower for $\Delta\theta \gtrsim -0.01$ deg and $R_T \lesssim 2\%$. As described in Sec. II, the increased width of the experimental curve is attributed mainly to lattice parameter variations. The dynamical solution for nonabsorbing thick crystals is used throughout this paper to represent the substrate contribution.

The range of nonzero reflecting power in Figs. 9(b), 9(c), and 9(d) increases linearly with dose. At the same time the peak farthest from the origin decreases in relation to other peaks, as does the overall reflecting power. At 6×10^{14} Ne^+/cm^2, Fig. 9(e), the oscillations are much reduced and the reflecting power is close to that of virgin GGG. The calculated curves match the data quite well over the entire range of doses.

The strain and damage distributions corresponding to the calculated curve in Fig. 9(d) are shown in Fig. 10. The layer thickness, maximum strain, and maximum damage are 1900 Å, 2.49% and 0.40 Å, respectively. Damage is linear with strain, with $U_j(\text{Å}) = 0.16\,\epsilon_j^\perp(\%)$. As for the He^+-implanted films, some deviation from linearity is possible. The relatively heavy damage level presents the opportunity to demonstrate the importance of including damage in the calculation. Figure 11 shows the same experimental data as Fig. 9(d). The theoretical curve in Fig. 11 was obtained using the strain of Fig. 10 but assuming no damage, i.e., $U_j \equiv 0$ at all depths. The positions of the calculated maxima and minima are unchanged from those in Fig. 9(d), but the integrated reflecting power is now several times greater. In addition, the relative height of the maxima no longer agrees with the data.

The strain and damage distributions obtained for the lower doses, 0.5 and $1.0\times10^{14}/cm^2$, when multipled by 3.4 and 2.0, respectively, are practically identical to those of Fig. 10. The invariance of the shape with dose strongly suggests that strain is linear with dose. This further implies that the ratio 3.4 instead of 4.0 between the 2.0 and $0.5\times10^{14}/cm^2$ distributions is either due to an error in the dose or to annealing effects. The former is considered more likely. The calculated curve in Fig. 9(e) was obtained assuming linearity of strain and damage with dose. The peak strain and damage are then 7.5% and 1.2 Å, respectively. The latter number is close to the interatomic spacing and represents amorphousness. Experimentally and theoretically, most of the implanted layer no longer diffracts. The undulating part of the calculated curve indicates the presence of a thin crystalline region near the interface. The undulation is much reduced in the experimental data, possibly because of sample curvature which increases with strain.

VI. DISCUSSION OF THE RESULTS

The kinematical theory is able to account for the rocking curves of ion-implanted garnets with a wide range of layer thickness, strain, and damage level. Symmetric reflections are sensitive only to strains perpendicular to the sur-

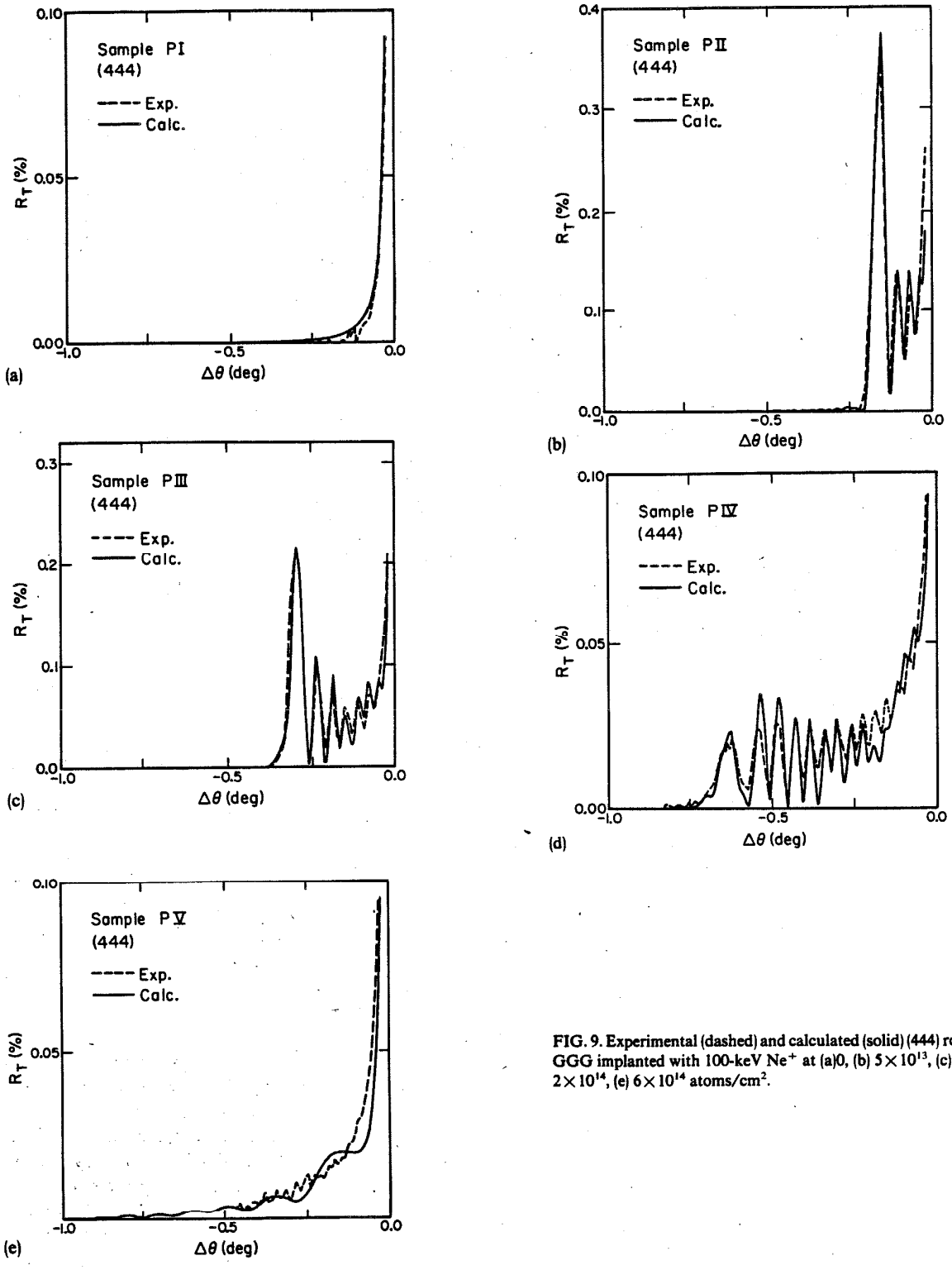

FIG. 9. Experimental (dashed) and calculated (solid) (444) rocking curves of GGG implanted with 100-keV Ne^+ at (a)0, (b) 5×10^{13}, (c) 1×10^{14}, (d) 2×10^{14}, (e) 6×10^{14} atoms/cm^2.

face, while asymmetric reflections measure both perpendicular and lateral strain. The agreement between calculated and experimental curves obtained with asymmetric reflections indicates that the lattice is indeed strained only in a direction perpendicular to the surface. Lateral strain is zero, as expected from the lattice match requirement.

The theoretical reduction in reflecting power due to random atomic displacement is very different for (444), (888), and (880). The good fit to these curves indicates that the assumed spherically symmetric Gaussian $\rho(\Delta \mathbf{r}_j)$ is consistent with the data. However, the validity of this assumption remains unproved. Since garnets are polyatomic, the

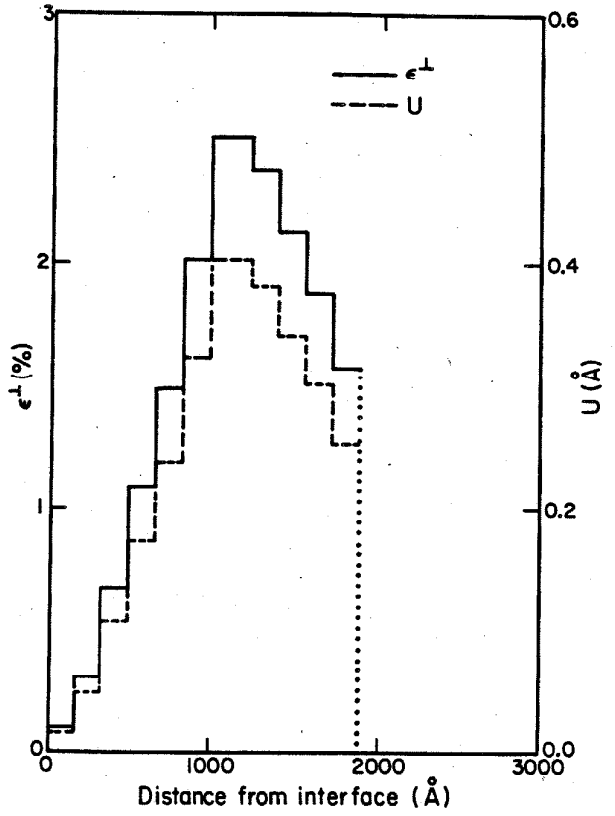

FIG. 10. Strain (solid) and U (dashed) distributions for sample PIV (2×10^{14} Ne^{+}/cm^{2}). The same distributions, when scaled by approximately the dose ratios, correspond to all other doses.

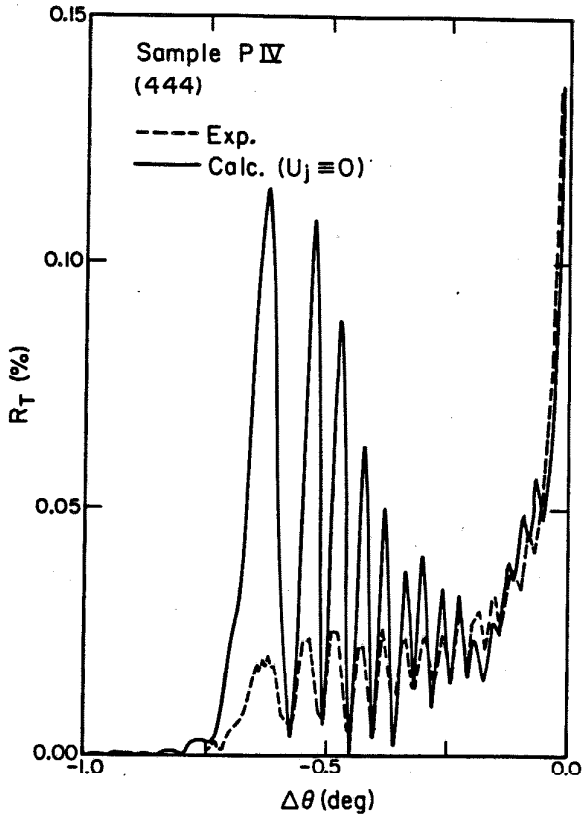

FIG. 11. Experimental (dashed) and calculated (solid) (444) rocking curves of sample PIV. The calculated curve was obtained from strain distribution of Fig. 10, but with zero damage.

contributions of various atoms to the structure factor depend on the particular reflection. It is conceivable that implantation results in a rearrangement of atoms such that the effect on the magnitude of the structure factor is the same as for random displacement. This ambiguity can be reduced by studying several other reflections. For (444), (888), and (880), the relative contribution of c sites, occupied by Gd, Tm, and Y, is ~80, 60, and 60%, respectively. The remaining contribution is almost entirely due to a combination of a sites (Fe) and d sites (Fe and Ga). The most abundant element, O, contributes very little in these reflections. Assuming random displacement, the obtained damage distributions apply mostly to the heavier elements in garnet. In a recent comparison[17] of the kinematical technique and backscattering spectrometry, the damage distributions obtained by the two methods were in satisfactory agreement.

The remarkably large strain and the linearity of the detailed distribution with dose are consistent with earlier results for the maximum strain.[18,19] Because of the lower theoretical sensitivity to damage, strict linearity between damage and strain has not been established. However, the results suggest that both the maximum and the average damage are linear with strain and dose. For both crystals, the proportionality constant between U and $\epsilon^{\perp}$ is 0.17 ± 0.01 Å. This relationship shows that strain and damage are initimately connected. *A priori* it might be expected that strain is due to the incorporation of implanted atoms into the unit cell. Such an affect was observed in doped Si, where the strain was negative and the damage negligible.[4-7] However, in garnets the range distribution of ions is significantly different from the strain distribution.[20] It was shown in Ref. 20 that the detailed strain distribution can be explained entirely in terms of nuclear energy loss. In that study the same strain was obtained with Ne^{+} and He^{+} doses which differed by almost two orders of magnitude. This was shown to be due to the difference in nuclear energy loss rates for Ne^{+} and He^{+}.

The presence of pronounced oscillations even in the moderately damaged sample PIV indicates that coherence and uniformity are maintained over macroscopic dimensions. In these garnets implantation appears to create only point defects. If extended defects, which cause strain and orientation variations, were present, the oscillatory structure would be smoothed out. Evidence of extended defects accompanied by severe broadening of the rocking curve was presented[12] for garnets subjected to relatively high ($\gtrsim 10^{16}/cm^{2}$) He^{+} doses. In those samples annealing resulted in large defect clusters probably caused by He bubble formation.

VII. SUMMARY

A kinematical model for general Bragg case x-ray diffraction in nonuniform crystals was presented. The kinematical approach has the advantage of computation speed over the more rigorous dynamical theory. The model is valid for

films of arbitrary thickness, provided the maximum reflecting power is less than ~6%. This requirement translates to maximum thickness of ~1 μm for typical crystals such as ion-implanted or doped Si, Ge, GaAs, and garnet. The model incorporates depth-dependent strain and random atomic displacements. Distributions in crystals are obtained by fitting the model to experimental rocking curves. The theoretical rocking curve is shown to be highly sensitive to strain distributions, layer thickness, lateral uniformity, and to a lesser extent, damage distributions. Accuracy of up to ~2% for these parameters is achievable.

The model was applied to He^+-implanted Gd, Tm, Ga:YIG and Ne^+-implanted $Gd_3Ga_5O_{12}$. In the former crystal the total strained layer thickness was 0.89 μm, with the strain varying between 0.09 and 0.91%. The maximum standard deviation U of random atomic displacements was 0.15 Å. Using symmetric and asymmetric reflections, the absence of lateral strain was demonstrated. In addition, the assumption of spherically symmetric random displacements was consistent with the data. The $Gd_3Ga_5O_{12}$ crystal was implanted with several doses corresponding to a wide range of damage. In all cases the layer thickness was 1900 Å; strain values of 2.49% corresponded to 0.40-Å U values. The detailed strain distribution was strictly proportional to ion dose. The damage distribution was closely linear with implantation-induced strain, although some deviation from strict linearity has not been ruled out. Both crystals showed the same relationship between damage and strain. The GGG crystal maintained single crystallinity up to the amorphous threshold.

ACKNOWLEDGMENTS

Thanks are due to C. H. Wilts for his continued support and for a careful reading of the manuscript. The contribution of H. L. Glass in the form of helpful discussions is gratefully acknowledged. B. M. Paine is thanked for the ion implantation of the GGG samples. Technical assistance by L. A. Moudy is acknowledged.

[1]S. Takagi, Acta Crystallogr. **15**, 1311 (1962).
[2]D. Taupin, Bull. Soc. Fr. Miner. Crist. **87**, 469 (1964).
[3]S. Takagi, J. Phys. Soc. Jpn. **26**, 1239 (1969).
[4]J. Burgeat and D. Taupin, Acta Crystallogr. A **24**, 99 (1968).
[5]J. Burgeat and R. Colella, J. Appl. Phys. **40**, 3505 (1969).
[6]A. Fukuhara and Y. Takano, Acta Crystallogr. A **33**, 137 (1977).
[7]B. C. Larson and J. F. Barhorst, J. Appl. Phys. **51**, 3181 (1980).
[8]R. W. James, *The Optical Principles of the Diffraction of X-rays* (Cornell University, Ithaca, New York, 1965).
[9]A. M. Afanasev, M.V. Kovalchuk, E. V. Kovev, and V. G. Kohn, Phys. Status Solidi A **42**, 415 (1977).
[10]See, for example, M. Buerger, *Vector Space and Its Application in Crystal-Structure Investigation* (Wiley, New York, 1953).
[11]V. S. Speriosu, H. L. Glass, and T. Kobayashi, Appl. Phys. Lett. **34**, 539 (1979).
[12]V. S. Speriosu, B. E. MacNeal, and H. L. Glass, Intermag. 1980 Conf., Boston, paper 22-4 (unpublished).
[13]W. H. Zachariasen, *Theory of X-ray diffraction in Crystals* (Wiley, New York, 1945).
[14]The Gd, Tm, Ga: YIG films and the ion milling were provided by the San Jose, California laboratory of IBM Corporation.
[15]K. Ju, R. O. Schwenker, and H. L. Hu, Intermag. 1979, New York (unpublished).
[16]Virgin GGG wafers were provided by the Anaheim, California laboratory of Rockwell International.
[17]B. M. Paine, V. S. Speriosu, L. S. Wieluński, H. L. Glass, and M-A. Nicolet, Fifth International Conf. Ion Beam Analysis, Sydney, Australia, 1981; Nucl. Instr. Meth. (in press).
[18]J. C. North and R. Wolfe, "Ion-Implantation Effects in Bubble Garnets" *In Ion-Implantation in Semi-conductors and Other Materials*, edited by B. L. Crowder (Plenum, New York, 1973).
[19]K. Komenou, I. Hirai, K. Asama, and M. Sakai, J. Appl. Phys. **49**, 5816 (1978).
[20]B. E. MacNeal and V. S. Speriosu, J. Appl. Phys. **52**, 3935 (1981).

Application to a Four Layer Gallium Aluminum Arsenide Laser Structure

The kinematical interpretation is valid for nonuniform layers with thicknesses much greater than that in the garnet films discussed earlier. An example is a GaAlAs laser structure considered in Ref. (21). In this study a four layer epitaxial film gave the rocking curve shown in Fig. 12(a), which at that time the authors considered too complicated for detailed interpretation. According to this reference, the curve was taken using a [100]-oriented GaAs substrate covered with four epitaxial layers:

1. 1.7 μm $Ga_{0.59}Al_{0.41}As$
2. 0.5 μm $Ga_{0.9}Al_{0.1}As$
3. 1.1 μm $Ga_{0.65}Al_{0.35}As$
4. 0.6 μm $Ga_{0.9}Al_{0.1}As$

Since the lattice parameter of AlAs is greater than that of GaAs, each of the four layers has a lattice parameter different from the substrate. According to Vegard's law, the difference is just proportional to the amount of Al substitution. Thus the strain profile is equivalent to the substitution profile. The rocking curve of Figure 12(b) was calculated using the distribution quoted in Ref. (21). This distribution is shown in Figure 12(c). The regions with higher strain correspond to higher Al substitution, the

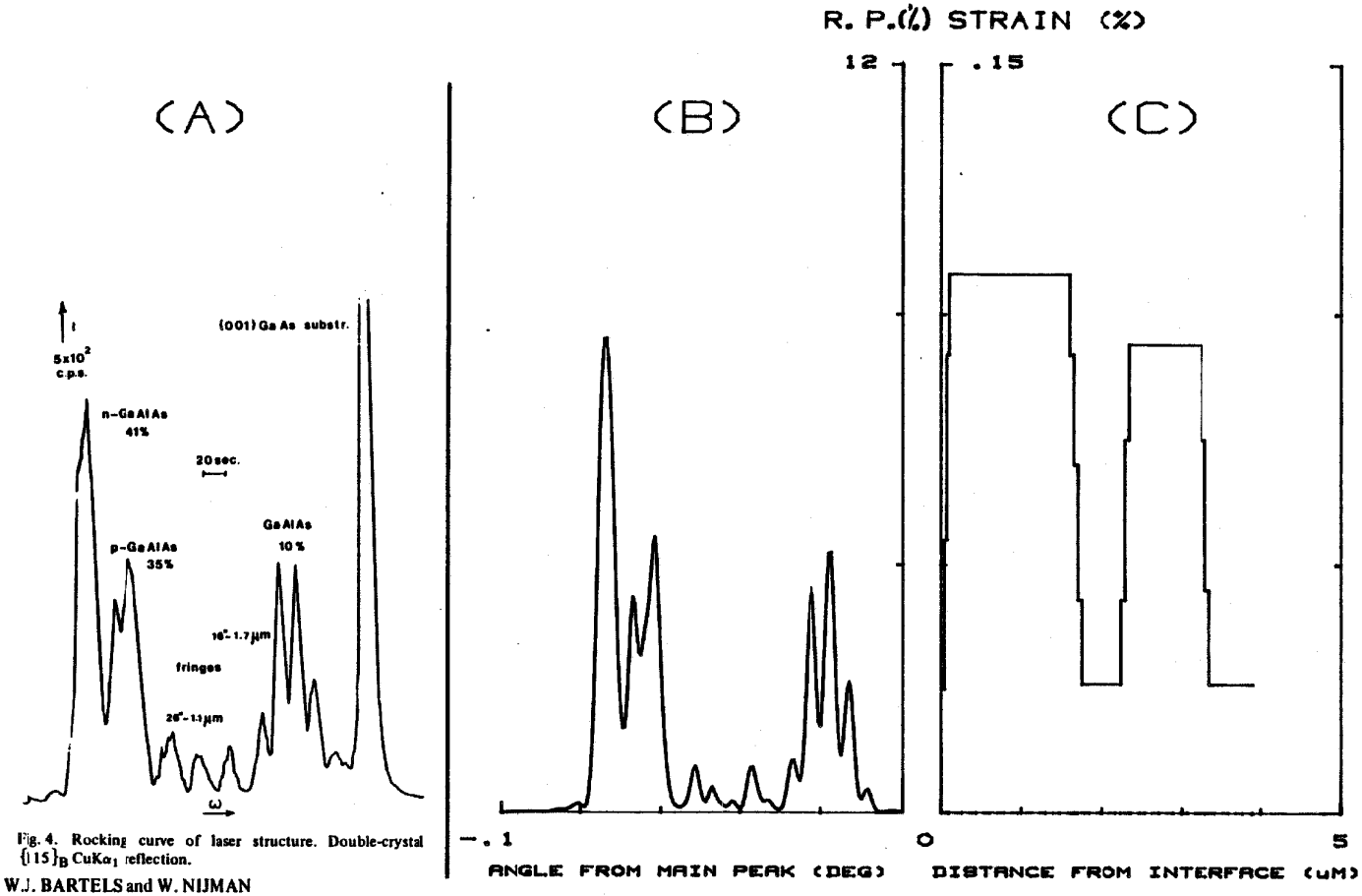

Fig. 4. Rocking curve of laser structure. Double-crystal $\{115\}_B$ $CuK\alpha_1$ reflection.

W.J. BARTELS and W. NIJMAN

Journal of Crystal Growth 44 (1978) 518–525

Figure 12. (a) Experimental and (b) calculated Cu K_α (115) rocking curve for a four layer GaAlAs laser structure. (c) Strain profile corresponding to the calculated curve.

degree of strain being adjusted to match the rocking curve. For a satisfactory fit it was necessary to include transition regions between the four layers, thus showing the high sensitivity to the strain profile stated earlier. Note that the maximum strain is an order of magnitude smaller than in the implanted samples considered earlier. In addition, the 4 μm thickness of the structure demonstrates the validity of the calculation for thick but nonuniform films.

Ref. 21. W.J. Bartels and W. Nijman, J.Cryst. Growth 44, 518(1978).

Chapter III

Comparison of kinematical x-ray diffraction and backscattering spectrometry

Strain and damage profiles obtained by the rocking curve method are compared to those obtained by Rutherford backscattering.

80

Nuclear Instruments and Methods 191 (1981) 80–86
North-Holland Publishing Company

COMPARISON OF KINEMATIC X-RAY DIFFRACTION AND BACKSCATTERING SPECTROMETRY – STRAIN AND DAMAGE PROFILES IN GARNET *

B.M. PAINE [1], V.S. SPERIOSU [1], L.S. WIELUŃSKI [1,**], H.L. GLASS [2] and M.A. NICOLET [1]

[1] *California Institute of Technology, Pasadena, CA 91125, U.S.A.*
[2] *Rockwell International, Microelectronics Research and Development Center, Anaheim, CA 92803, U.S.A.*

We compare the results of measurements of crystal distortions made by means of two techniques: a new kinematic X-ray diffraction technique and backscattering spectrometry of channeled MeV ions. Samples were ⟨111⟩ single-crystal gadolinium gallium garnet (GGG) that had been implanted at room temperature with 100 keV Ne^+ ions to various doses. For these implantation conditions, the ranges of sensitivity of the two techniques overlap for about one decade in implantation dose up to the amorphous threshold. X-ray diffraction was found to be most sensitive to low damage levels while backscattering was found to be most sensitive to high damage levels. Neither method as applied here is sensitive to light atoms in a heavy matrix. In the former technique, strain and damage profiles were obtained by fitting a model to the X-ray rocking curve. In the latter technique, the damage profile was obtained directly from the energy spectrum of backscattered particles while strain was obtained from the implantation-induced changes in the relative orientations of channeling axes. The two techniques are in excellent agreement on the near-surface strain, but differ significantly at depths below ~500 A. The damage distributions agree to within a factor of 2.

1. Introduction

Backscattering spectrometry (BSS) of MeV ions has long been used to obtain damage profiles in ion-implanted single-crystals [1]. By contrast, X-ray diffraction has generally been used only to determine average lattice parameters in crystalline materials [2] or lattice parameter differences between distinct layers in composite single-crystal samples (e.g. epitaxial films) [3]. For single crystals with lattice parameters which vary with depth, *dynamical* X-ray diffraction theory [4] has been used successfully [5–7] to obtain profiles of the variations in the lattice parameter, but at the cost of considerable computing time. *Kinematical* X-ray diffraction (KXD) theory [4], which is mathematically much simpler, has recently been adapted [8,9] for characterizing thin ($\leqslant 1$ μm) single-crystal films. The technique is believed to be highly sensitive to variations of lattice parameters with depth, lateral non-uniformities, and, to a lesser extent, damage distributions. Where results are available, it is in close agreement with the dynamical theory. Both KXD and BSS can sense changes in atomic positions that are well below the 1 Å range. To help evaluate the techniques of KXD and BSS and to gain insight into their capabilities and limitations, we have conducted a comparison of the results of the two methods applied to implanted samples of single-crystal garnet. We have compared their sensitivities for a range of implantation doses and compared strain and damage profiles obtained with a single dose.

2. Experimental procedure

Measurement were conducted on ⟨111⟩ single-crystal gadolinium gallium garnet (GGG). This material, which is cubic and has the stoichiometry $Gd_3Ga_5O_{12}$ was chosen because implantation with moderate doses causes crystal distortions that are within the ranges of sensitivity of both KXD and BSS. Implantations were performed at room temperature with 100 keV Ne^+ ions to doses ranging from 5×10^{13} to 6×10^{14} ions cm^{-2}. These doses gave damage concentrations ranging from low levels up to full amorphicity as determined by both techniques. Two sets of samples were prepared under closely similar conditions and analyzed by the respective techniques.

The X-ray diffraction system is shown schemati-

* This work was partially supported by the Defense Advance Research Projects Agency and monitored by the Air Force Office of Scientific Research under contract number F49620-C-80-0101 and the U.S. Army Research Office under the Joint Services Electronic Program [DAAG-29-80-C-0103].

** Permanent address: Institute of Nuclear Research, Warszawa, Hoza 69, Poland.

0029-554X/81/0000–0000/$02.75

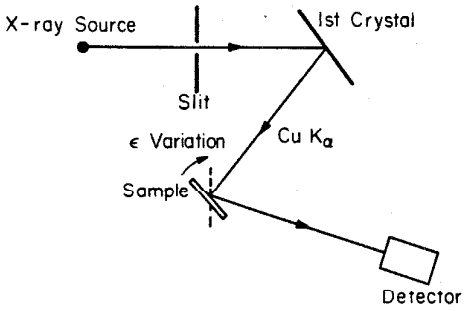

Fig. 1. Schematic diagram of the X-ray diffraction system.

cally in fig. 1. X-rays from a Cu target pass through a slit and impinge on the first crystal. The latter is adjusted for the same Bragg angle as that required for the sample and serves to reduce the beam divergence and select the characteristic K_α line. It also has the effect of partially polarizing the beam. Radiation diffracted from the sample is sensed by a NaI(Tl) detector. In these measurements, the sample and detector were rotated about an axis at the sample surface to the desired Bragg condition. The sample was then rotated finely about the same axis and the reflecting power recorded as a function of angle, to give the so-called "rocking curve". The illuminated area on the sample was ~2 mm^2. A piece of ⟨111⟩ GGG was used for the first crystal.

The experimental arrangement for the backscattering measurements is shown in fig. 2. To prevent electrical charging during BSS analysis, a 100 Å layer of Al was deposited on the sample surfaces and contact made by means of a steel clip. The samples were aligned for channeling by varying θ and ϕ.

X-ray diffraction is only sensitive to displacements of atoms in a direction perpendicular to the diffracting plane while backscattering of channeled ions is sensitive only to displacements in a direction perpendicular to the channel axis. Therefore the optimum arrangement for comparing the two techniques would involve channeling along axes that are parallel to the planes employed for X-ray diffraction. However, because of poor definition of the channels for high index axes a compromise was made such that only a component of the channeling directions lay in the diffraction planes. Symmetric Bragg X-ray reflections from (444) planes were employed and the backscattering measurements were made with the beam channeled in the ⟨110⟩ and ⟨100⟩ directions.

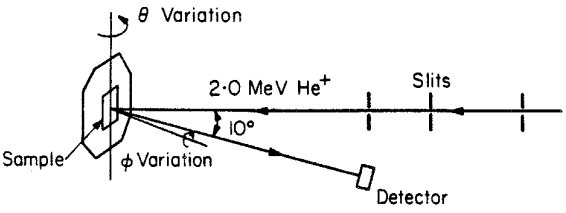

Fig. 2. Schematic diagram of the backscattering system.

3. Analysis and results

3.1. Sensitivity–dose dependence

The raw data obtained from KXD and BSS analyses are shown for a range of implantation doses in fig. 3. It is clear that the two systems are roughly complementary in terms of their régimes of maximum sensitivity: KXD is most sensitive for doses $\leqslant 10^{14}$ Ne^+ ions cm^{-2} while BSS is most sensitive above that value. At a dose of 5×10^{13} Ne^+ ions cm^{-2}, for example, the KXD curve shows very prominent structure (part a) while the BSS spectrum is little changed from that for an unimplanted sample (part e). This is because X-ray rocking curves are highly sensitive to strain, even at low magnitudes, while channeling BSS spectra mostly reveal only crystal damage. On the other hand, for an implantation dose of 6×10^{14} Ne^+ ions cm^{-2} the KXD signal is very small (part d) while the BSS channeling spectrum has a lot of structure (part h). This is because at high damage concentrations the probability of backscattering a channeled ion is high while the intensity of coherently diffracted X-rays is low.

Observation of the high energy part of a BSS channeling spectrum reaching the same heights as the random spectrum is typically taken to indicate that the corresponding layer of the sample is "amorphous". Similarly, in X-ray studies a thin layer is said to be "amorphous" when it gives rise to a rocking curve with no oscillations and a reflecting power close to that from unimplanted material. It has not previously been clear whether these two definitions coincide. From the results in parts d and h of fig. 3, it appears that when a sample is amorphous by one of these definitions, it does indeed satisfy the criteria for amorphicity that are usually adopted with the other technique.

While the respective sensitivities of the two tech-

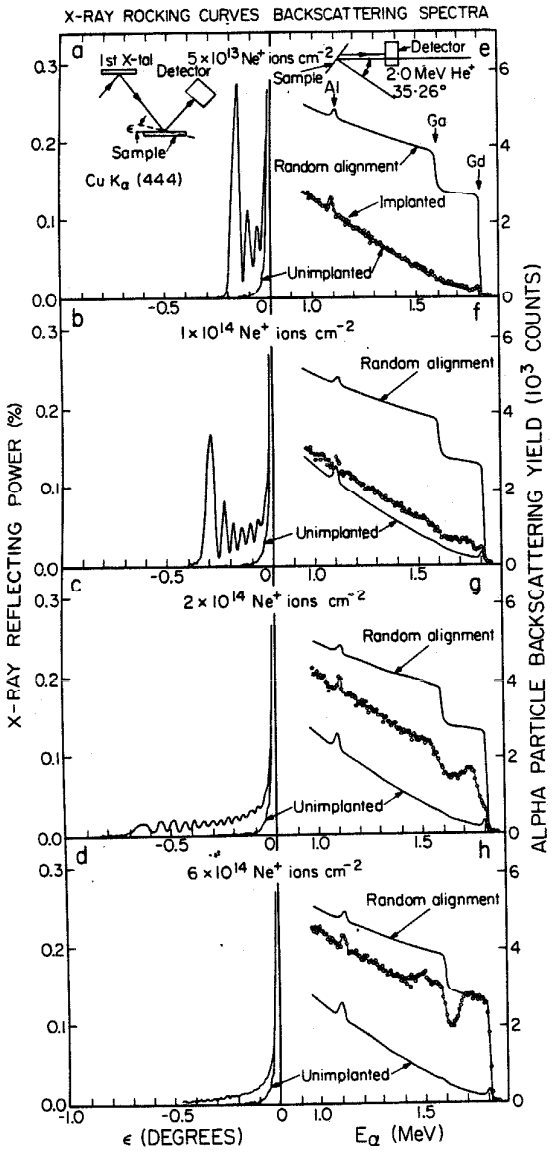

Fig. 3. X-ray rocking curves and He^+ backscattering spectra from GGG samples implanted with a range of doses of 100 keV Ne^+ ions. The angle ϵ is referred to the orientation of the Bragg peak from undamaged crystal (at 25.5°). The backscattering spectra were obtained with the incident beam channeled in the ⟨110⟩ direction.

niques vary with damage levels, neither technique as applied in fig. 3 was sensitive to light atoms (e.g. O) in the heavy Gd–Ga matrix. However, it should be noted that if the light atoms had been of particular interest, both techniques could readily have been modified to enhance their sensitivities to such atoms: X-ray reflections can be found for which most of the diffracted intensity is due to the light ions, and elastic (α, α) resonances with cross-sections far exceeding the Rutherford level can be employed for detecting ^{16}O [10].

3.2. Strain profile

Strain and damage in a crystal lattice are represented schematically in fig. 4. Strain is the fractional change $\Delta a/a$ in lattice parameter resulting from a uniform displacement of atoms. According to KXD measurements [11] ion implantation typically only causes strain that is perpendicular to the sample surface. In addition to strain, ion implantation also induces damage, i.e. random displacements δr of atoms from their lattice positions.

In the KXD model, the implanted crystal acts as a set of independently, but coherently diffracting laminae, each incorporating many unit cells and oriented parallel to the surface. The strain distribution is incorporated by allowing each lamina to have its own constant strain value. The distribution of incoherently displaced atoms (damage) is described by a probability function $\rho(\delta r)$ which changes the mean structure factor in each lamina. In this paper, for simplicity, $\rho(\delta r)$ was assumed to be a spherically symmetric Gaussian function.

Experimental rocking curves can be analyzed directly in terms of this model to yield parameters such as strained layer thickness, mean and maximum strain, and thickness-averaged r.m.s. values of (δr). In addition, detailed strain and r.m.s. (δr) distributions

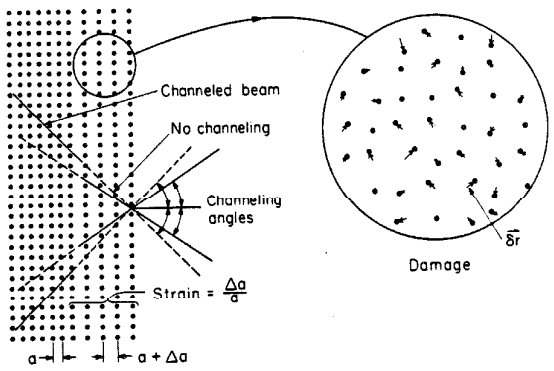

Fig. 4. Schematic representations of strain and damage in a crystal lattice.

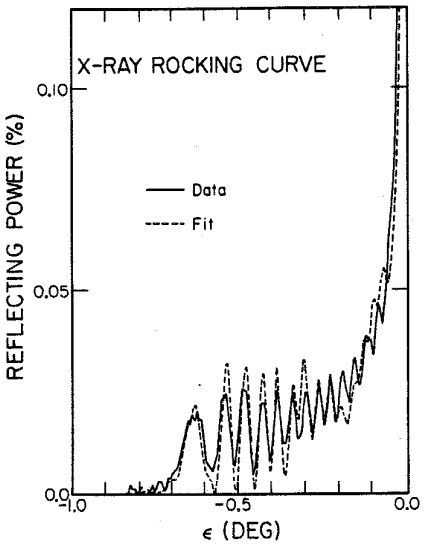

Fig. 5. Continuous curve: KXD rocking curve for the GGG sample after implantation with 100 keV Ne^+ ions to dose of 2×10^{14} ions cm^{-2}. Dashed curve: fit to the data obtained by means of the method of Speriosu et al. [8,9].

can be obtained by fitting the entire experimental rocking curve with a curve generated by the model described above (see refs. 8 and 9 for details). The fitting procedure was applied to the curves shown in fig. 3a–d, and very good fits were obtained in all cases. An example of data and fit is shown in fig. 5. The presence of pronounced oscillations in the data indicates very good lateral uniformity of the sample. The strain profile corresponding to this fit is plotted as a heavy line in fig. 7.

The approach adopted for BSS measurement of strain is illustrated schematically in fig. 4. If a region of the lattice is strained in a direction perpendicular to the surface, then the orientations relative to the surface of axes other than the ⟨111⟩ axis will be changed relative to those in an unimplanted sample. While absolute measurements of their orientations would be difficult, measurements of angular separations between axes are straightforward. Thus, energy windows were set in the backscattering spectra on the Gd signal at positions corresponding to a depth of 700 Å, and a measurement was made of the angular separation of the ⟨100⟩ and ⟨110⟩ axes on opposite sides of the ⟨111⟩ axis for both unimplanted GGG and the sample that had been implanted with 2×10^{14} Ne^+ ions cm^{-2}. At each axis the goniometer angle ϕ was adjusted so that the incident beam was channeled in the (110) plane and then θ was varied in steps of 0.1° across the axial channeling dip. The results are shown in fig. 6. Since the ⟨111⟩ axes in the mounted samples lay within 0.2° of the normal to the goniometer, it was not necessary to change ϕ in order to stay in the (110) plane during a scan over an axis. Also, for this reason the ϕ coordinates of the ⟨100⟩ and ⟨110⟩ axes differed by only 0.4°. Nevertheless, both the θ and ϕ coordinates of these axes were taken into account in calculating their angular separation. The precise θ coordinates of the axes were obtained by fitting inverted Gaussian curves to the data of fig. 6 by the method of least squares. The difference

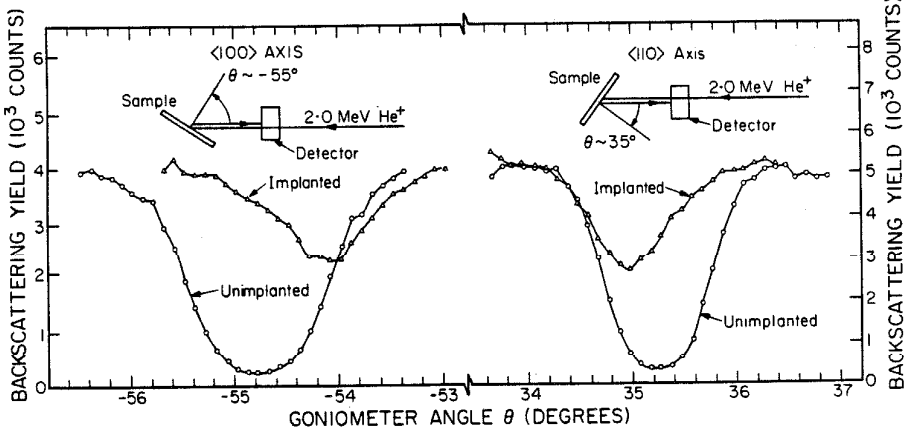

Fig. 6. Angular scans in θ of the yield of backscattered alpha particles from a window on the Gd signal at an energy corresponding to a depth of 700 Å.

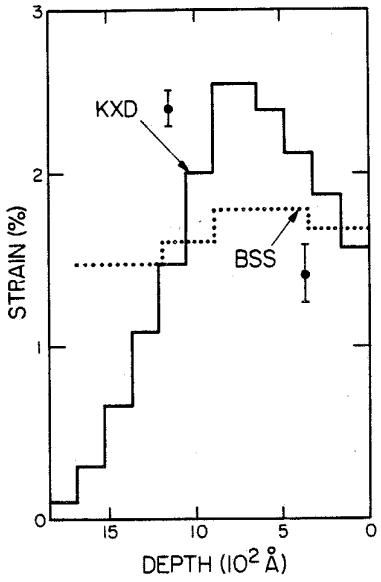

Fig. 7. Profiles of strain in the sample implanted with 2×10^{14} Ne^+ ions cm^{-2} at an energy of 100 keV.

in the angular separations in the implanted and unimplanted samples was $-0.9° \pm 0.1°$, implying a strain of $1.7 \pm 0.2\%$.

In addition to the window at 700 Å, three other windows were applied to the spectra at energies corresponding to various depths and the channeling angles in these were measured relative to those in the 700 Å window. The resulting profile of strain to a depth of ~1700 Å is shown as the dotted curve in fig. 7.

It is evident from fig. 7 that the two techniques are in good agreement for the strain near the surface, but while the KXD curve rises to a peak strain of 2.5% at ~700 Å and falls off to essentially zero at 1800 Å, the BSS curve remains roughly horizontal. We suggest that this discrepancy is the result of steering of the channeled alpha particles in the strained lattice. If the variations of crystal strain with depth are not abrupt, then it is possible that ions that are channeled in the surface layers of the sample are steered into the channels with different orientations that exist deeper in the sample. If this occurs, then angular scans obtained with energy windows corresponding to any depth will all measure mostly the strain at the surface. It would be of interest to test this hypothesis by recording BSS spectra from samples that have been etched to successively greater depths.

3.3. Damage profiles

Damage profiles were also deduced by means of both techniques for the sample that had been implanted with 2×10^{14} Ne^+ ions cm^{-2}. The BSS profile was derived from a spectrum obtained with the incident beam channeled in a ⟨110⟩ direction, part of which is shown in fig. 8. A dechanneling curve beneath the direct scattering peak was calculated iteratively [12] assuming (1) a critical angle at all depths equal to that measured at the surface ($2\psi_{1/2} = 1.1°$); (2) a uniform flux of channeled particles within the channels; (3) that *all* displaced atoms interact with the channeled particles; and (4) that dechanneled particles are not scattered back into channels. The result is the heavy stepped curve in fig. 8. This curve appears to be an underestimate since it should reach the data level at a point beyond the implanted region. This difference is possibly the result of a decrease in the critical channeling angle with higher damage densities below the sample surface, and extra dechanneling caused by depth-dependent lattice strain. Therefore, for the purpose of ob-

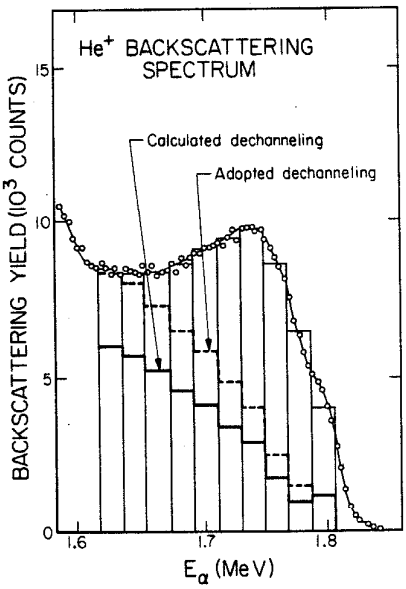

Fig. 8. Portion of the backscattering spectrum from a GGG sample implanted with 2×10^{14} Ne^+ ions cm^{-2} at an energy of 100 keV. The sample was oriented so the incident beam was channeled in the ⟨110⟩ direction. Solid curve: dechanneling calculated from a simple model (see text). Dashed curve: finally adopted dechanneling curve.

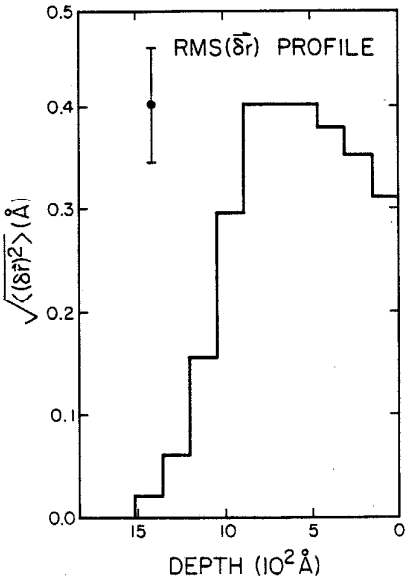

Fig. 9. R.m.s. value of δr obtained from the fit to the KXD data shown in fig. 5.

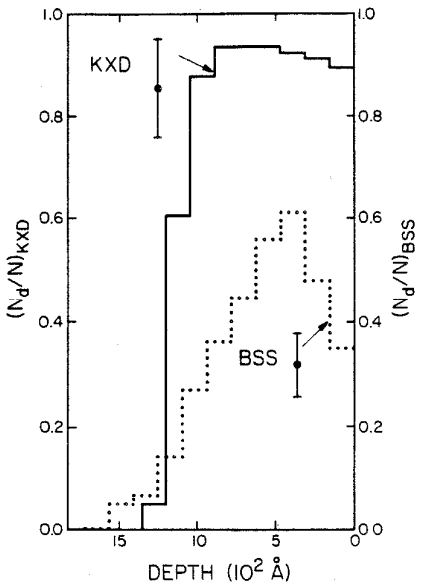

Fig. 10. Profiles of damage in the sample implanted with 2×10^{14} Ne^+ ions cm^{-2} at an energy of 100 keV. The BSS curve was obtained directly from fig. 8 while the KXD curve is the fractional number of atoms displaced by more than a_{TF} = 0.15 Å in a direction parallel to the lattice plane, deduced from the r.m.s. (δr) profile of fig. 9, assuming spherical symmetry.

taining a realistic damage profile this calculated curve was simply scaled up to the level indicated by the dashed curve in fig. 8. The resulting profile of N_d/N, the relative number of displaced atoms, is shown in fig. 10 as a dotted curve.

The KXD fitting technique described earlier yields the profile of r.m.s. (δr) in addition to the strain profile. For this calculation, the relative sensitivities of the Cu K_α (444) reflections to Gd, Ga and O were taken to be the same as those for undamaged GGG, i.e. ~80%, ~20% and 0%, respectively. This assumption is valid if $\langle \delta r \rangle = 0$, i.e. the mean random displacement is zero. The resulting r.m.s. (δr) profile is shown in fig. 9. For comparison with the BSS results, this curve was converted to the profile of fractional number of atoms with planar projections of δr that are greater than the Thomas–Fermi radius, a_{TF}, in unimplanted material (estimated to be 0.15 Å). The result is plotted as a continuous curve in fig. 10. The damage depths are in good agreement, but the KXD curve is about a factor 2 higher than the BSS result. However, in the light of the very different approaches employed by the two techniques, we regard this as satisfactory agreement.

Several factors may be responsible for the differences in the magnitudes of the two curves in fig. 10. The use of the Thomas–Fermi radius for calculating N_d/N from the KXD results is somewhat arbitrary. Since damage is heavy for a dose of 2×10^{14} Ne^+ ions cm^{-2}, the *effective* radius is probably larger than its value for a perfect crystal, and in fact we find good agreement with the BSS curve if a value of a_{TF} = 0.35 Å is assumed. Also, if peaking of the flux density of channeled ions near the centers of the channel were taken into account, the number of displaced atoms deduced from the BSS results would increase – again bringing the results of the two techniques into closer agreement. Finally, the assumptions of a spherically symmetric Gaussian form for $\rho(r)$ and that $\langle \delta r \rangle = 0$, while being reasonable, may not be entirely correct.

4. Summary

We have conducted a comparison of the results of kinematic X-ray diffraction and backscattering spectrometry analyses of strain and disorder in 100 keV Ne^+-implanted gadolinium gallium garnet. Our results can be summarized as follows:

1) For our implantation conditions, the two techniques have a common range of sensitivity for doses varying over about one decade up to the threshold for amorphicity.

2) KXD is most sensitive to low lattice distortion (dose $\leqslant 1 \times 10^{14}$ Ne^+ ions cm^{-2}) while BSS is most sensitive to high lattice distortion (dose $\geqslant 1 \times 10^{14}$ Ne^+ ions cm^{-2}). Neither technique, as usually applied, can readily sense light atoms in a heavy matrix.

3) Both techniques yield the same value for the thickness of a damaged layer.

4) Strain profiles from the two techniques are in good agreement at the sample surface. However, the KXD curve has a peak at ~700 Å and drops off to zero at greater depths while the BSS results are roughly constant with depth.

5) The KXD and BSS magnitudes of the profiles of the relative number of displaced atoms agree to within a factor 2.

We acknowledge technical assistance from L.A. Moudy at Rockwell International.

References

[1] See, for example, Backscattering spectrometry, eds., W.K. Chu, J.W. Mayer and M-A. Nicolet (Academic Press, New York, 1978).
[2] See, for example, B.D. Cullity, Elements of X-ray diffraction (Addison-Wesley, Reading, Massachusetts, 1956).
[3] See, for example, M.A.G. Halliwell, R. Heckingbottom and P.L.F. Hemment, J. Phys. D 10 (1977) L29.
[4] See, for example, W.H. Zachariasen, Theory of X-ray diffraction in crystals (Wiley, New York, 1945).
[5] J. Burgeat and D. Taupin, Acta Crystallogr. A24 (1968) 99.
[6] A. Fukuhara and Y. Takano, J. Appl. Cryst. 10 (1977) 387.
[7] B.C. Larson and J.F. Barhorst, J. Appl. Phys. 51 (1980) 3181.
[8] V.S. Speriosu, H.L. Glass and T. Kobayashi, Appl. Phys. Lett. 34 (1979) 539.
[9] V.S. Speriosu, to be published.
[10] L.C. Feldman and S.T. Picraux, in Ion beam handbook for materials analysis, eds., J.W. Mayer and E. Rimini (Academic Press, New York, 1977) ch. 4.
[11] V.S. Speriosu, B.E. MacNeal and H.L. Glass, Intermag 1980 Conf., Boston, paper 22-4 unpublished.
[12] F.H. Eisen, in Channeling, ed. D.V. Morgan (Wiley, New York, 1973) ch. 14.

Chapter IV

X-ray rocking curve and ferromagnetic resonance investigations of ion-implanted magnetic garnet

Elucidation of the behavior of crystalline and magnetic properties versus species, dose and annealing.

X-ray rocking curve and ferromagnetic resonance investigations of ion-implanted magnetic garnet

V.S. Speriosu and C.H. Wilts

California Institute of Technology
Pasadena, CA 91125

Abstract

Detailed analyses of X-ray rocking curves and ferromagnetic resonance spectra were used to characterize properties of <111>-oriented Gd,Tm,Ga:YIG films implanted with Ne^+, He^+, and H_2^+. For each implanted species the range of doses begins with easily-analyzed effects and ends with paramagnetism or amorphousness. Ion energies were chosen to produce implanted layer thicknesses of 3000Å to 6000Å. Profiles of normal strain, lateral strain, and damage were obtained. The normal strain increases with dose and near amorphousness is 2.5%, 3.4%, and 3.9% for Ne^+, He^+, and H_2^+, respectively. Lateral strain is zero for all values of normal strain, implying absence of plastic flow. Comparison of these results with the reported decrease in lateral stress implies either a large reduction in Young's modulus or a transition to rhombohedral equilibrium unit cell. Damage is modelled by a spherically-symmetric gaussian distribution of incoherent atomic displacements. Due to the use of (444), (888), and (880) reflections the sensitivity is greatest for the c-sites occupied by Gd, Tm, and Y. The standard deviation of displacements increases linearly with strain with proportionality constant 0.25, 0.18, and 0.13 Å/% for Ne^+, He^+, and H_2^+, respectively. For maximum strains up to 1.3% annealing in air reduces the strain without changing the shape of the profile. The behavior of the strain with annealing is nearly independent of implanted species or dose. After annealing at 600°C the strain is 40% of

the original value. Magnetic profiles obtained before and after annealing were compared with the strain profiles. The local change in anisotropy field ΔH_k with increasing strain shows an initially linear rise for both He^+ and Ne^+. The slope is -4.1 kOe/%, in agreement with the magnetostriction effect estimated from the composition. For strain values between 1% and 1.5%, ΔH_k saturates reaching peak values of -3.6 kOe for He^+ and -2.8 kOe for Ne^+. At strain values near 2.3% for He^+ and 1.8% for Ne^+, ΔH_k drops to nearly zero and the material is paramagnetic. For peak strains greater than 1.3% for He^+ and 1.1% for Ne^+ the relation between uniaxial anisotropy and strain is not unique. The saturation magnetization $4\pi M$, the ratio of exchange stiffness to magnetization (A/M) and the cubic anisotropy H_1 decrease with strain reaching zero at 2.3% and 1.8% for He^+ and Ne^+, respectively. At these strain values the damping coefficient α is 50% and 80% greater than bulk value for He^+ and Ne^+, respectively. For higher observed strains the material remains paramagnetic. Upon annealing of samples implanted with low doses of Ne^+ and He^+ the anisotropy field follows uniquely the behavior with strain for unannealed material. At 600°C the magnetization returns to bulk value but the ratio A/M remains 20% low. For H_2^+ implantation the total ΔH_k consists of a magnetostrictive contribution due to strain and of a comparable excess contribution associated with the local concentration of hydrogen. The profile of excess ΔH_k agrees with calculated LSS range. The presence of hydrogen results in a reduction of $4\pi M$ not attributable to strain or damage. For a peak strain of 0.60% and a peak total ΔH_k of -4.5 kOe, the magnetization is only 40% of bulk value. After annealing up to 350°C the excess ΔH_k diminishes and redistributes itself to the regions neighboring the peak damage. At 400°C the excess is nearly zero. For higher annealing temperatures the only component of ΔH_k is magnetostrictive. At 600°C, the magnetization, the ratio A/M, and α return to bulk values.

I. Introduction

Since the discovery[1] that ion-implantation in magnetic garnets is useful in the manufacture of devices, there has been an interest in the properties of implanted garnets. These properties may be subdivided into three broad categories: (1) the damage viewed primarily from a crystallographic point of view, (2) the possible effects due to the presence of the dopant, and (3) the magnetic properties arising from (1) and (2).

Damage has been studied by X-ray diffraction[1-13], indirectly through stress measurements[14-16], enhanced etch rate measurements[17-19], Rutherford back-scattering[20-22], and electron diffraction[23]. Magnetic properties have been studied through the capping-layer effect[24,2,4], ferromagnetic resonance (FMR)[25-33], A.C. susceptibility[34], Mossbauer spectroscopy[35,36], vibrating sample magnetometry[9], and Kerr rotation[37]. Although no direct measurements of dopant distribution have been published, studies have been made of their anneal-induced desorption.[8]

One conclusion drawn from this work is that the strain and damage are uniquely related to the energy deposited through nuclear collisions[1,38,39]. Generally, no crystallographic effects are attributed to the presence of the dopant. Another conclusion drawn is that the major connection between changes in magnetic and crystalline properties is magnetostriction,[40] promoting efforts to measure the magnetostriction constant of virgin and implanted crystals.[41-43] An apparent lack of correlation between strain and uniaxial anisotropy H_k at high doses has led to the hypothesis that implantation destroys the growth-induced anisotropy.[44] Other effects include changes in the saturation magnetization M, in the exchange stiffness A, in the Curie temperature T_c, in the cubic anisotropy H_1, and in the damping parameter α.[9,11,13,31,32,44] In the case of H^+-implanted garnet the unusually large variation of uniaxial anisotropy with dose[45] and annealing[8,33] has been attributed to either (1) qualitatively different damage caused by H^+ implantation,[46] or (2) chemical effects due to

the presence of H in the lattice.[8,33,47] Despite the relatively large number of papers devoted to implanted garnets, many of their basic features are unresolved. Part of this is due to difficulties of interpretation of experimental results and frequent failure to extract the maximum of quantitative information available in the experimental data.

In this paper we have combined X-ray diffraction and ferromagnetic resonance measurements of Ne^+, He^+, and H_2^+ implanted <111>-oriented Gd, Tm, Ga:YIG. This choice of implanted species and host material was made because of their (previously) widespread use in the manufacture of devices. More important, this material has the beneficent properties of reasonably narrow linewidth and high magnetostriction (70 Oe and $\lambda_{111} \sim -3\times10^{-6}$). The narrow linewidth permits a clear identification of mode location and amplitude in FMR, while the large λ_{111} ensures that a relatively large number of modes are supported in the implanted layer, thereby providing data with high information content. For each implanted species, doses were chosen to cover a range starting with easily-analyzed effects up to amorphousness. The incident ion energy produced implanted layer thicknesses of 3000 Å to 6000 Å. Selected samples were annealed up to 600°C.

We have attempted to answer the following questions: (1) Can FMR and X-ray diffraction yield detailed and unequivocal information about magnetic and crystalline properties for all levels of damage? (2) If so, what is the extent of correlation between magnetic and crystalline properties? The answer to the first question is a qualified yes. Concerning the second question, there is a strong although not total correlation between measured magnetic and measured crystalline properties.

II. Experiment

The garnet used was LPE-grown, <111>-oriented Gd,Tm,Ga:YIG. The substrate material was the usual single-crystal $Gd_3Ga_5O_{12}$ (GGG) wafer with a 5cm diameter

and 0.5mm thickness. Two wafers with films of identical nominal composition and very similar bulk magnetic properties were used, one (M721) for the neon and helium implantations, and the other (M722) for the hydrogen implantations. Two nominally identical, 4mmx4mm samples were made for each implanted species and dose. Implantation was done at room temperature. (See Table 1 for details). These three series of implanted samples were provided to us by an external source.[48]

In the determination of magnetic profiles for high doses, it was found useful to chemically etch some of the neon and helium implanted samples. A 30 min preanneal in air at 150°C produced no detectable changes in either FMR or X-ray diffraction. Following this, the sample was etched in hot (110°C) H_3PO_4. After cleaning with organic solvents, the sample was plunged in the acid and stirred for 5 to 10 seconds, followed by immersion in room temperature water. The sample was etched and measured with FMR or FMR and X-ray techniques in successive steps, up to the disappearance or near disappearance of the signal attributed to the implanted layer. The longest total etch time was 1 minute. The amount of material removed was determined with an accuracy of about ±50 Å from the X-ray rocking curve by inverting the process discussed in Ref. (7). Lateral nonuniformities attributed to uneven etching were detected by the broadening of both the FMR absorption spectrum and the rocking curve. The broadening increased with successive etch steps, but did not impair the X-ray determination of layer thickness. In the case of FMR, the broadening at the last two etch steps vitiated a meaningful measurement of some surface mode amplitudes, reduced the sensitivity for detection of weak modes, and increased the uncertainty in surface mode location from the usual ±5 Oe (unetched) up to ±150 Oe (last etch step). Other than nonuniform etching of the surface, we found no evidence of etch-induced changes in either crystalline or magnetic profiles. Selected unetched samples were annealed in air at temperatures ranging from 150°C to 600°C. in steps of 50°C. Due to the limited supply of samples, the same sample was annealed at progressively higher

Table 1

Some bulk properties of garnet and implantation schedule

Nominal composition		$\{Gd_{0.84}Tm_{1.17}Y_{0.99}\}$ $[Fe_2]$ $(Ga_{0.39}Fe_{2.61})O_{12}$
Nominal thickness	(μm)	0.95
$\lvert F_{444}\rvert$*		1074
$\lvert F_{888}\rvert$		974
$\lvert F_{880}\rvert$		1124
μ_{abs}	(μm^{-1})	0.117
$4\pi M$	(gauss)**	510

Wafer	Ion	Nominal Energy (keV)	Nominal Dose ($10^{13}/cm^2$)
M721	Ne^+	190	5
			10
			20
			30
			50
M721	He^+	140	300
			600
			1200
			2000
M722	H_2^+	120	200
			300
			500
			2000
			4000

Implantation current density $0.25\mu A/cm^2$

*Structure factors and normal absorption coefficient calculated from the composition.

**Calculated from magnetic bubble properties.

temperature in successive steps lasting 30 min each. FMR measurements were made every 50°C, while rocking curves were taken every 100°C.

Double crystal, Bragg case, X-ray rocking curves were taken under the conditions described in Ref. (7). The X-ray source line was Cu Kα with an incident beam counting rate of 10^5cps. The spot size at the sample was limited to ∿ 1mm x 1mm by a set of slits. All as-implanted samples were measured using the (444) reflection. In certain cases described below, the (880) $\gamma_o > |\gamma_H|$, and the (880) $\gamma_o < |\gamma_H|$, reflections were also used. For the annealed samples, especially for annealing temperatures greater than 350°C, the (888) reflection was used because of its sensitivity to low strain. Measurements repeated up to several months apart produced practically identical rocking curves.

Ferromagnetic resonance measurements were made at a fixed frequency of 9.5 GHz with the usual combination of rectangular cavity, microwave bridge, and modulated external applied field. All measurements were made at room temperature without a temperature controller. Both perpendicular and parallel FMR configurations were used for each sample. For some samples FMR spectra as a function of polar angle were also taken. The reproducibility of mode location and amplitude determination was ±5 Oe and ±2%, respectively, for measurements repeated within a few hours. However, spectra taken several days apart at times showed systematic differences up to 50 Oe in mode location, without appreciable changes in mode amplitude. We attribute these variations to differences in room temperature, since one can observe shifts of several hundred Oe by blowing warm (T∿50°C) air into the cavity. We do not consider the observed variations to be significant, since the range of applied field in which the modes are excited spans several thousand Oe.

III. Theoretical Considerations

It is perhaps inappropriate to include here a qualitative description of

the basic processes of ion implantation. The major purpose of this paper is to present experimental results. However, the impression formed by reading the literature on ion-implanted garnets is that different authors assign different meanings to the same words. At the risk of belaboring the point, we wish to give a precise description of what we think we are measuring.

During ion-implantation the incident ions undergo collisions with target atoms. Since the ion beam is aimed in a non-channeling direction, the crystallographic structure of the target plays only a minor role in determining the scattering process. The parameters which enter the expression for this process are the masses and nuclear charges of the ion and target atoms, the density (number of each kind of atom per unit volume) of the target, its electronic density, and the kinetic energy of the ion beam.[49] Since the ions continuously lose energy as they penetrate the crystal, the energy dependence becomes at least statistically a depth dependence. Due to the low electron mass, collisions with electrons remove energy but do not contribute to damage.[49] For typical implantation in garnet at a few hundred keV, the number of nuclear collisions per ion is several hundred.[46] At each collision the transferred energy ranges from zero up to a value determined by the kinetic energy of the ion and the ion-target mass ratio. If the transferred energy is sufficiently large, the target atom will be ejected from its original site and may in turn eject other atoms. Thus for each incoming ion there is a cascade of recoil atoms (a thermal spike). The mean free path of the ion is sufficiently short[46], so that even for the lowest doses we are considering ($\sim 10^{13}/cm^2$ for Ne^+ and $\sim 10^{15}/cm^2$ for He^+ and H_2^+), at least one atom from almost every unit cell has been displaced by more than one interatomic spacing. Atoms surrounding either the vacancy or the interstitial atom are no longer located in perfect-crystal sites. Since an interstitial and a vacancy are not equivalent, it is plausible that in the implantation region the atoms are no longer packed as closely as in virgin crystal. This is the positive strain uniformly observed in ion-implanted crystals with

widely different properties, such as Si, GaAs, and GGG.[7,50]

If the displacement of a particular atom j is $\Delta\vec{r}_j$, then there is a probability distribution $\rho(\Delta\vec{r}_j)$ which describes the frequency of these incoherent displacements. For a polyatomic crystal, such as garnet, one expects that each set of equivalent sites, occupied by a particular atomic species, has its own $\rho(\Delta\vec{r}_j)$, each contributing in a different way to the total (coherent) strain. For ion doses below that required to render the crystal amorphous, the unit cell is still recognizable. The registry between the implanted layer and the underlying undamaged crystal is maintained. It constrains the average unit cell to expand only in a direction perpendicular to the film surface.[7] The implanted layer is therefore in lateral compression and the total normal strain includes a Poisson (elastic) contribution. The compressive stress may act as a source of energy for the creation of extended defects. If the stress is sufficiently large, stress-reducing dislocations may form.[51] Such an occurrence is accompanied by the loss of strict registry between highly stressed and less stressed regions of the crystal.

Up to now we have not considered any crystallographic effects due to the presence of the implanted dopant. Although a priori it is not possible to exclude the dopant as a contributor to the total strain, experimental results strongly suggest that only the damage is effective. For the same strain, the doses for neon vs. helium differ by one and a half orders of magnitude,[1,39] conforming to the difference in nuclear stopping power. The hypothesis that damage is the source of the strain is further confirmed in Ref. (39), where the detailed strain distribution was found to agree closely with the calculated distribution of energy deposited in nuclear collisions, but not with the ion range. Our present results, discussed below, suggest that in the case of hydrogen implantation there is a detectable strain associated with the ion range.

X-ray diffraction can detect and separate the implantation-induced damage components: point defects, strains, and extended defects. Point defects change

the value of the structure factor. If they are incoherent, the magnitude of the structure factor is diminished. This decrease is determined by the displacement functions $\rho(\Delta\vec{r}_j)$ belonging to each site j. We make the simplifying and physically plausible assumption that these functions are spherically symmetric gaussians described by their standard deviations U_j. A further simplification is that, at a given depth, $U_j \equiv U$ is the same for all sites. For the reflections used in this work, the c-sites, occupied by Gd, Tm, and Y, are the dominant contributors to the structure factor. Thus the experimental value of U refers mostly to these atoms. The sensitivity to a- and d-sites, occupied by Fe and Ga, is much less (20% to 40%, depending on the reflection), and the sensitivity to h-sites, occupied by O, is practically zero.[7]

The definition of strain used in this work is the fractional change in lattice parameter with respect to that of virgin GGG crystal. The strain may have a component $\varepsilon^{\perp}$ in a direction perpendicular to the film surface and a lateral component $\varepsilon^{||}$. In general, both $\varepsilon^{\perp}$ and $\varepsilon^{||}$ change the magnitude and the direction of a particular reciprocal lattice vector. These changes are related to the measurable change in the angular location of the Bragg peak.[7] X-ray diffraction alone gives no information on stress.

Detailed information about extended defects is much more difficult to extract from the rocking curve. If they occupy a sufficiently small volume, they are indistinguishable from point defects. If the extended defects involve gentle, long-range ($\sim$ 1μm radius) distortion of the lattice, then they result in a broadening of the rocking curve. In this case, the mosaic-crystal theory[52] may be used to obtain estimates of their size, misorientation, and lateral variation in strain.[5,50]

The relationship between point defects, strain, extended defects, and dopant chemistry on one hand, and magnetic properties on the other, is poorly understood. We are not aware of any "first-principles" theoretical framework which would

attempt to relate magnetism to the chemistry and geometry of implanted crystals. At low doses there is an approximately linear relationship between the shift in location of the FMR principal surface mode and dose, strain or stress. The proportionality constant roughly corresponds to the magnetostriction constant determined by external elastic deformation of the virgin crystal. At higher doses the mode shift is no longer simply related to any of these. In some of the references a correlation is attempted in which the mode shift is equated to a change in H_k which is then related to the dose or maximum strain. This is erroneous for several reasons. The most important of these is that H_k saturates and decreases in regions of high damage so that the mode is localized and measures the change in H_k at a point far from the point of maximum strain. It is not clear whether the changes in other magnetic properties, such as M, A, H_1, γ, and α are due to strain or damage or chemistry, or a combination of all. Even worse, the magnitudes of these changes versus ion species, dose or depth are also poorly known. Ferromagnetic resonance spectra, when interpreted according to the model presented in Ref. (31), provide information about profiles of these magnetic properties.

IV. The Fitting Procedure

Crystalline profiles and magnetic profiles are obtained from the rocking curve and the FMR spectrum, respectively. Unfortunately, neither technique as presently used can directly yield the desired profiles from the respective measurement. Both techniques rely on choosing a trial distribution, calculating the corresponding spectrum, and comparing it to the experimental data. Since the spectra characteristic of various classes of profiles (unimodal vs. polymodal, constant or increasing or decreasing with depth, etc.) have already been calculated, these serve as a guide in choosing the initial distributions. A trial and error procedure is then used until a satisfactory fit is obtained. A more sophisticated approach is the use of Jacobians to determine the changes in profile

for a better fit. However, combination of this with least-squares fitting procedures has been singularly unsuccessful in converging to a satisfactory fit.

In the rocking curve, the angular range of nonzero reflecting power establishes the maximum strain, the most rapid oscillation establishes the total layer thickness, the area under the curve establishes the thickness-averaged structure factor; and the degree of smoothing is related to extended defects.[7] In the kinematical regime, the rocking curve and the strain and damage distributions are related through a Fourier transformation. However, the lack of phase detection precludes a direct inversion of the rocking curve.

In perpendicular FMR, the location of the highest mode yields an estimate of the maximum field for local uniform resonance H_{un}; the total number of surface modes yields an estimate of the ratio $A/(MT^2)$, where T is the layer thickness; the linewidth is linearly related to the damping parameter α; the relative amplitudes of the principal surface and body modes yield a value for surface to bulk magnetization ratio.[31,53] Some of this information is repeated in a different form for parallel FMR.

For both X-ray and FMR analyses the accuracy and uniqueness of a resulting distribution depend on several factors: the information content (i.e. structure) of the experimental data, the sensitivity of the experimental data to variations of the quantity in question, the extent to which other parameters produce similar effects and of course the accuracy or quality of the fit that is demanded. The interpretation of the rocking curve is less ambiguous than the FMR spectrum since the rocking curve depends very strongly on only one parameter, the strain distribution. The damage distribution though required for a fit at high doses and strain has a much smaller effect. As a consequence the strain profile can be quickly obtained with an apparent high accuracy, while the damage profile is less certain. Without a formal proof, it remains our opinion that the strain distribution corresponding to a given rocking curve is unique, except for mirror reflections. Typically the strain distribution is determined everywhere to a

precision of a few percent of the maximum strain, and ±2% at the peak. The depth resolution is 50 to 200 Å depending on the particular distribution.

We describe the damage distribution by U the standard deviation of an assumed gaussian distribution of random atomic displacements. The local structure factor has an exponential dependence $|F| \sim e^{-kU^2}$, and so the parameter U becomes a dominant factor in regions of high damage and has no effect in regions of low damage.[7] In a later section it will be shown that a linear relation between U and strain gives the best fit but that the proportionality constant varies with implant element. Thus the value of this constant is determined by the fitting process for medium to high doses.

For the samples studied here, the number of surface modes excited by perpendicular FMR ranges from 1 to 11. If their locations and amplitudes are used as inputs, there are from 2 to 22 data points. The major parameters which determine mode locations and amplitudes are the field for uniform resonance H_{un} and the ratio $\frac{A}{M}$. When several modes are present, the FMR spectrum appears to be uniquely related to the distribution of H_{un} provided this distribution is unimodal. In such cases the precision of the determination is within a few percent of the maximum everywhere, and ±3% at the peak. For unimodal distributions, the depth-averaged A/M is also determined to ±10%, but the sensitivity to the shape of this distribution is relatively poor. The same remarks apply to the distribution of M. Parallel FMR is used to separate the various components of H_{un}. However the resolution of parallel FMR is less than half that of perpendicular FMR, and the overlap of modes vitiates accurate amplitude measurement.[31]

If the magnetic profiles are polymodal, we are unable to determine a unique profile from a single set of spectra. One must then resort to etching (or preferably ion-milling, since it removes the material more uniformly) and reconstruct the profiles as described in Ref. (31). The etch - or milling-steps must be small (100 to 200 Å) since larger etch-steps leave room for multiple

interpretations of the spectra. The above discussion suggests the fitting procedure we followed.

For all samples the strain and damage profiles were first obtained. Magnetic profiles were estimated by assuming a unique relationship to exist between ΔH_{un} and $\Delta\varepsilon^{\perp}$ for each implanted species. For neon and helium, this relationship was immediately shown to be linear at low doses with a clear saturation of ΔH_{un} for what we term medium doses. In this range the saturation can be represented empirically or by some convenient mathematical form. We found it convenient and satisfactory to assume a form

$$\Delta H_{un} = K[\Delta\varepsilon^{\perp} - b(\Delta\varepsilon^{\perp})^3] \qquad (1)$$

The magnitudes of the linear and cubic terms were adjusted to give a best fit to the spectra for all low to medium doses.

The assumption that ΔH_{un} and $\Delta\varepsilon^{\perp}$ are uniquely related was not arbitrarily made. In previous publications, the authors have separately studied the same low-dose He-implanted garnet with properties similar to those of some of the present samples. The magnetic profiles were determined by one of the authors[31] independently of any X-ray results, and the crystalline profiles were obtained by the other author[7] without FMR inputs. Upon comparison, the ΔH_{un} and $\Delta\varepsilon^{\perp}$ profiles agreed with each other to ±2% of the peak values.

Various features of the FMR spectra imply differences in surface and bulk values of other magnetic parameters. Differences in the linewidth require a change in α; relative mode amplitudes may dictate a change in M; comparison of $\perp$ and $\parallel$ modes may require a change in H_1 or γ; FMR as a function of polar angle about $\langle 1\bar{1}0\rangle$ axes places limits on the allowed changes in H_1. However there is relatively poor sensitivity to the actual profile shape of these magnetic properties. A convenient assumption that is consistent with experimental data is that these changes are also linearly related to $\Delta\varepsilon^{\perp}$. The peak value for each

distribution is then independently adjusted to fit the appropriate spectrum.

In the case of low to medium doses of neon and helium, this approach produced excellent fits to the FMR spectra. For all arbitrary deviations from this relationship that were tested, the quality of fit rapidly deteriorated. At very high doses the structure of the FMR spectra changed so radically, that we were unable to use the strain data to obtain magnetic profiles. In this dose range the bimodal profile of H_{un} was determined independently of strain, and with reduced precision by etching and using the methods of Ref. (31).

For the samples implanted with hydrogen, the assumption of a unique relationship between ΔH_{un} and $\Delta\varepsilon^{\perp}$ was immediately shown to be false. Nevertheless, since the magnetic profiles are unimodal, they could be obtained directly from the FMR spectra, without the need to resort to etching.

V. Results and Discussion

A. Experimental and calculated spectra

Since neither rocking curves nor FMR spectra corresponding to a wide range of doses of ion-implanted garnets have been published, we include here some of our experimental data. In addition to showing their structural peculiarities, the figures include calculated spectra showing the quality of fit that is obtainable. For this quality of fit the distributions of $\Delta\varepsilon^{\perp}$ and ΔH_{un} have the accuracy quoted earlier except for high doses where portions of the film become amorphous or paramagnetic.

Figures 1a, b, and c, respectively, show the experimental (dashed) and calculated (solid) rocking curves for several doses of Ne^{+}, He^{+}, and H_2^{+} implanted garnet. All three sets have several features in common: the single sharp peak near the origin corresponding to diffraction by the deep, unimplanted, bulk portion of the film; the oscillatory structure which extends to lower angles and becomes less intense with increasing dose; and the envelope shape

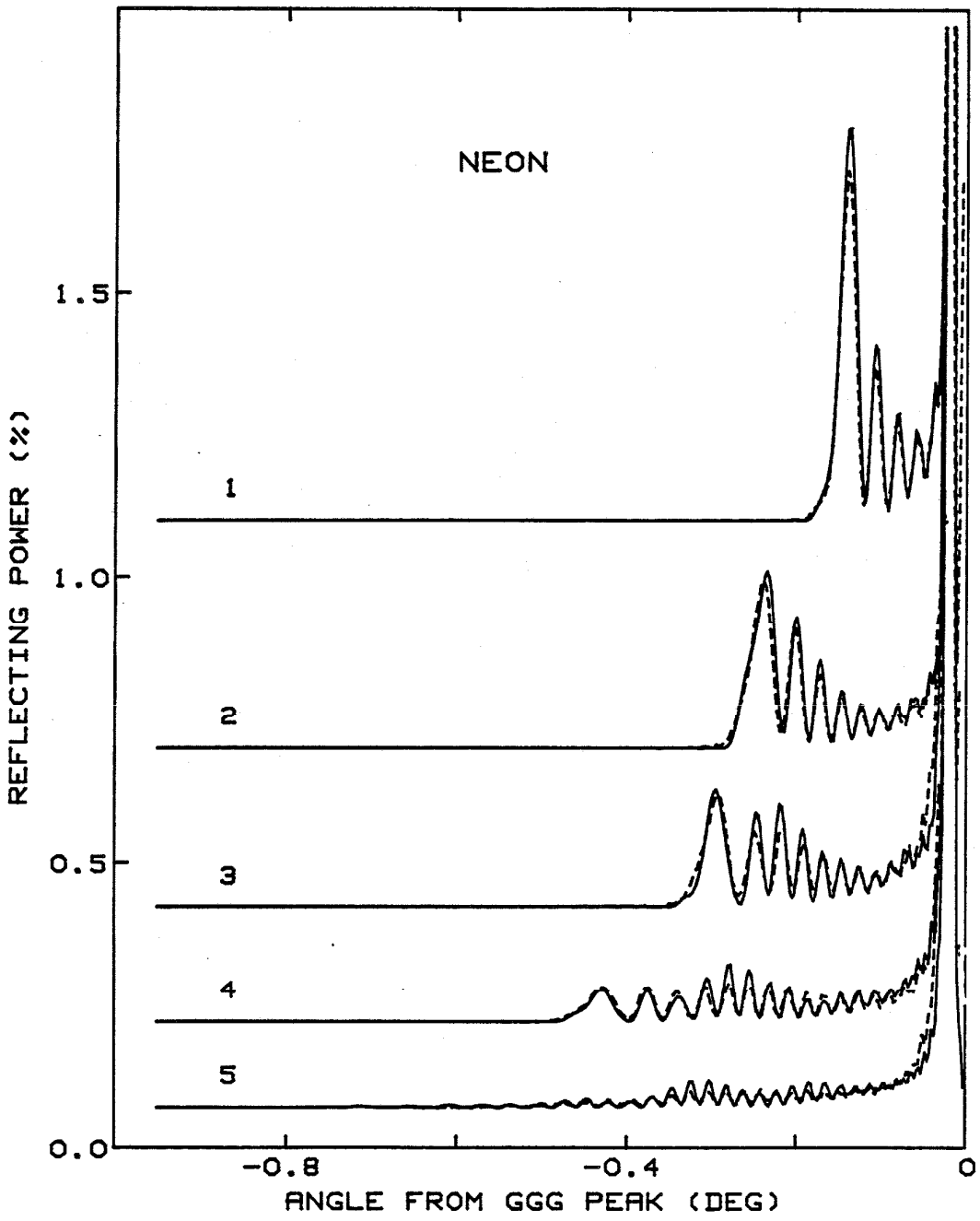

Figure 1(a). Measured (dashed line) and calculated (solid line) Cu K_α (444) rocking curves for 190 keV Ne^+ implantation. Doses are 0.5, 1.0, 2.0, 3.0 and $5.0 \times 10^{14}/cm^2$ for curves 1 through 5, respectively.

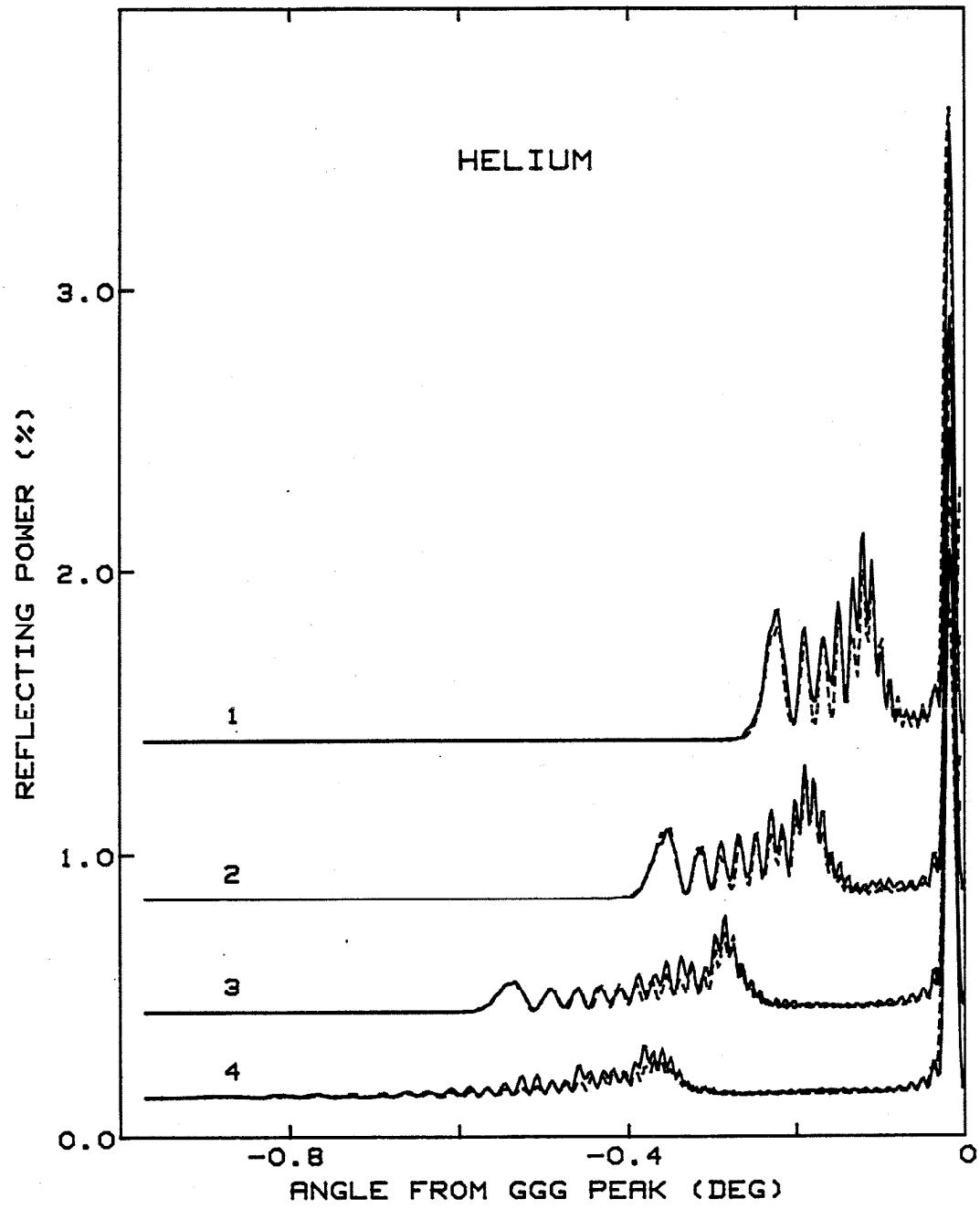

Figure 1(b). Cu K_α (444) rocking curves for 140 keV He^+ implantation. Doses are 3.0, 6.0, 12, and $20 \times 10^{15}/cm^2$ for curves 1 through 4, respectively.

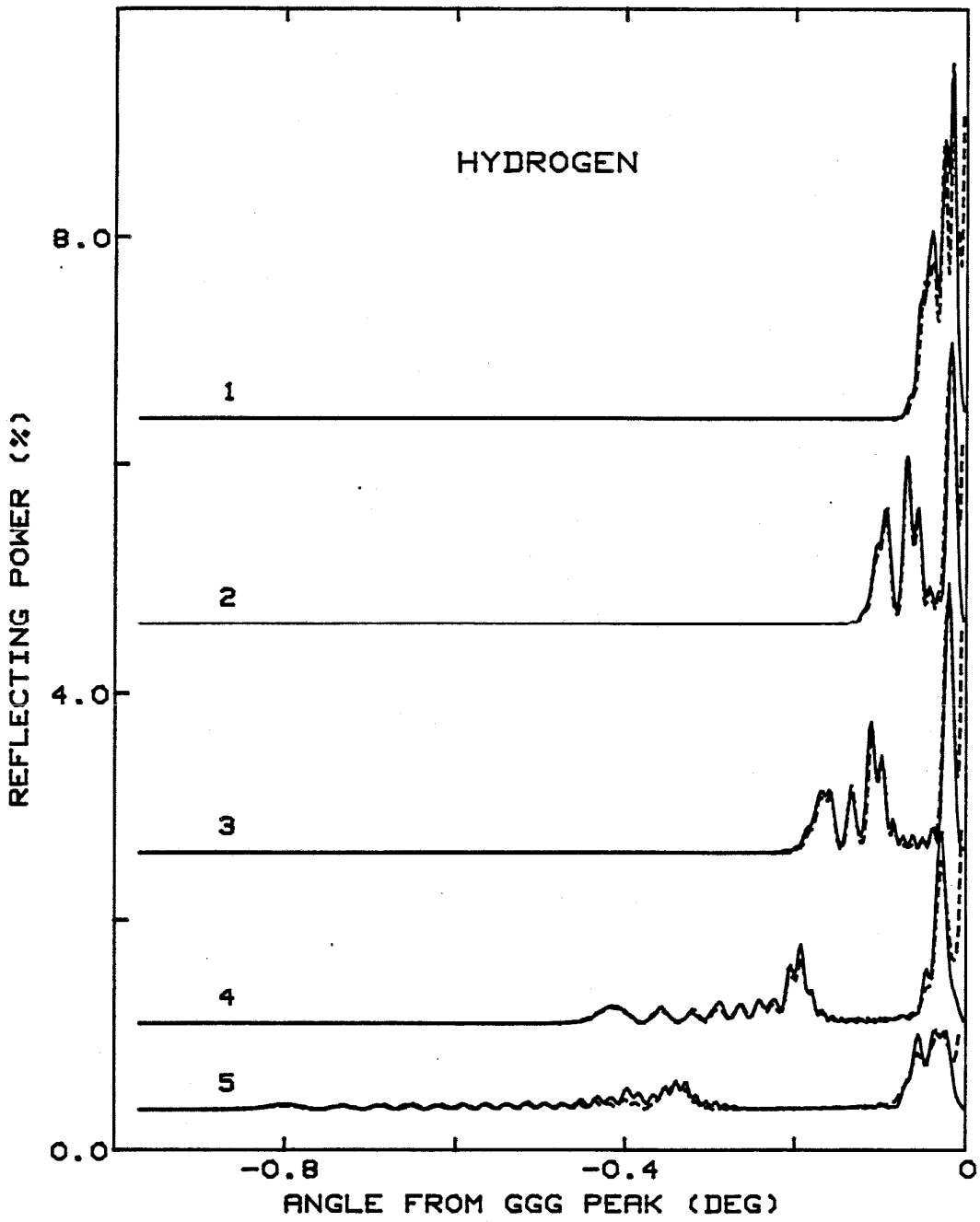

Figure 1(c). Cu K_α (444) rocking curves for 120 keV H_2^+ implantation. Doses are 2.0, 3.0, 5.0, 20, and $40 \times 10^{15}/cm^2$ for curves 1 through 5, respectively.

characteristic of unimodal distributions. For all cases shown, the calculated plane-wave solution was convolved with the incident beam, whose angular divergence distribution is approximated by a gaussian with a standard deviation of 8 arcsec.

Figures 2a, b, and c, respectively, show the perpendicular FMR spectra for the same samples. The spectra are presented in stick-diagram form, the solid and open rectangles corresponding to measured and calculated modes, respectively. For clarity, the modes (experimental and calculated) are shown adjacent to each other, without overlap. The actual field is located at their boundary. The discrepancy between calculated and measured mode location is as a rule less than ±10 Oe, rarely becoming as large as 50 Oe for some of the high dose cases. Mode amplitudes are indicated by the relative height of the rectangles. Experimental modes with amplitudes less than 10% of the principal (or first) surface mode, and nearly zero amplitude theoretical modes where no experimental mode is seen, are also indicated by vertical arrows. The 50 Oe width of the rectangles does not reflect the actual mode linewidth, which increases with dose from 70 Oe (bulk modes) up to ∿150 Oe (surface modes for highest doses).

Only spectra for the three lowest doses of hydrogen implantation are shown in Fig. 2c. The higher-dose spectra were excluded because the lineshape of some of the modes indicated that the static magnetization was not completely aligned with the applied field. For sufficiently large surface anisotropy field, this occurs for applied fields above but near the bulk mode. Although surface modes exist in this situation, their characteristics cannot be calculated accurately by the methods used in this study.

The depth-dependence of the r.f. magnetization in FMR provides a convenient classification of modes. In the present figures, the largest mode, occurring at ∿3750 Oe, is the main bulk mode, while modes at lower fields are predominantly sinusoidal bulk spinwave modes. The modes found at fields above the main mode

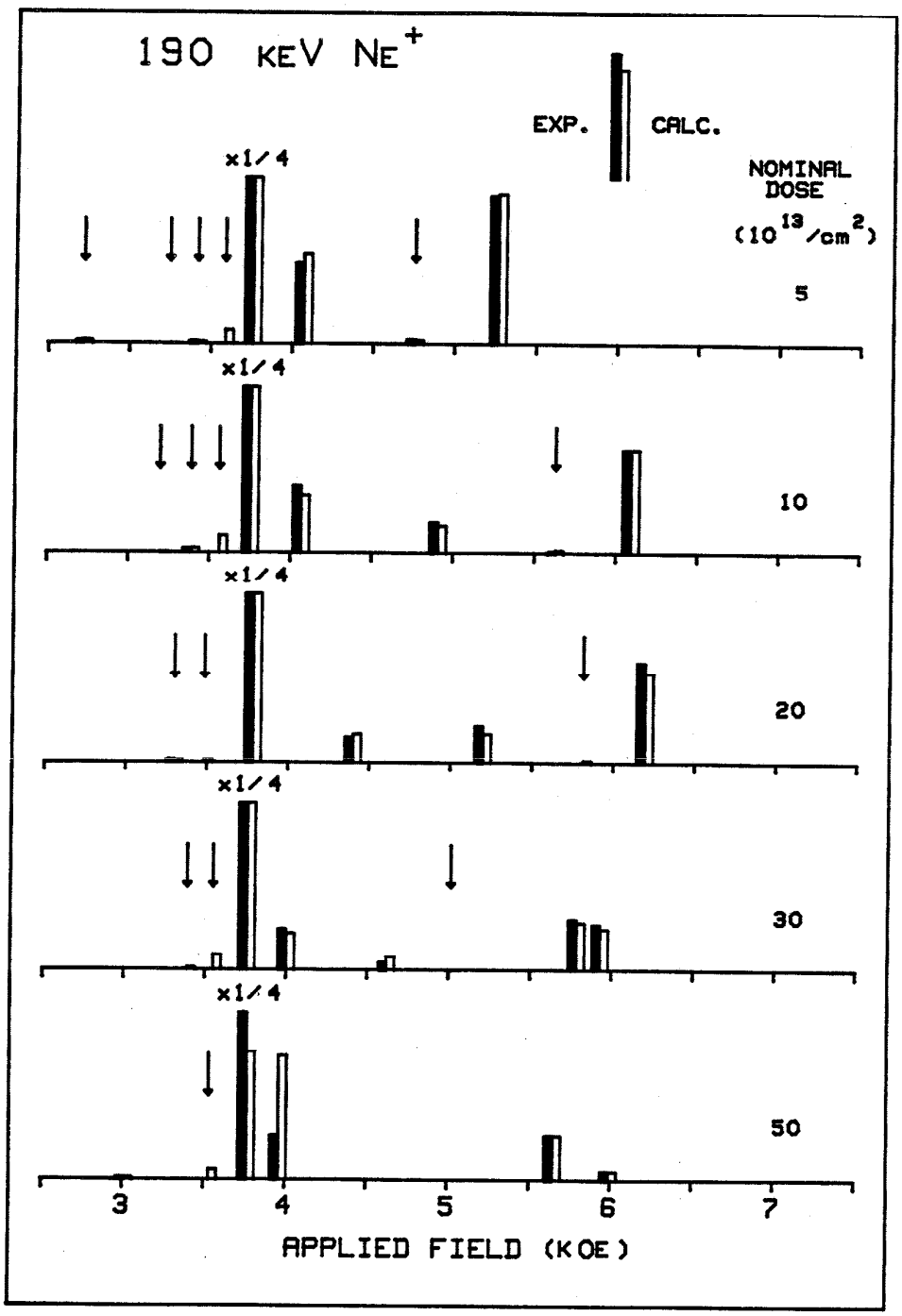

Figure 2(a). Measured (solid rectangles) and calculated (open rectangles) ⊥ FMR spectra for the Ne^+ samples of Figure 1(a).

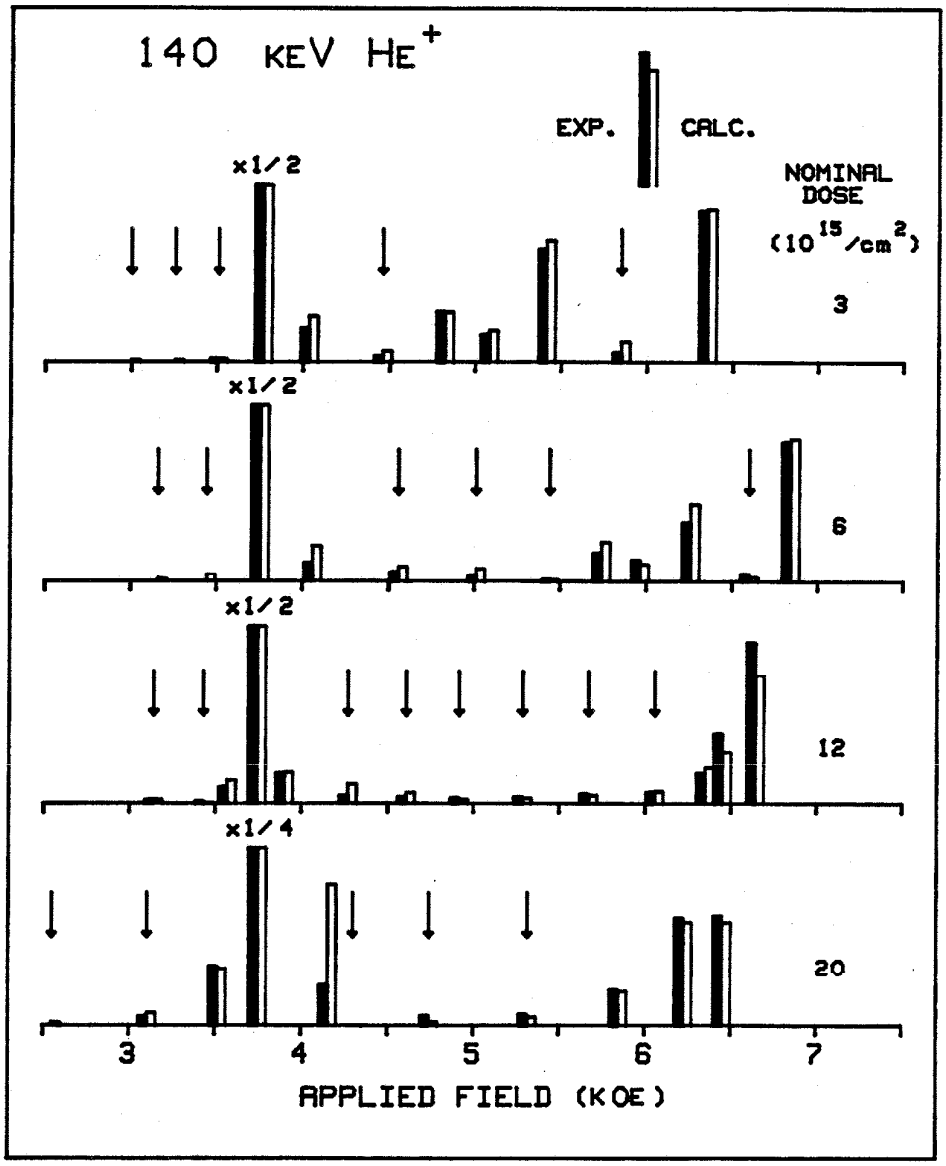

Figure 2(b). ⊥ FMR spectra for the He^+ samples of Figure 1(b).

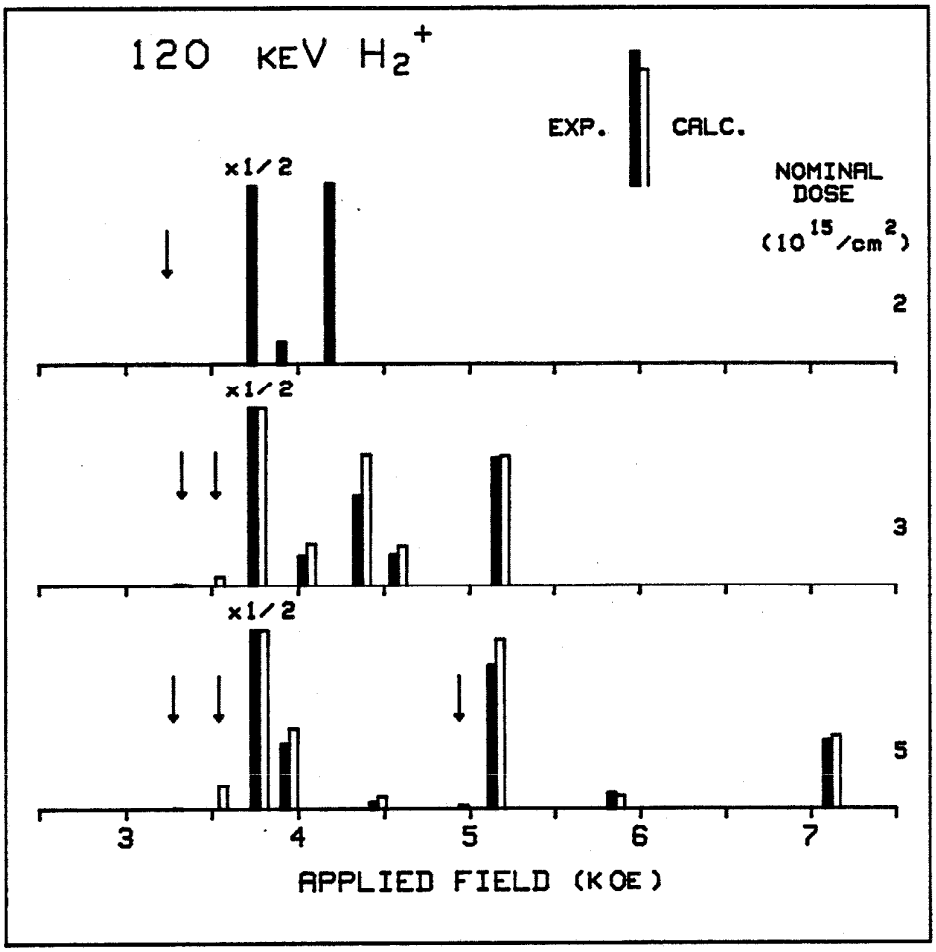

Figure 2(c). ⊥ FMR spectra of the three lower dose H_2^+ samples of Figure 1(c).

are largely confined to the implanted layer and are called surface modes.[31] For low doses, the amplitudes of the surface modes generally follow an alternating large-small sequence which is characteristic of certain unimodal distributions of H_{un}.[53] This is seen for the lowest three neon doses, the lowest two helium doses and all three hydrogen doses.

An important feature is observed on comparing the spectra for the lowest and highest doses in the neon and helium series. Although the nominal doses vary by an order of magnitude, the separation between the principal surface and bulk modes changes by less than 30% in both cases. However the high dose spectra have a drastically different character. In these cases the magnetic profiles become bimodal. The details of the bimodal profiles could only be elucidated by analysis after progressive etching.

The bimodal character was first established for the third helium implant with dose $1.2 \times 10^{16}/cm^2$. This case showed at least ten surface modes in a complex spectrum unlike anything seen in earlier work. The development of this spectrum with etching was even more bizarre as seen in Fig. 3a. Mode locations are indicated by circular symbols (or elliptical symbols for less certain locations); mode amplitudes are given at selected depths. Question marks indicate amplitudes uncertain by more than a factor of two. Also shown are the cumulative etch-time intervals, and vertical arrows which indicate depths obtained by analysis of X-ray rocking curves. The unetched spectrum is identical to one of the spectra in Fig. 2b. The evolution of this spectrum with etch depth is quantitatively and qualitatively different from that of a lower dose, but identical energy, He^+ implantation in a similar garnet (see Figure 5 of Ref. (31) for a comparison).

Figure 3b shows the calculated spectrum for the etched sample. To obtain this structure it was necessary to use a bimodal profile for H_{un} with extreme variations in magnetic profiles to be discussed below. Although there are small discrepancies of detail between Figures 3a and 3b, the sensitivity of the

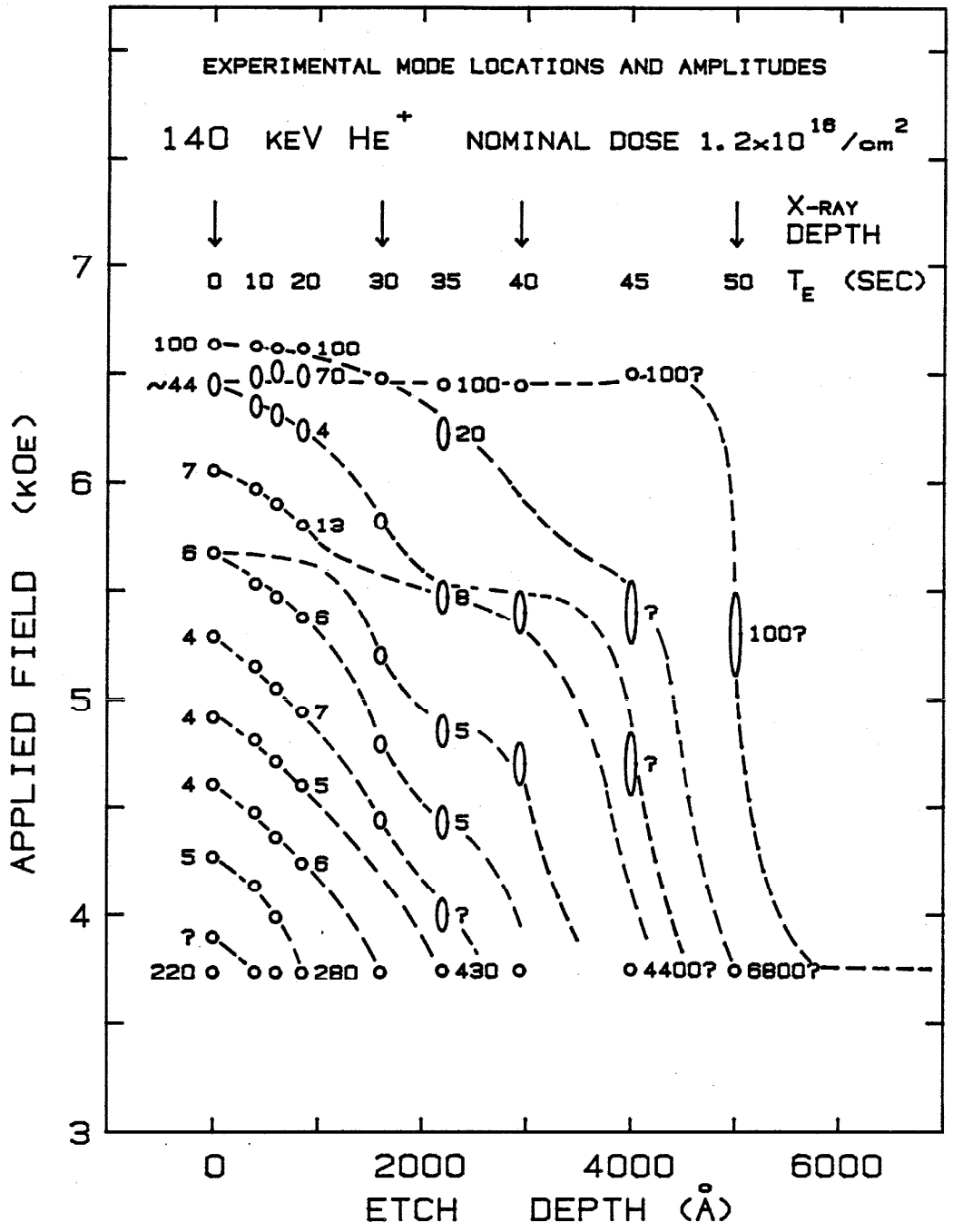

Figure 3(a). Experimental ⊥ FMR spectrum versus etch depth for the sample implanted with 140 keV He^+, $1.2x10^{16}/cm^2$.

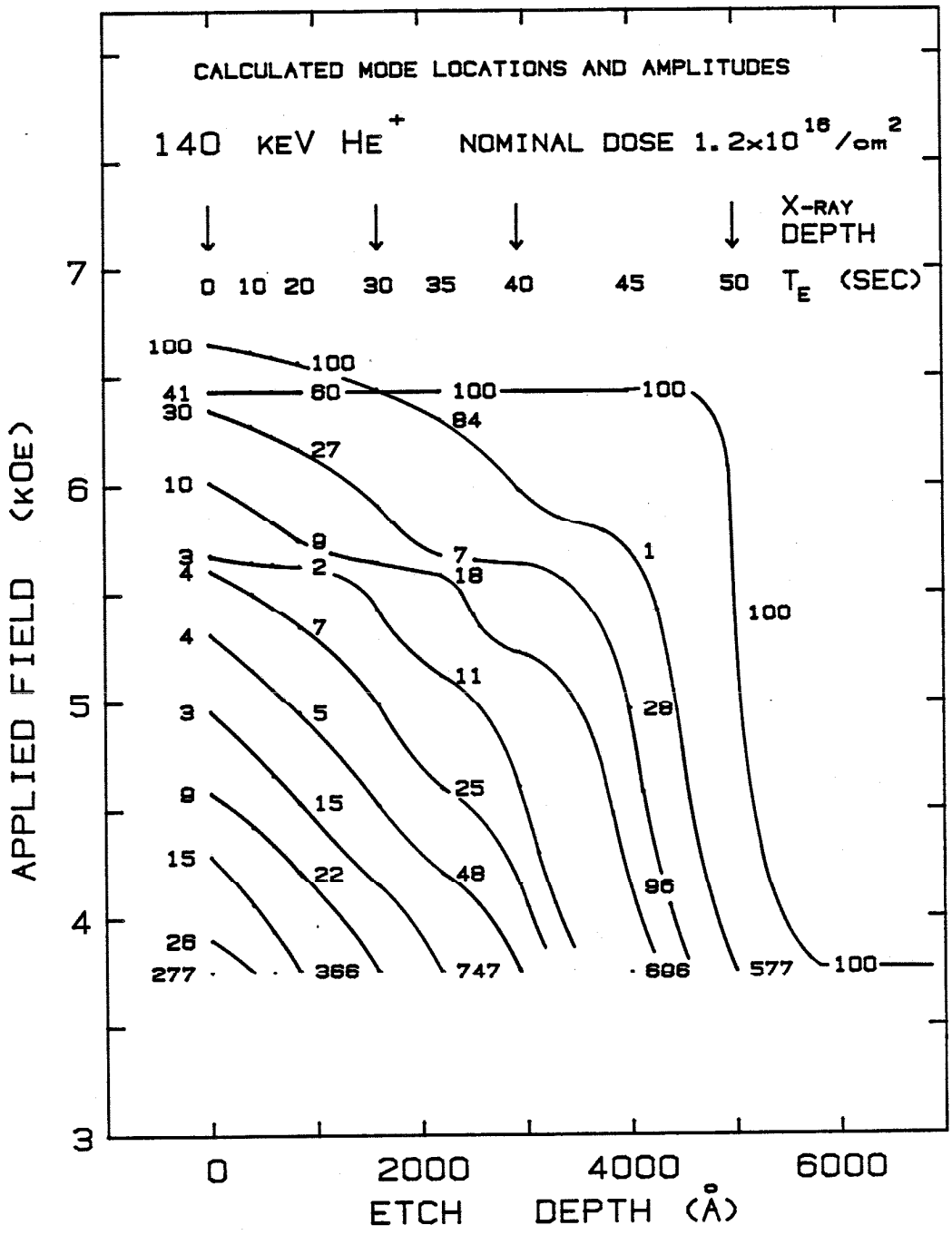

Figure 3(b). Calculated ⊥ FMR spectrum corresponding to Figure 3(a).

calculated spectrum to the extreme variations in magnetic profiles is so large that we accept this result as sufficiently accurate.

In addition to this case, the etching and fitting procedure was repeated for the neon implantation with dose $3 \times 10^{14}/cm^2$. A similar profile was required and the quality of fit is similar to that shown in Figures 3a and 3b.

B. Profiles of Perpendicular Strain

The strain profiles obtained from the rocking curves of Figure 1 are shown in Figures 4a, b, and c for Ne^+, He^+, and H_2^+ implantations, respectively. In each figure the distributions are labeled to show correspondence with the appropriate rocking curves. Since the (444) reflection used is symmetric about the film normal, only the perpendicular strain is measured. The unimplanted region shows an as-grown component of strain. Assuming that for any single wafer this strain is constant and independent of location on the wafer, the small spread observed in the measured value verifies the reproducibility of experimental rocking curves stated earlier. The implanted regions shown on the left in these figures have thicknesses which depend on implanted species and energy. For computational convenience the distributions are represented in laminar form, the number of laminae being approximately the minimum required for a good fit.[7] This number increases with increasing strain, as seen in the figures.

For each species the general features of the profiles conform to expectations based on LSS theory. Going from Ne^+ to He^+ to H_2^+ the distributions become sharper and increasingly asymmetric about the maximum strain. The magnitude of the maximum strain below amorphousness is about 2.5% for Ne^+, 3.4% for He^+ and 3.9% for H_2^+. For each species the surface strain is less than half of the maximum strain. The thicknesses of the strained layer are 3300 Å, 5800 Å and 4900 Å, respectively. The total thickness, including the bulk region, is 9200 Å for the Ne^+ and He^+ implanted wafer, and 8400 Å for the H_2^+ implanted wafer. Both

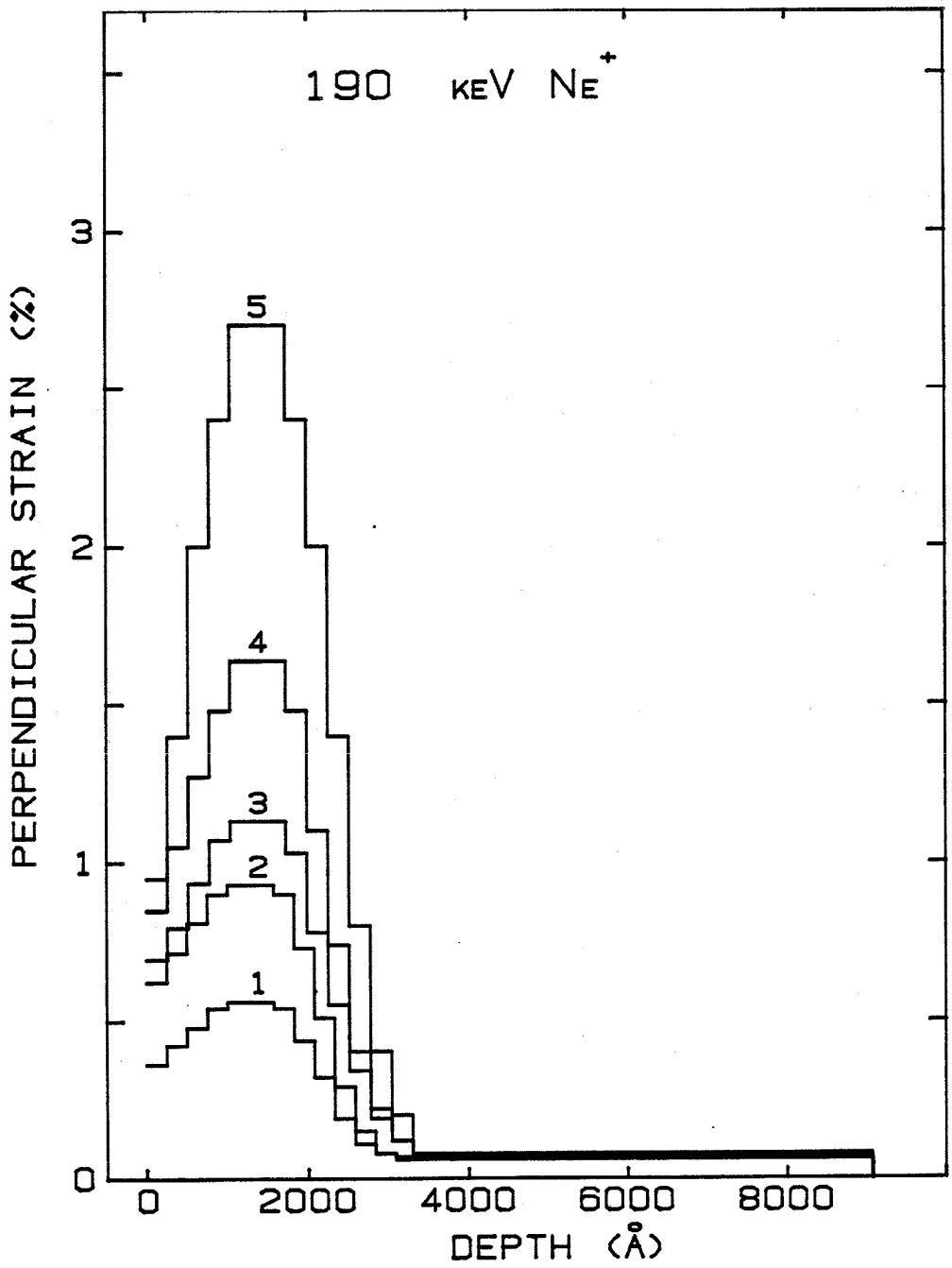

Figure 4(a). Perpendicular strain profiles of Ne^+ implanted samples. The distributions are labeled to show correspondence with the rocking curves of Fig. 1(a), from which they were obtained.

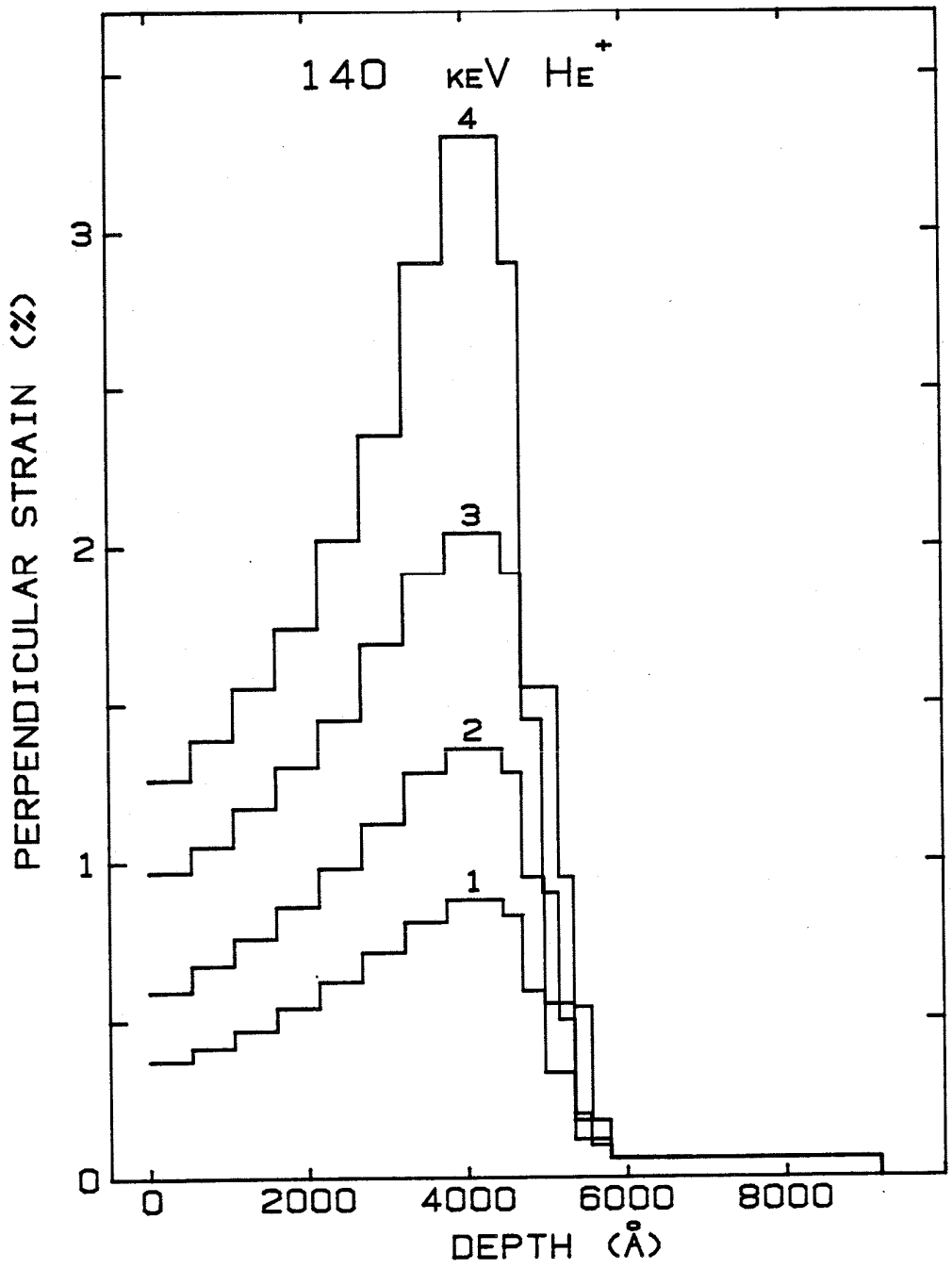

Figure 4(b). Perpendicular strain profiles of He^+ implanted samples.

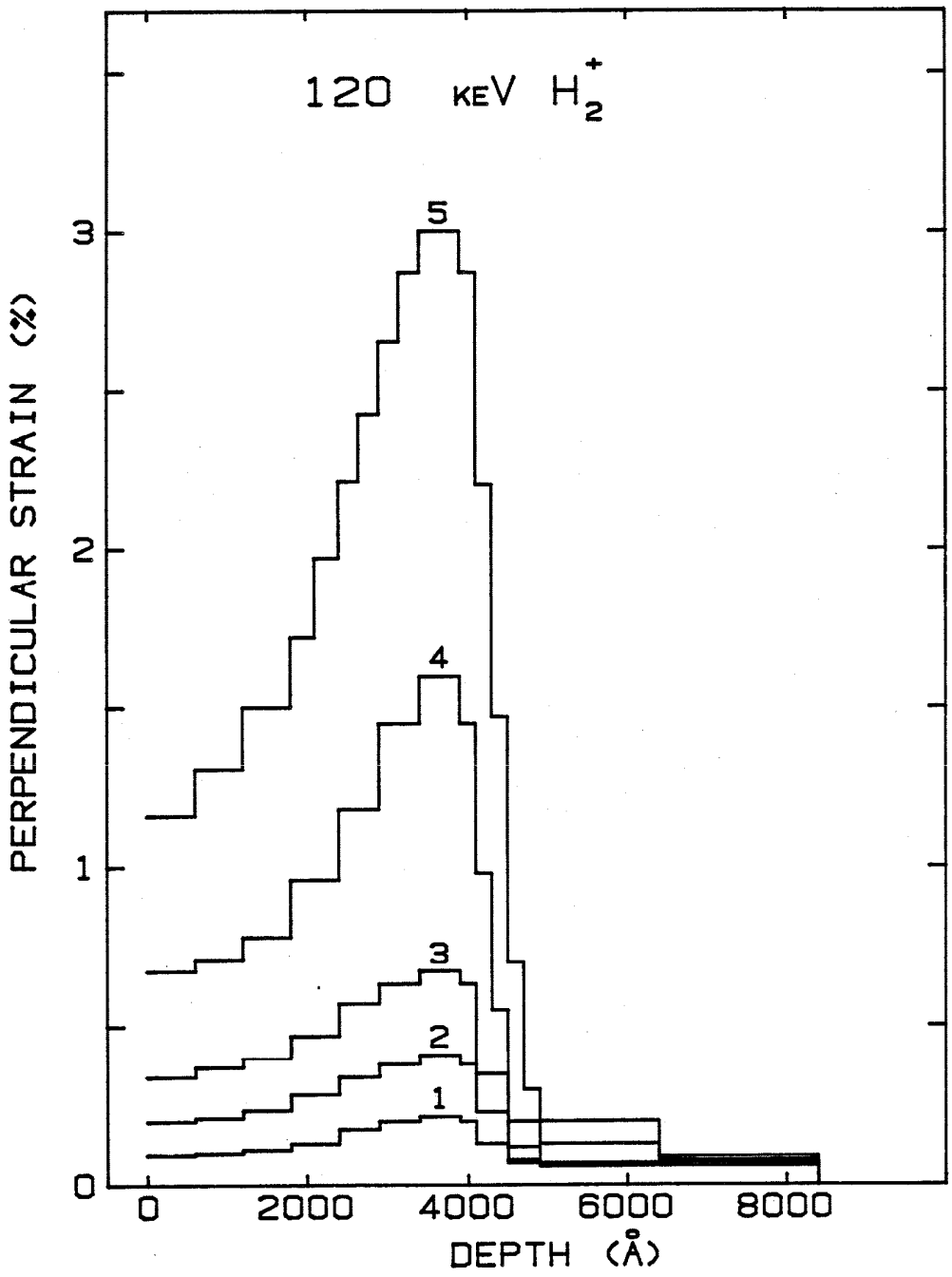

Figure 4(c). Perpendicular strain profiles of H_2^+ implanted samples.

values are in reasonable agreement with the approximate values determined optically by the supplier.

For the two highest doses of H_2^+ implantation (Figure 4c, distributions 4 and 5), our resolution is sufficient to show that the presumed bulk region is not really uniform. A two-layer representation of the strain profile in the bulk is shown since the resolution does not permit greater detail. The variation shown is required to fit the low-angle features of the rocking curve. The difference in strain between the two layers increases in proportion to the maximum strain . This behavior as well as the thickness and location of the region of higher strain leads us to conclude that the increased strain is due to the presence of implanted hydrogen. For 120 keV H_2^+, according to theory most of the stopped hydrogen atoms are located in a region about 2000 Å wide at a distance of 4500 Å from the surface.(54) The region of increased strain in the bulk region is consistent with this calculation. For these doses, the relative atomic concentration of hydrogen is 2% to 4%, and the presumed dopant-induced strain is 4% of the maximum strain induced by damage. This relation may hold for other implanted species but cannot be determined by the rocking curve method. For other dopants the implanted layer is rendered amorphous for doses corresponding to dopant concentrations well below 1%.

For each implanted species there are two curious features involving the relation between maximum strain and dose, and the ratio of surface strain to maximum strain. First, the maximum implantation-induced strain $\Delta\varepsilon^{\perp}_{max}$ does not behave smoothly as a function of nominal dose. For example, the values of $\Delta\varepsilon^{\perp}_{max}$ in Figure 4a are in the ratios 1 :1.8 :2.1 :3.2 :5.4. The normalized nominal doses form a different sequence 1,2,4,6 and 10. For hydrogen (Figure 4c), the values of $\Delta\varepsilon^{\perp}_{max}$ are in the ratios 1 :2.3 :3.9 :9.8 :18.8 while the normalized nominal dose sequence is 1, 1.5, 2.5, 10 and 20. Data for helium are also inconsistent but in a third way. If the nominal doses are taken at face value, there is no

discernible unique relationship between maximum strain and dose. Since implantation was done in another laboratory, we are unable to assess the accuracy of the doses. The second feature is that the detailed shape of the strain distribution (in particular the ratio of surface strain to peak strain) does not show a systematic trend with increasing dose. Fortunately the existence of pairs of nominally identical samples for each species and dose has enabled a partial resolution of this puzzle. The rocking curves obtained from each pair of samples are in most cases decidedly different giving rise to an inconsistency in the ratio of surface to peak strain. While the maximum strain values for each pair do not differ by more than 15%, a discrepancy develops between this region and the surface, becoming as large as 250% at the surface. It was gratifying that this same inconsistency was found in the FMR spectra and their corresponding H_{un} profiles. The lack of systematic trend mentioned above is simply a continuation of this inconsistency. The actual reason for these variations in strain and magnetic profiles for nominally identical samples remains unknown. This inability to manufacture reproducible samples has hampered our attempt to determine the dose dependence of strain and magnetic profiles. Serious inconsistencies in the properties of implanted garnets versus dose have been reported by at least two other laboratories.[55,56]

C. Lateral Strain and Stress

An important characteristic of ion-implanted single crystal layers is the compressive stress in the implanted region. Its existence implies that at least up to a certain dose, implantation causes a tendency toward an isotropic or nearly isotropic expansion of the unit cell. But at least initially the registry with undamaged crystal constrains the implanted layer to expand only in a direction perpendicular to the surface.[7] Therefore the implanted layer and the much thicker substrate are in lateral compression and lateral tension, respectively. The

depth-averaged compressive stress has been measured by a beam cantilever method.[14] For 100 keV Ne^+ implantation with increasing doses ranging from $10^{13}/cm^2$ to $10^{15}/cm^2$, in Ref. (14) the average stress initially increases linearly with dose, then saturates, and finally decreases to the limit of detection. Over this range we find that the perpendicular strain continues to increase with dose up to amorphousness. Three possible reasons for the decrease of stress come to mind: (1) with increasing dose the modulus of elasticity E of the implanted layer diminishes by more than an order of magnitude; (2) dislocations are formed to accommodate the lattice mismatch and allow the unit cell to relax back to a cubic shape; and (3) a phase transition occurs such that the new equilibrium shape of the unit cell is rhombohedral.

By measuring lateral strain we have attempted to determine the role played by the second possibility in the mechanism of stress relaxation. For the Cu K_α (880) $\gamma_0 > |\gamma_H|$ reflection in <111> garnet the glancing angles of incidence and diffraction are 80^0 and 9.5^0, respectively. In the $\gamma_0 < |\gamma_H|$ reflection the directions of incidence and diffraction are reversed. For both cases the rocking curve measures lateral in addition to perpendicular strain. In the $\gamma_0 < |\gamma_H|$ reflection the sensitivity to lateral strain is even greater than to perpendicular strain. In a helium implanted sample with a maximum perpendicular strain of 0.82%, previous measurement showed[7] that lateral strain was below the limit of detection ($\sim$0.03%).

In the present study we selected the neon distribution #4 ($\Delta\varepsilon^{\perp}_{max}$=1.57%) and the helium distribution #3 ($\Delta\varepsilon^{\perp}_{max}$ = 2.00%) because the strain is high but the damage is below the level of amorphousness (see the next section for results on damage). The nominal dose for neon case #4 is greater than the dose for which the stress rapidly diminishes, as reported in Ref (14). Our present result is that for both Ne^+ and He^+ distributions the measured lateral strain at any depth is not greater than 0.03%. Thus, even though the stress may have relaxed, the implanted unit cell has not returned to cubic shape. This rules out possibility #2 as the mechanism of stress relaxation. We do not believe that the modulus of

elasticity goes to zero as the implanted layer approaches amorphousness. Crystalline and amorphous materials of the same composition usually have similar elastic properties. We are thus left with the hypothesis that the equilibrium shape of the unit cell in the implanted garnet layer becomes, at a certain dose, rhombohedral. A possible mechanism for this transition has been suggested by W.L. Johnson.[57] Due to the interaction of the local stress field of a Frenkel pair with the macroscopic (average) stress, the energy of the Frenkel pair is not invariant under rotation. During implantation at a certain dose this energy is minimized by an uniaxial orientation of Frenkel pairs which reduces the macroscopic stress. When this occurs the perpendicular strain no longer has a Poisson contribution. For this and higher doses $\Delta\varepsilon^{\perp}$ should show a different behavior from that at lower doses. We are unable to verify this since the actual doses are uncertain and for nominally identical implantation the strain distribution is not reproducible.

The assumption that in implanted <111> garnet the equilibrium unit cell becomes rhombohedral is supported by a measurement of the stress distribution[16] in a magnetic garnet implanted with 200 keV Ne^{+} at a dose of $2\times10^{14}/cm^{2}$. According to this reference, in the implanted layer the stress distribution is bimodal. The 1000 Å thick regions near the surface and near the interface with unimplanted material are under substantial and comparable lateral stress. In the intermediate region, also 1000 Å thick, where the perpendicular strain and the damage are greatest, the stress is barely measurable. The existence of compressive stress in the outer region is unexplained if relaxation occurs by a crystallographic decoupling of highly implanted from less implanted region. But if the relaxation is accomplished by a local transition to an equilibrium rhombohedral unit cell, then at a given depth the stress depends on the degree of this transition. In this case two regions with the same sign of the stress may be separated by a region with zero stress. Since even at high doses we have measured the lateral strain to be zero, henceforth we shall drop the term "perpendicular" when we speak of strain.

D. Damage Profiles

For the present range of doses, for each species the area under the rocking curve changes by roughly one order of magnitude. Since the layer thickness does not decrease with increasing dose, the only possible interpretation is that the magnitude of the structure factor F decreases. Amorphousness corresponds to $|F| \sim 0$. Small strains (0.1 to 0.5%) are easily measured with good accuracy. In this region the structure factor is essentially unchanged and no information can be obtained about the damage profile. When the maximum strain reaches about 2.5% for neon, 3.4% for helium or 3.9% for hydrogen, the structure factor in the region of maximum strain has decreased to nearly zero and above this strain no measurable diffraction occurs. As the peak strain falls below this critical value, the local structure factor rises sharply, the best fit being a negative exponential in $(\Delta\varepsilon)^2$. Since the structure factor is known to depend in this same way on U (the standard deviation of the assumed gaussian random atomic displacements) it follows that the peak value of U is linear in $\Delta\varepsilon$. Elsewhere in the profile, the sensitivity is such that U cannot be determined with equal precision and we can only state that when the strain is high enough to give a determination of U, the peak value occurs in the region of maximum strain. Since it varies linearly in this region, it is a reasonable hypothesis that this relation holds at all depths and strains, in agreement with Ref. (7). This is consistent with the idea that the damage is the source of the strain.

With this assumption, excellent fits have been obtained for all doses. The proportionality constant between U and $\Delta\varepsilon$ has the value 0.25, 0.18 and 0.13 Å/% for Ne^+, He^+ and H_2^+ implantation, respectively. The different effective levels of damage for the same strain are due to the discriminating sensitivity of the (444), (888) and (880) reflections to the c-sites occupied by the heavy elements Y, Gd, and Tm. The implication is that for the same strain, neon ions damage the c-sublattice more severely than helium or hydrogen ions. This is in agreement

with the ballistics of implantation in polyatomic materials.[49]

At high doses the broadening of (880) reflections indicates the presence of lateral nonuniformities attributable to extended defects. The resolution is not sufficient to provide quantitative information about their density or structure. As we have shown, these defects do not result in any measurable lateral strain.

E. Magnetic Properties versus Strain for He^+ and Ne^+ implantation

The local field for uniform resonance H_{un} in $\perp$ FMR is

$$H_{un} = \frac{\omega}{\gamma} - H_k + 4\pi M + \frac{2}{3} H_1 \qquad (2)$$

where ω is the microwave angular frequency, γ is the gyromagnetic ratio, H_k is the uniaxial anisotropy field, $4\pi M$ is the saturation magnetization, and H_1 is the cubic anisotropy field. The change in H_{un} is specified by ΔH_{un}, the difference between its value and that in the bulk region. Of all magnetic properties obtainable by FMR, the distribution of ΔH_{un} is determined with the highest precision. However for high doses, substantial changes in other parameters are demanded by the resonance spectrum. Even though these changes are not known with the same precision, their general features are incontestable. A good example is shown in Fig. 5 for the helium implantation with dose $1.2 \times 10^{16}/cm^2$. This dose is not sufficient to give a nonmagnetic layer but produces extreme variations in almost all magnetic parameters and gives a very rich spectrum in $\perp$ FMR with eleven surface modes as shown in Figs. 2b and 3b. Fig. 5a shows the profile of ΔH_{un} (solid line) and the strain profile multiplied by 4.1 kOe/% (dashed line). This choice of multiplicative constant is made clear below. Although the strain profile is unimodal, the distribution of ΔH_{un} is bimodal and no longer resembles the strain profile. The profiles of $4\pi M$ and A/M are shown in Figs. 5b and 5c. At the location of maximum strain there is an 80% reduction in $4\pi M$ and a 98%

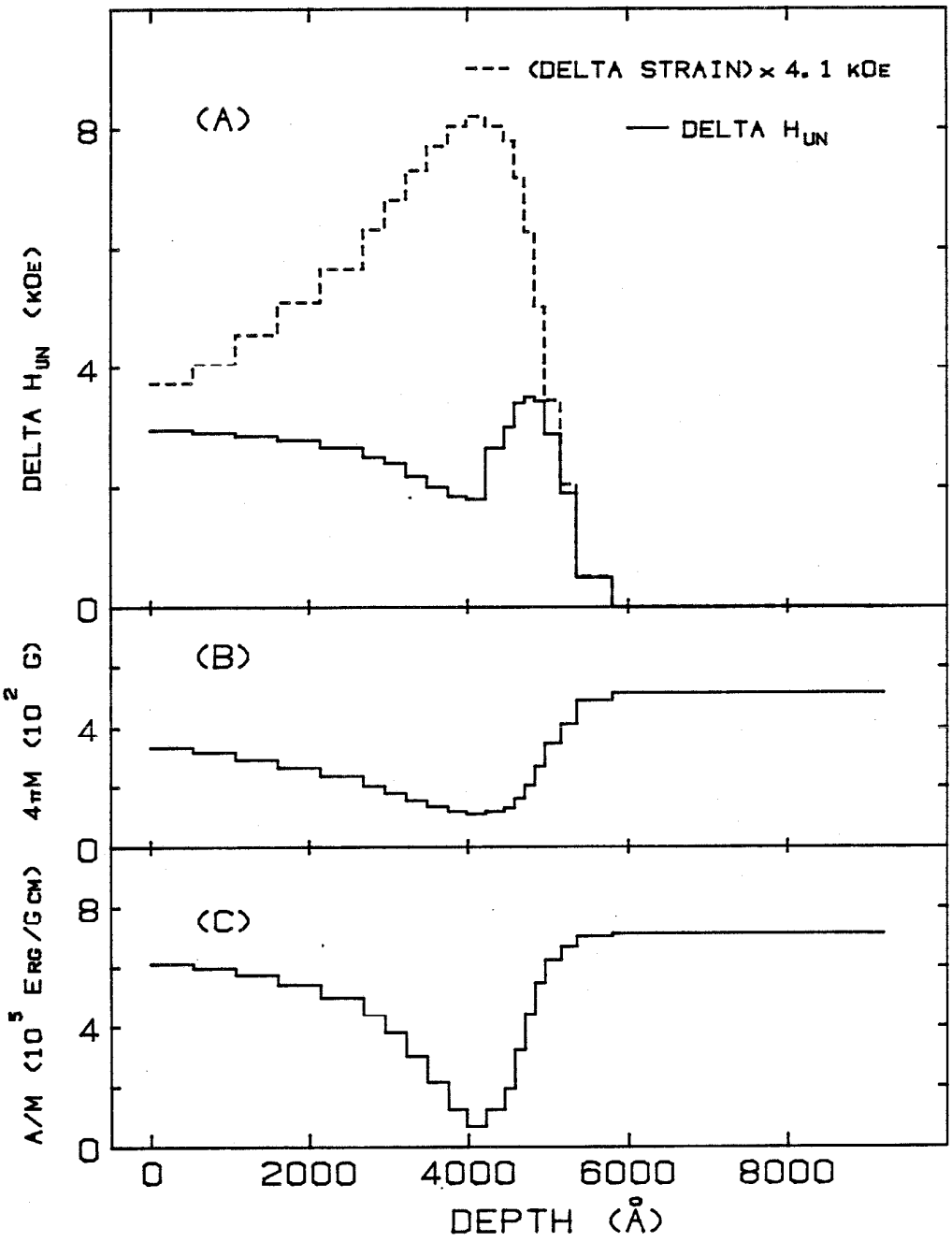

Figure 5 Profiles corresponding to Figure 3: (a) ΔH_{un} (solid) and $\Delta\varepsilon$ (dashed); (b) magnetization $4\pi M$ (c) Ratio A/M.

reduction in exchange constant, A. These extreme variations are required to produce the FMR spectra of Fig. 3b.

The relationship between ΔH_{un} and $\Delta\varepsilon$ may be obtained by considering their respective values for all doses and depths. Figure 6a shows the values of ΔH_{un} versus $\Delta\varepsilon$ obtained for all doses of helium implantation. A different symbol is used to represent each set of points corresponding to a particular dose. The nominal doses and the values of $\Delta\varepsilon_{max}$ are also shown. If we limit attention to the two lower doses for which $\Delta\varepsilon_{max} < 1.3\%$, all points lie on a single curve. In this dose range the relationship between ΔH_{un} and $\Delta\varepsilon$ is unique and independent of dose or depth. As mentioned in a previous section, for pairs of samples with nominally the same implantation, the values of $\Delta\varepsilon_{max}$ are nearly the same, but strain values towards the surface differ by a factor as large as 2.5. Even with such differences in profile the relationship shown in Fig. 6a is valid.

The initial slope of the curve is 4.1 kOe/%. As we shall show, in the linear region approximately 98% of ΔH_{un} is due to the change in uniaxial anisotropy H_k. If the change in H_k is attributed to magnetostriction using bulk values of Young's modulus ($E = 2.0\times10^{12}$ dynes/cm^2), Poisson's ratio ($\nu = 0.29$) and magnetization ($4\pi M = 510$G), one obtains a value of -3.6×10^{-6} for the magnetostriction constant λ_{111}. This number is higher than but in reasonable agreement with the value -3.4×10^{-6} estimated from the nominal composition and the tables given in Ref. (40). Thus we conclude that, at least for He^+, at low doses the principal source of ΔH_k is $\Delta\varepsilon$ and that the relationship is the same as for external elastic deformation (magnetostriction).

For $\Delta\varepsilon_{max} \gtrsim 1.3\%$ the dependence of ΔH_{un} on $\Delta\varepsilon$ is much more complicated. First, ΔH_{un} saturates at a value 3.6 kOe at strain $\Delta\varepsilon = 1.5\%$ and then decreases to a value near zero at $\Delta\varepsilon \approx 2.3\%$ where the material becomes paramagnetic. The material remains nonferrimagnetic up to the highest observed strain $\Delta\varepsilon = 3.30\%$ where the material is nearly amorphous. Second, in the region where ΔH_{un} is

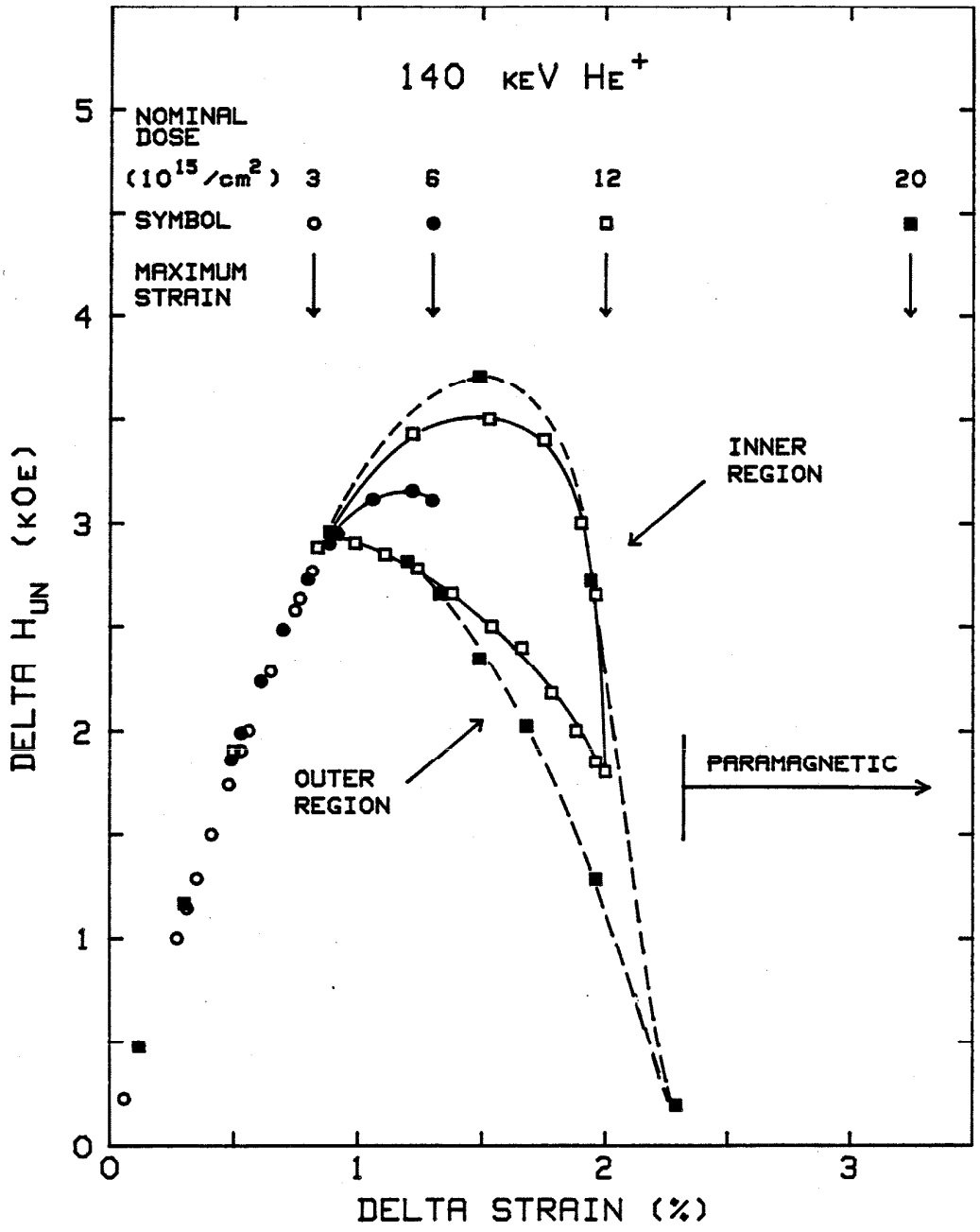

Figure 6(a). ΔH_{un} versus $\Delta\varepsilon$ for four He^+ doses. Each set of points corresponding to one dose is represented by its own symbol. Nominal doses and $\Delta\varepsilon_{max}$ values are also indicated.

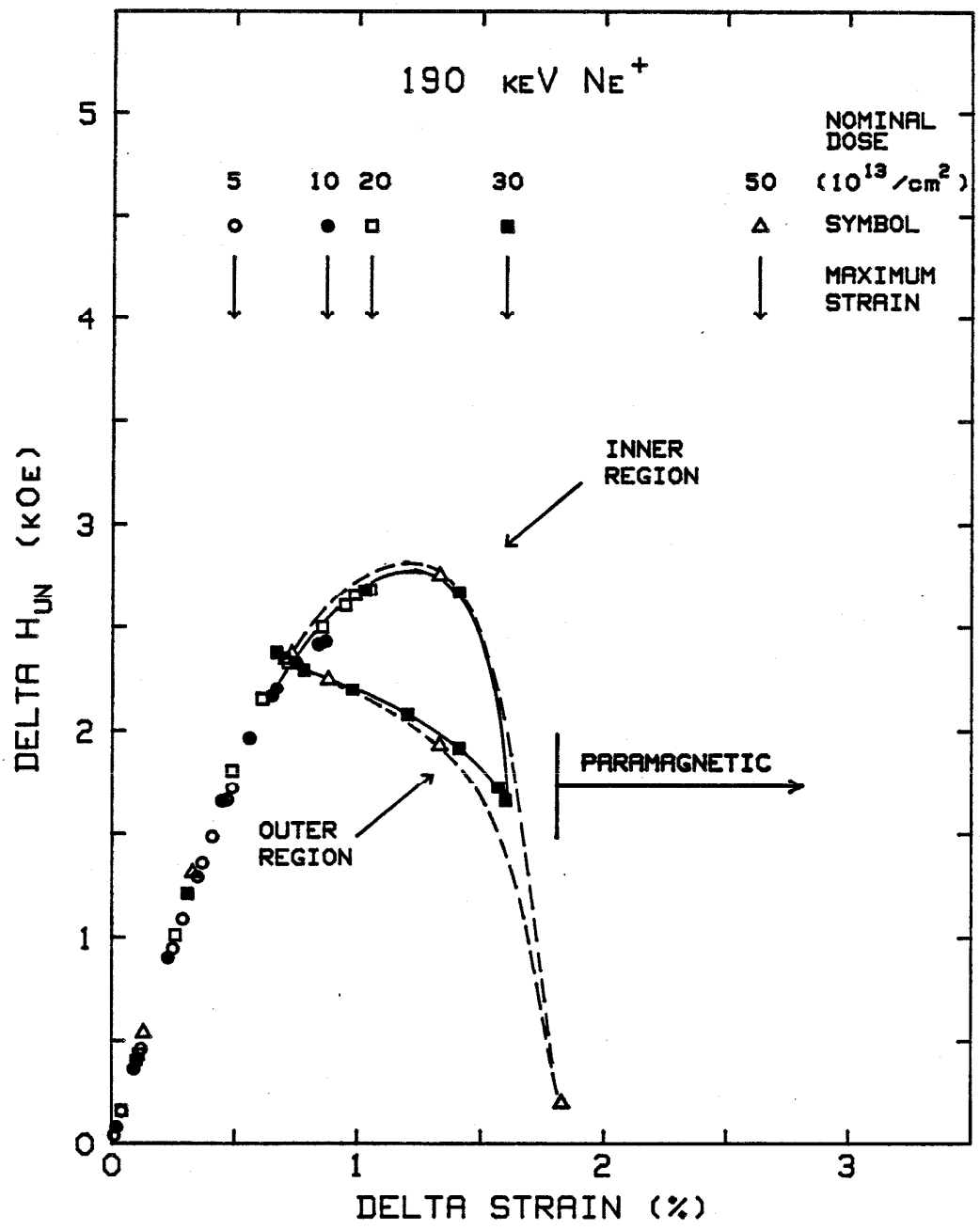

Figure 6(b). ΔH_{un} versus $\Delta\varepsilon$ for five Ne^+ doses.

saturating and decreasing with strain, the relationship is no longer unique. The solid and dashed lines, respectively, connect the points obtained for two different doses where $\Delta\varepsilon_{max}$ is equal to 2.00% and 3.30%. In each case there are two relations between ΔH_{un} and $\Delta\varepsilon$. If the implanted layer is subdivided into two regions, one (the outer) includes all points from the surface up to the location of the peak strain, and the other (inner) region includes points from the peak strain down to the interface with unimplanted material. These regions have a different relation between ΔH_{un} and $\Delta\varepsilon$. Another intriguing feature is the lower saturation for $\Delta\varepsilon_{max} < 1.5\%$ compared to the peak value for higher strains. For now we defer discussion of the possible reasons for this behavior.

A plot of ΔH_{un} vs. $\Delta\varepsilon$ for all neon doses is shown in Fig. 6b. The general features seen with neon are the same as with helium. The initial slope of the curve is 4.1 kOe/%, again supporting the conclusion that at low doses the phenomenon giving rise to ΔH_k is magnetostriction. The important differences between Ne^+ and He^+ implantation are the lower peak value of ΔH_{un} (2.8 kOe versus 3.6 kOe) and the lower strain (1.8% versus 2.3%) for which the material becomes paramagnetic.

We return to He^+ implantation for a discussion of magnetic properties other than H_{un}. Figure 7 shows the values of $4\pi M$, A/M, H_1, and α versus maximum $\Delta\varepsilon$. Due to poorer sensitivity, the profile shapes of $4\pi M$, A/M, H_1 and α cannot be independently determined. In the dose range below saturation of ΔH_{un}, a good fit is obtained if the implantation-induced changes are assumed proportional to $\Delta\varepsilon$. The extreme variation then occurs at the point where the strain is a maximum. For higher doses the variations are less certain, particularly when a part of the surface layer becomes paramagnetic. A good fit is still obtained if the changes are proportional to $\Delta\varepsilon$, except that $4\pi M$ and A/M go to zero at $\Delta\varepsilon \simeq 2.3\%$ and remain zero for higher strain.

The variation of H_1 is less certain but it clearly decreases as the strain increases. The bulk value, -165±5 Oe, was determined with good accuracy by

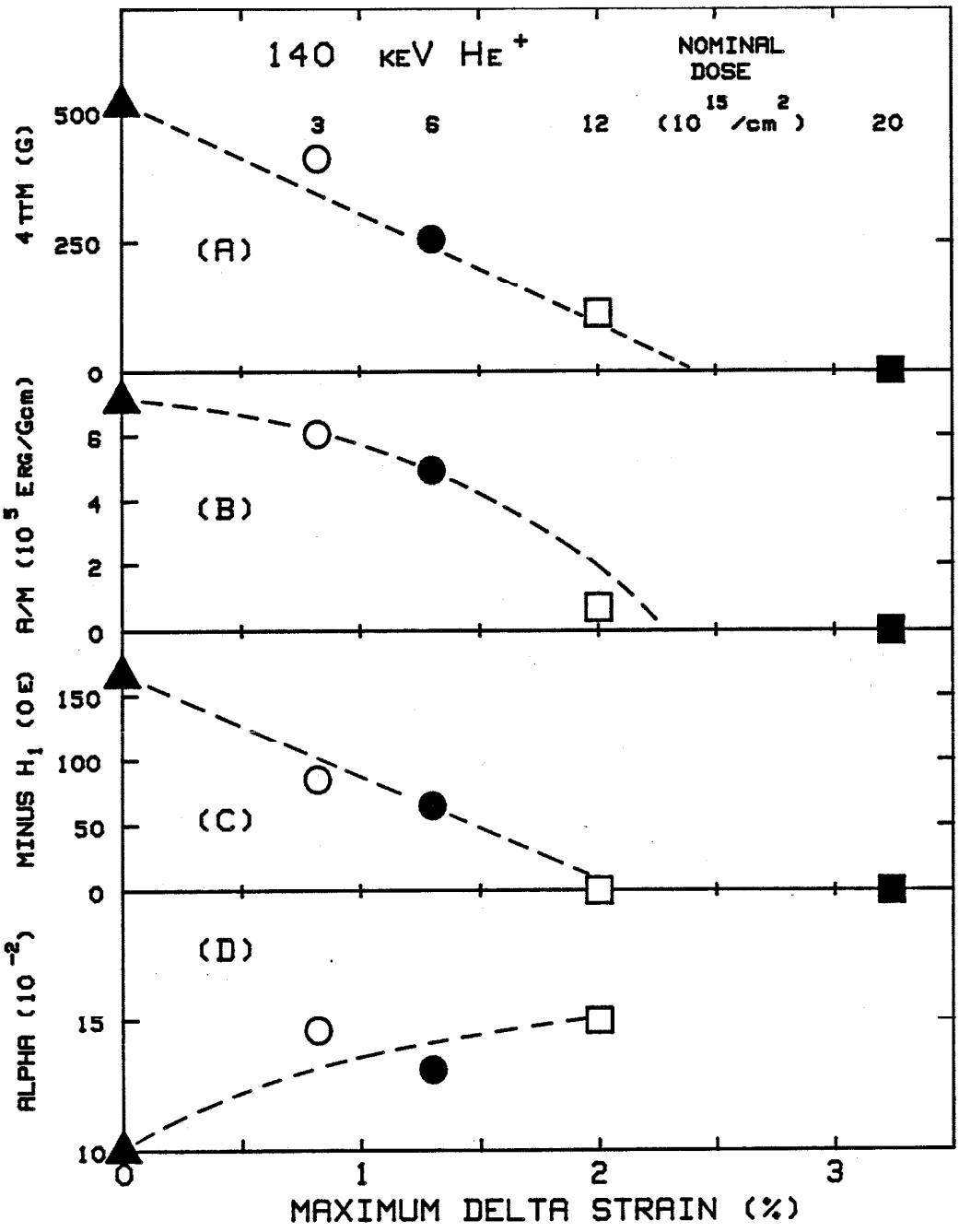

Figure 7(a)-(d). Extremum values of magnetic properties versus $\Delta\varepsilon_{max}$ for the four He^+ doses. Values obtained for each dose are represented by their own symbol. (a) Saturation magnetization $4\pi M$. (b) Ratio (A/M) of exchange stiffness constant to saturation magnetization. (c) Cubic anisotropy field - H_1. (d) Damping coefficient α (note zero suppression).

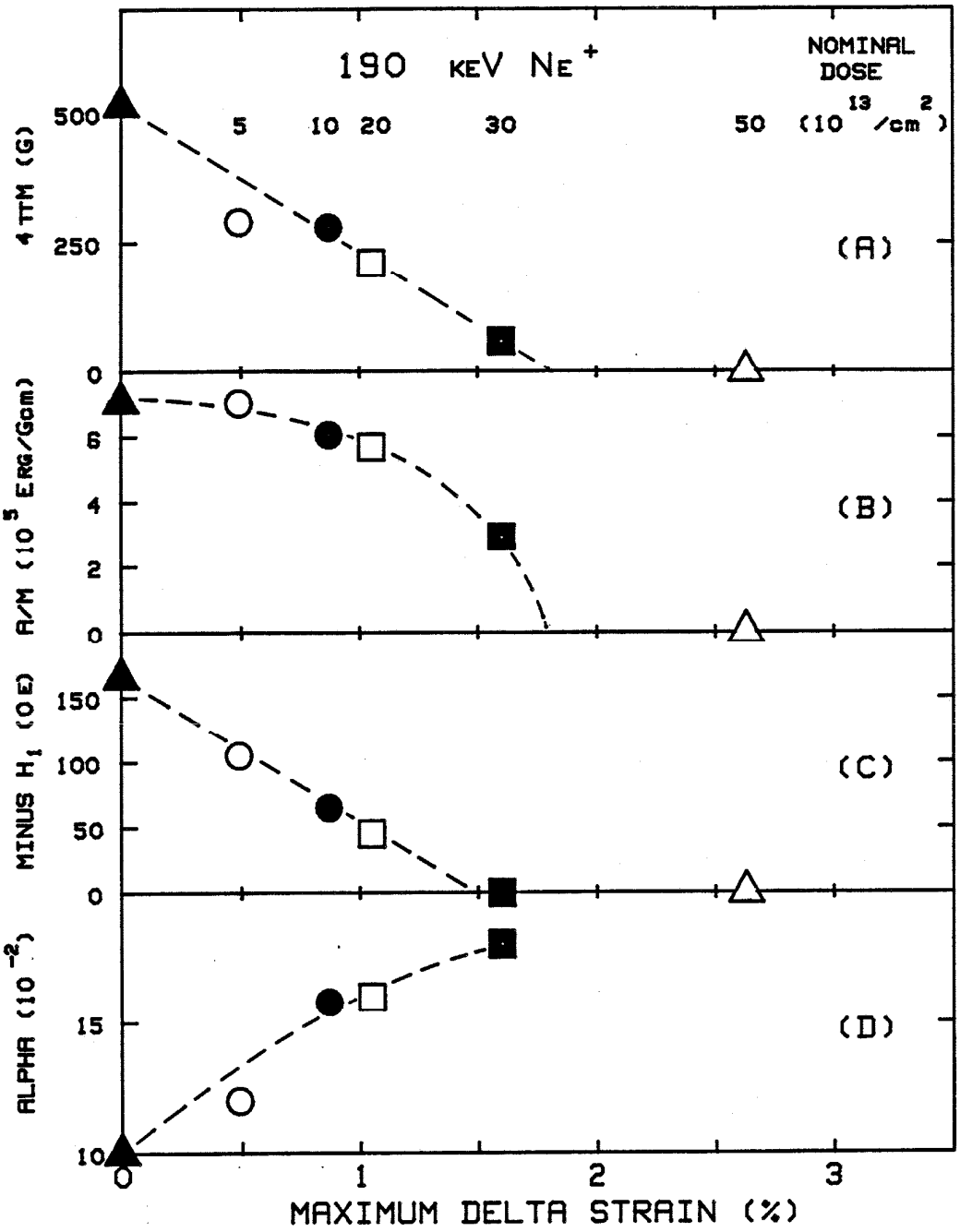

Figure 8(a)-(d). Extremum values of magnetic properties versus $\Delta\varepsilon_{max}$ for the five Ne^{+} doses.

measuring the bulk resonance mode as a function of angle. This procedure when applied to the surface modes can only be used to estimate the minimum value of H_1 since the large uniaxial anisotropy masks the effect of H_1 and since accurate analysis is not feasible for spin-wave resonance at angles other than parallel and perpendicular. The asymmetry of the resonance field for the principal surface mode vs. angle suggests that H_1 decreases about 70% for the dose where $\Delta\varepsilon$ = 1.3%. Comparison of perpendicular and parallel spectra requires a change nearly twice as large or else requires a small increase ($\sim$ 4%) in the surface value of γ (perpendicular and parallel FMR cannot distinguish between these parameters). The bulk value of γ is 1.503×10^7 $(\text{Oe sec})^{-1}$. This is 15% lower than that of pure YIG, a feature attributed to the presence of rare earth ions. It is quite plausible that implantation damage would reduce this effect. The damping coefficient α is another parameter which increases with strain. At $\Delta\varepsilon \simeq 2.3\%$, where most magnetic parameters go to zero, α reaches a value 50% larger than in the bulk. For $\Delta\varepsilon > 2.3\%$ the material is paramagnetic and α is not defined.

As shown in Figure 8, the magnetic properties of the Ne^+ implanted samples behave in a way that is similar to He^+ implantion. The major differences are the higher rate of decrease with strain and consequently the lower value of $\Delta\varepsilon$ for which $4\pi M$, A/M, and H_1 go to zero (1.8% versus 2.3%), and the large increase of α with $\Delta\varepsilon$. As for helium implantation, the transition to paramagnetism is accompanied by a rapid drop in ΔH_{un} (Fig. 6(b)).

F. Discussion of magnetic properties for Ne^+ and He^+ implantation

We have seen that for both Ne^+ and He^+ implantation the parameters M and A which define garnet as ferrimagnetic decrease with increasing strain (and damage) and that for a certain strain they go to zero. The local transition to paramagnetism occurs for damage levels roughly 30% below that required for amorphousness. The information obtained so far is, of course, still insufficient to

permit an identification of the source of the changes in magnetic properties. One is tempted to attribute the destruction of ferrimagnetism to incoherent atomic displacements. There is even a correspondence between the more rapid decrease in $4\pi M$ and A/M with strain on one hand and on the other hand the larger increase of damage with strain for neon vs. helium implantation. However amorphous ferromagnetic materials do exist. It is conceivable that the large albeit coherent strains caused by implantation also contribute to the transition to paramagnetism. We can say very little about the increase in the damping parameter α with strain and damage. The increase implies larger losses from magnetic excitations to lattice vibration. In unimplanted doped YIG the losses are attributed to the presence of rare earth ions.[40] Their role in implanted doped YIG is poorly understood, since in Ref. (5) a large (400 Oe) virgin linewidth decreases while in the present case a low (70 Oe) virgin linewidth increases with damage.

Figs. 6, 7 and 8 show that $-\Delta H_k$ is the dominant component of ΔH_{un}. The first important feature of the relation between ΔH_k and $\Delta\varepsilon$ is the initial linearity and value of the slope which matches the estimated magnetostrictive effect. The component of bulk H_k attributable to growth-induced anisotropy is about 500 Oe whereas ΔH_k can be as large as 3000 Oe. There is therefore no evidence that at low doses the change in H_k is due to the suppression of growth-induced anisotropy.[44]

The second important feature is the saturation and decrease in ΔH_k with increasing $\Delta\varepsilon$. This is similar to the reported saturation and decrease in stress in another garnet.[14,16] A detailed correlation of these separate experiments is not possible, but the source of the decrease in both cases might well be the same and is likely to be the damage. The ratio of ΔH_k to stress could in principle be used to define a parameter $3\lambda_{111}/M$, but it is unlikely that this would be the same parameter obtained by application of external stress and deformation to this same implanted material.

We do not have an explanation for the departure from a unique relation between ΔH_{un} and $\Delta\varepsilon$ at high doses, but the sensitivity of the fitting procedure and the accuracy of the spectrum give us confidence that the difference is real.

It has been observed in Figs. 2a and 2b that from medium to high doses the separation in resonance field between principal surface and body mode is relatively insensitive to maximum strain and dose. This is a natural consequence of the saturation and decrease in ΔH_k with increasing strain. In $\perp$ FMR the principal surface mode is localized in the region neighboring the maximum H_{un}. At increasing doses this maximum does not change, but shifts location from the point of maximum strain towards the interface with unimplanted material, even after large portions of the implanted layer have become paramagnetic. This also indicates that the shift of this mode with external elastic deformation cannot be used to measure λ_{111}/M in the saturation region.

G. Magnetic Profiles for H_2^+ Implantation

The effects of H^+ implantation on ΔH_{un} are known to be markedly different from those of other ions. In a given material, for He^+, B^+, C^+, O^+, and Ne^+ implantation the separation $\Delta H_\perp$ between principal surface and body modes in $\perp$ FMR saturates with increasing dose at a value not exceeding 3 kOe.[45] In the same material, implantation with hydrogen causes $\Delta H_\perp$ to increase with dose beyond measurement capability at 10 GHz ($\Delta H_\perp \approx 10$ kOe). Conversely, for hydrogen implantation $\Delta H_\perp$ decreases rapidly with annealing temperature around 350°C, while $\Delta H_\perp$ for other ions changes relatively little.[45] The rapid decrease in $\Delta H_\perp$ correlates with annealing-induced desorption of hydrogen.[8] Upon annealing up to 700°C $\Delta H_\perp$ shows a nonlinear dependence on the strain.[33] Comparison of strain, magnetostriction constant and $\Delta H_\perp$ for deuterium implantation shows an excess contribution to ΔH_k which is not attributable to simple magnetostriction.[56]

Even in garnets with very low λ_{111} large values of $\Delta H_{\perp}$ are observed.[47] These results strongly suggest chemical effects associated with the presence of implanted hydrogen. Our results support this view.

Figure 9(a) shows the distribution of ΔH_{un} as a function of depth obtained for 120 keV, $5 \times 10^{15}/cm^2$ H_2^+. This distribution corresponds to the third FMR spectrum of Figure 2(c). The maximum ΔH_{un} is 4.5 kOe, a value greater than any obtained with Ne^+ or He^+ implantation. If the total ΔH_{un} profile is assumed to consist of a magnetostrictive contribution due to strain and a contribution due to a different mechanism, then a comparison with the strain profile may yield information about the unknown mechanism. Figure 9(b) shows the strain distribution multiplied by 4.1 kOe/%. Since the maximum $\Delta\varepsilon$ for this case is only 0.60%, it is reasonable to assume that the initial linear relation between ΔH_{un} and $\Delta\varepsilon$ found for Ne^+ and He^+ is also valid here. Figure 9(c) shows the difference between total and magnetostrictive ΔH_{un}. The excess ΔH_{un} is in remarkable agreement with the calculated LSS range (the local density of hydrogen atoms). This agreement strongly suggests a connection between ΔH_{un} and the presence of hydrogen. The connection is further confirmed by comparing the profiles of ΔH_{un} and $\Delta\varepsilon$ before and after annealing at successively higher temperatures. Figures 10(a) and (b) show such a sequence for nominal doses $5 \times 10^{15}/cm^2$ and $2 \times 10^{15}/cm^2$, respectively. Before annealing the ratio of maximum ΔH_{un} to maximum $\Delta\varepsilon$ is greater for the sample with higher dose, indicating that the excess ΔH_{un} increases more rapidly with dose than does $\Delta\varepsilon$. With annealing up to 300°C the excess ΔH_{un} decreases and shifts toward the location of maximum strain and damage. Gettering of implanted dopants from regions with low damage to regions with higher damage has been reported for other materials.[58] The diminishing amount of excess ΔH_{un} is consistent with the desorption of hydrogen at these temperatures. After annealing at 400°C, little or no hydrogen remains in the crystal[8] and the total ΔH_{un} coincides with the contribution due to strain. Annealing at 500°C and 600°C

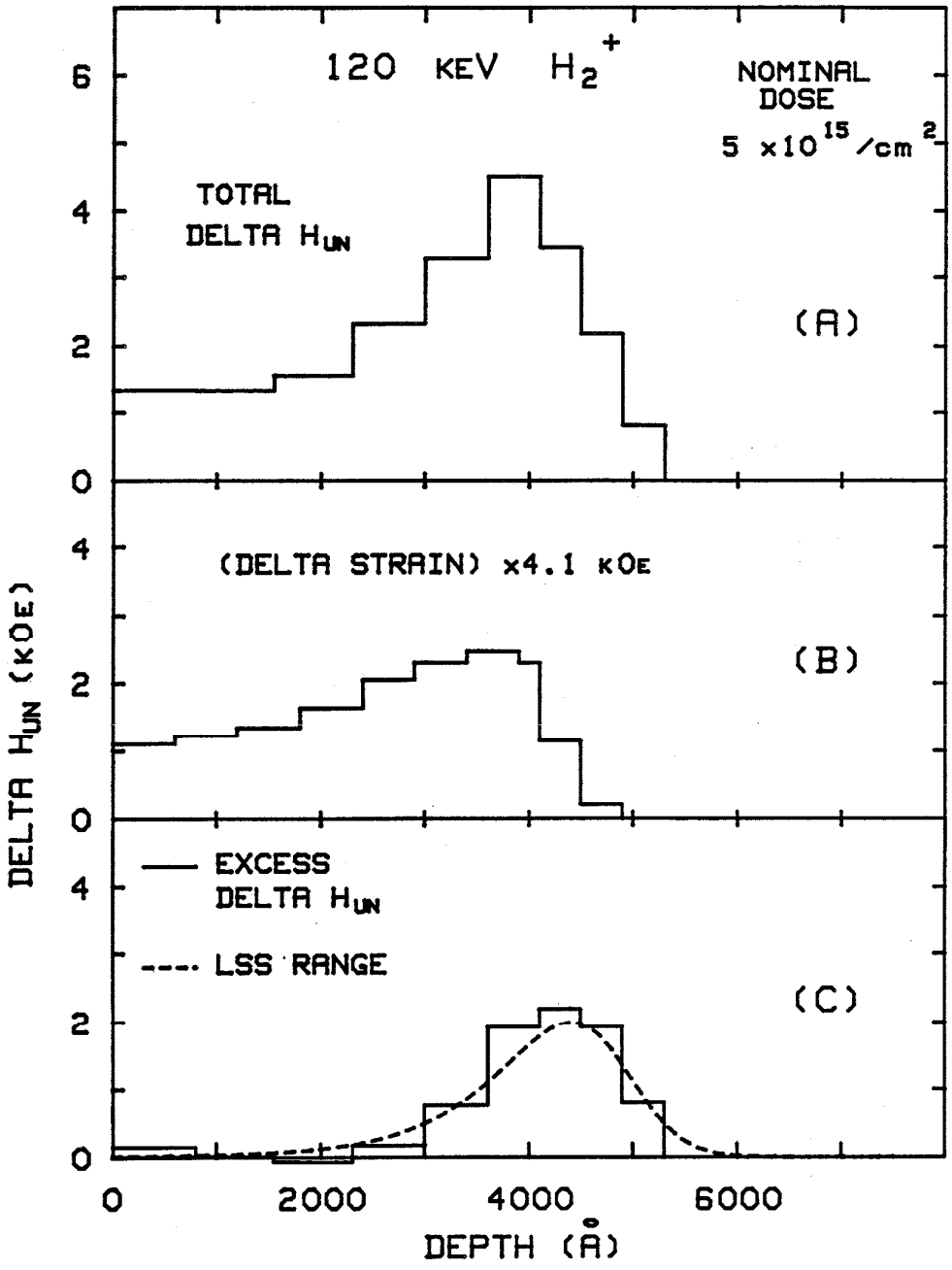

Figure 9. Depth profiles of ΔH_{un} for 120 keV, $5 \times 10^{15}/cm^2$ H_2^+ implantation. (a) FMR-determined ΔH_{un} distribution. (b) $\Delta\varepsilon$ profile multiplied by 4.1 kOe. (c) Difference between profiles (a) and (b). Also shown (dashed) is calculated LSS range of 60 keV H^+ in garnet.

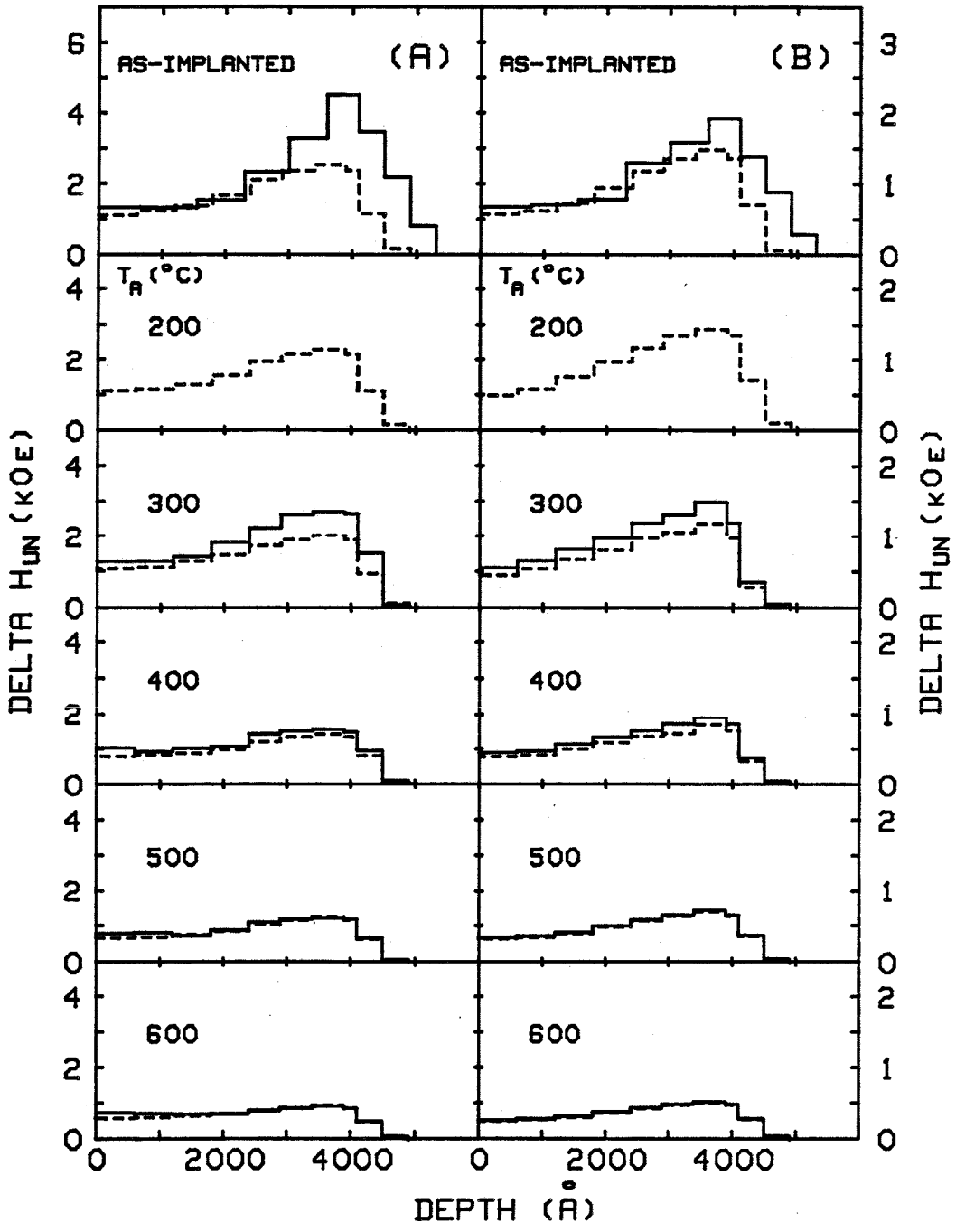

Figure 10. (a) and (b), respectively, show total ΔH_{un} profiles (solid) and $\Delta\varepsilon$x4.1 kOe profiles (dashed) for $5\text{x}10^{15}/\text{cm}^2$ and $2\text{x}10^{15}/\text{cm}^2$ 120 keV H_2^+ implantation. Profiles are for successively higher annealing temperature. Note the different vertical scales.

decreases ΔH_{un} and $\Delta\varepsilon$ but maintains the magnetostrictive relation.

In addition to the unusual effect on ΔH_{un} which is primarily a change in uniaxial anisotropy, hydrogen implantation also causes unusual changes in $4\pi M$, A/M and α. For the case shown in Figure 9, where the maximum $\Delta\varepsilon$ is only 0.60%, there is a 60% reduction in $4\pi M$. If the same maximum strain is obtained with Ne^+ or He^+, the reduction is less than 30%. For hydrogen implantation the region with significantly lowered $4\pi M$ extends beyond the strained layer up to the depth of excess ΔH_{un}. However at strain $\Delta\varepsilon$ = 0.60% the exchange constant A is nearly the same for all three species: 64%, 68% and 56% of bulk value for neon, helium and hydrogen, respectively. Since for hydrogen A decreases more slowly than M, for the distribution of Figure 9 the average A/M is 43% greater than bulk value. This is accompanied by an increase of a factor of two in α.

As in the case of Ne^+ and He^+, we have limited understanding of what causes the changes in magnetic properties for hydrogen implantation. The reduction in magnetization accompanied by a smaller reduction in A suggests that incoherent atomic displacements play a smaller role than for Ne^+ and He^+, and the profiles support the view that the presence of hydrogen atoms is a significant factor. The same appears to be true of H_k, but the uniaxial character is intriguing.

It would be informative to do detailed X-ray and FMR analyses of deuterium implanted garnet. Since for deuterium nuclear stopping is greater than for hydrogen, the relative contribution of the strain compared to the contribution attributable to chemistry would be greater. Published results already show that for deuterium ΔH_{un} is greater than expected from simple magnetostriction.[56]

The discovery of large chemical effects for hydrogen implies that other ions may also produce effects not associated with strain or damage. But if detectable chemical effects require dopant concentrations of at least 1%, such measurements are difficult. For all other ions the implanted garnet is rendered paramagnetic with doses yielding concentrations well below 1%.

H. Results of Annealing

In this paper the study of annealing behavior was limited to the two lower doses of Ne^+ and He^+ implantation and to the three lower doses of H_2^+ implantation. For Ne^+ and He^+ at these doses the relationships between ΔH_{un} and $\Delta\varepsilon$ are independent of depth and consequently FMR spectra are easily interpreted. The maximum strain and ΔH_{un} for the lowest dose hydrogen implantation were too low after annealing to provide significant quantitative information. The reasons for excluding the high-dose hydrogen implantations were discussed earlier.

For all three species the strain decreases with increasing annealing temperature. However the changes in profile shape are negligible. For each species it is thus possible to normalize the profiles to the profile obtained prior to annealing. Figure 11 shows the results. It is worth noting that before annealing and normalizing the maximum values of $\Delta\varepsilon$ were 0.49% and 0.87% for Ne^+; 0.82% and 1.30% for He^+; and 0.35% and 0.60% for H_2^+. For Ne^+ and H_2^+ the annealing behavior is nearly independent of the magnitude of the original strain. For He^+ implantation at $6\times10^{15}/cm^2$ annealing at $\sim400^oC$ results in severe broadening of both X-ray and FMR spectra. At this and higher doses there is a formation of He bubbles[24,5] which results in a deterioration of crystalline and magnetic properties. The present measurements on the lower doses of He^+ implantation did not show any broadening up to 600^oC.

Although the strain for hydrogen decreases more rapidly with annealing temperature than the strain for neon and helium, the general trend is the same for all three species. This reinforces the idea that despite the large differences in dose, the major source of the strain is independent of ion species. The more rapid decrease of strain for temperatures between 300^oC and 400^oC and again between 500^oC and 600^oC has been previously reported for Ne^+ implantation.[12] The present measurements and all other measurements known to us do not provide infor-

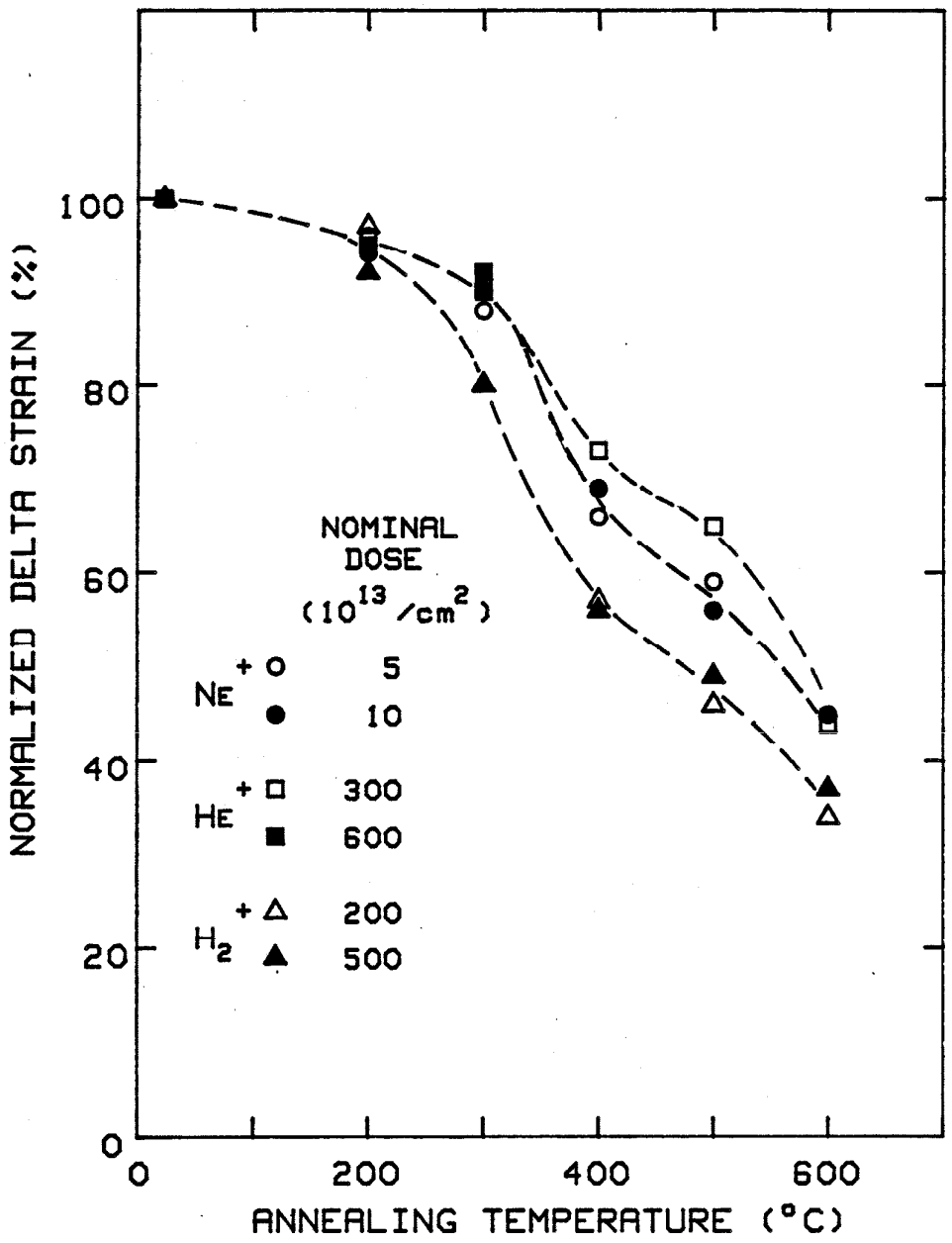

Figure 11. Normalized strain $\Delta\varepsilon$ versus annealing temperature for neon, helium and hydrogen implantation.

mation permitting speculation concerning the reasons for this behavior. For all six cases and especially after annealing the damage is too low for meaningful measurement.

The behavior of magnetic properties for Ne^+ and He^+ implantation is reasonably consistent with the strain. As the strain decreases, the profiles of ΔH_{un} follow the curves of Figures 6(a) and (b). Slight inconsistencies are observed for $4\pi M$ and A/M. The magnetization increases with annealing, reaching its bulk value at 600^oC, where the strain has relaxed only half way. For both species the ratio of A/M also increases with annealing but at 600^oC remains some 20% below bulk value. The damping parameter α decreases with annealing, reaching the bulk value around 400^oC, and for higher temperature it drops 10% below this value. The cubic anisotropy remains 20% to 50% low after annealing up to 400^oC. We have already shown the annealing behavior of ΔH_{un} for hydrogen implantation. In this case the values of $4\pi M$, A/M and α also move toward and reach the respective bulk values at 600^oC.

VI. Concluding Remarks

It has been shown that a considerable amount of information can be obtained by combining detailed analyses of X-ray and FMR spectra of ion-implanted garnet. Several conclusions afforded by detailed analysis are substantially different from conclusions based only on considerations of $\Delta H_\perp$, the separation of principal surface mode and bulk mode in FMR and on the maximum extent $\Delta\theta$ of the rocking curve in X-ray diffraction. Some of the results clarify various aspects of implanted garnet; other results raise new and difficult questions. The major feature to be explained is the departure at high doses from a unique relationship between ΔH_{un} and $\Delta\varepsilon$. Also, a study of the annealing behavior of samples implanted at high dose would be worthwhile.

An important question is whether or not the present results are specific to

the garnet and the implanted species used. This cannot be clearly answered due to the lack of a theory of the properties of implanted garnet. Nevertheless it is probable that the general features of the present results are reproduced in all magnetic garnets implanted with a variety of ion species. Judging by published X-ray rocking curves, the strain depends on ion species, energy, dose and annealing but is insensitive to the composition of the garnet. Regardless of implanted species, all garnets are probably rendered amorphous at strains around 3%. Complete and detailed FMR spectra of implanted garnet have been rarely published, but the more frequently published dependence of $\Delta H_{\perp}$ on ion species, dose, etc., is similar to our observations. We infer that the entire structures of these spectra are also similar to the present measurements. Thus we expect that magnetic profiles of garnets with different compositions and implanted with different ions are similar to those of the films we have studied.

Acknowledgements

One of the authors (VSS) thanks the International Business Machines Corporation for financial support in the form of a predoctoral fellowship. We thank Tim Gallagher, Kochan Ju, H. Ben Hu and Chris Bajorek of the San Jose laboratory of IBM for supplying the samples and encouraging this study. We express appreciation to Lavada Moudy, Howard Glass and Jack Mee of Rockwell International (Anaheim, CA) for providing easy access to a double-crystal diffractometer. We thank Jim Campbell of Caltech for suggesting the use of and providing us with the HP 9826 computer. Thad Vreeland of Caltech encouraged us to accept an unusual X-ray result.

References

1. J.C. North and R. Wolfe, "Ion-Implantation Effects in Bubble Garnets" in Ion-Implantation in Semiconductors and Other Materials, edited by B.L. Crowder (Plenum, New York, 1973).
2. K. Komenou, I. Hirai, K. Asama, and M. Sakai, J. Appl. Phys. 49, 5816 (1978).
3. V.S. Speriosu, H.L. Glass and T. Kobayashi, Appl. Phys. Lett. 34, 539 (1979).
4. H. Jouve, P. Gerard and A. Luc, IEEE. MAG 16, 946 (1980).
5. V.S. Speriosu, B.E. MacNeal and H.L. Glass, Intermag 1980 Conf., Boston, paper 22-4.
6. W. de Roode and J. W. Smits, J. Appl. Phys. 52, 3969 (1981).
7. V.S. Speriosu, J. Appl. Phys. 52, 6094, 1981.
8. Y. Sugita, T. Takeuchi and N. Ohta, MMM Conf. 1981, Atlanta, Paper CA-5.
9. Y. Satoh, M. Okashi, T. Miyashita, and K. Komenou, Int. Conf. on Magnetic Bubbles, Tokyo (1980), paper A-4.
10. G. Suran, H. Jouve and P. Gerard, MMM Conf. 1981, Atlanta, Paper BA-6 (to be published).
11. V.S. Speriosu and C.H. Wilts, MMM Conf. 1981, Atlanta, Paper BA-9.
12. W.H. de Roode and H.A. Algra, J. Appl. Phys. 53, 2507 (1982).
13. H.A. Algra and W.H. de Roode, J. Appl. Phys. 53, 5131 (1982).
14. H. Jouve, J. Appl. Phys. 50, 2246 (1979).
15. T.J. Nelson, R. Wolfe, S.L. Blank, and W.A. Johnson, J.Appl. Phys. 50, 2261 (1979).
16. J.P. Kersusan, P. Gerard, J.P. Gailliard, H. Jouve, IEEE MAG 17, 2917 (1981).
17. W.A. Johnson, J.C. North, and R. Wolfe, J. Appl. Phys. 44, 4753 (1973).
18. H.A. Washburn and G. Galli, J. Appl. Phys. 50, 2267 (1979).
19. H. Jouve and M.T. Delaye, IEEE MAG 16, 949 (1980).
20. P. Gerard, M.T. Delaye, R. Danielou, Thin Solid Films, 88, 75 (1982).

References Con't

21. P. Gerard, P. Martin, R. Danielou, to be published.
22. B.M. Paine, V.S. Speriosu, L.S. Wielunski, H.L. Glass and M-A. Nicolet, Nucl. Instr. Meth. 191, 80 (1981).
23. T. Omi, C.L. Bauer, M.H. Kryder, MMM Conf., Atlanta, 1981, Paper DA-6.
24. R. Wolfe, J.C. North, and Y.P. Lai, Appl. Phys. Lett. 22, 683 (1973).
25. R.F. Soohoo, J. Appl. Phys. 49, 1582 (1978).
26. J.P. Omagio and P.E. Wigen, J. Appl. Phys. 50, 2264, (1979).
27. C.H. Wilts, J. Zebrowski, and K. Komenou, J. Appl. Phys. 50, 5878 (1979).
28. K. Komenou, J. Zebrowski, and C.H. Wilts, J. Appl. Phys. 50, 5442 (1979).
29. H.A. Algra and J.M. Robertson, J.Appl. Phys. 51, 3821 (1980).
30. J.Mada and K. Asama, J. Appl. Phys. 50, 5914, (1979).
31. C.H. Wilts and S. Prasad, IEEE MAG 17, 2405 (1981),
32. G. Suran, R. Krishnan, P. Gerard, and H. Jouve, IEEE MAG 17, 2920 (1981).
33. G. Suran, H. Jouve and P. Gerard, to be published.
34. I. Maartense and C.W. Searle, Appl. Phys. Lett. 34, 115 (1979).
35. P.H. Smit, H.A. Algra, and J.M. Robertson, Appl. Phys. 22, 299 (1980).
36. A.H. Morrish, P.J. Picone and N. Saegusa, Int. Conf. on Magnetic Bubbles, Tokyo 1982.
37. R. Krishnan, S. Visnovski, V. Prosser, and P. Gerard, to be published.
38. K. Ju, R.O. Schwenker, and H.L. Hu, IEEE MAG 15, 1658 (1979).
39. B.E. MacNeal and V.S. Speriosu, J. Appl. Phys. 52, 3935 (1981).
40. See for example, P. Hansen, "Magnetic anisotropy and magnetostriction in garnets", in Physics of Magnetic Garnets edited by A. Paoletti (North-Holland, New York, 1978).
41. B. Hoekstra, F. Van Doveren, and J.M. Robertson, Appl. Phys. 12, 261 (1977).

42. G.P. Vella-Coleiro, Rev. Sci. Instr. 50, 1130 (1979).

43. X. Wang, C.S. Krafft, M.H. Kryder, Int'l. Conf on Magnetic Bubbles, 1982, Tokyo.

44. G.P. Vella-Coleiro, R. Wolfe, S.L. Blank, R. Caruso, T.J. Nelson and V.V.S. Rana, J. Appl. Phys. 52, 2355 (1981).

45. R. Hirko and K. Ju, IEEE MAG 16, 958 (1980).

46. H. Matsutera, S. Esho, and Y. Hidaka, J. Appl. Phys. 53, 2504 (1982).

47. H. Makino, Y. Hidaka and H. Matsutera, Int'l. Conf. on Magnetic Bubbles, 1982, Tokyo.

48. The San Jose, Calif., Laboratory of IBM.

49. See, for example, J.W. Mayer, L. Eriksson and John A. Davies, Ion Implantation in Semiconductors, (A.P., New York, 1970).

50. V.S. Speriosu, B.M. Paine, M-A. Nicolet and H.L. Glass, Appl. Phys. Lett. 40, 604 (1982).

51. G.A. Rozgonyi, P.M. Petroff, and M.B. Panish, Appl. Phys. Lett. 24, 251 (1974).

52. See, for example, W.H. Zachariasen, Theory of X-ray Diffraction in Crystals, (Wiley, New York, 1945).

53. C.H. Wilts, MMM Conf. 1981, Atlanta, paper CA-6.

54. J.F. Gibbons, W.S. Johnson, and S.W. Mylroie, Projected Range Statistics, 2nd ed. (Halstead, New York, 1975).

55. R.D. Pierce, R. Caruso, and C.J. Mogab, J. Appl. Phys. 53, 4480 (1982).

56. A.M. Guzman, C.S. Krafft, X. Wang, M.H. Kryder, to be published.

57. W.L. Johnson, verbal communication.

58 See, for example, R.G. Wilson and D.M. Jamba, Electrochemical Society Meeting, Denver, 1981, abstract 333.

Chapter V

X-ray rocking curve study of Si-implanted GaAs, Si and Ge

A comparative study of the evolution of strain and damage with ion dose.

X-ray rocking curve study of Si-implanted GaAs, Si, and Ge

V. S. Speriosu,[a] B. M. Paine, and M-A. Nicolet
California Institute of Technology, Pasadena, California 91125

H. L. Glass
Rockwell International, Microelectronics Research and Development Center, Anaheim, California 92803

(Received 6 November 1981; accepted for publication 8 January 1982)

Crystalline properties of Si-implanted ⟨100⟩ GaAs, Si, and Ge have been studied by Bragg case double-crystal x-ray diffraction. Sharp qualitative and quantitative differences were found between the damage in GaAs on one hand and Si and Ge on the other. In Si and Ge the number of defects and the strain increase linearly with dose up to the amorphous threshold. In GaAs the increase in these quantities is neither linear nor monotonic with dose. At a moderate damage level the GaAs crystal undergoes a transition from elastic to plastic behavior. This transition is accompanied by the creation of extended defects, which are not detected in Si or Ge.

PACS numbers: 61.10.Fr, 61.70.Tm, 62.20.Fe

The existence of different annealing behavior in ion-implanted amorphized GaAs compared to Si and Ge has been known for some time. In Si and Ge layer regrowth is linear with time and there is good epitaxy.[1-3] In GaAs layer regrowth is nonlinear with time[4] and, independently of ion species, epitaxy is poor.[5] To obtain good electrical activity, implantation in Si and Ge is done at room temperature with doses sufficient to amorphize the material.[6] In GaAs the temperature is held at a few hundred °C in order to prevent amorphization of the layer.[7] Up to the present no substantive evidence has been published concerning the cause of these differences. In this letter we present an x-ray diffraction study of Si-implanted ⟨100⟩ GaAs, Si, and Ge. The results indicate that the evolution of the damage up to amorphousness in GaAs is very different from that in Si and Ge.

⟨100⟩-oriented GaAs, Si, and Ge single crystals, about 5 mm × 5 mm × 0.5 mm in size, highly polished, were implanted with 300-keV Si^+ (in GaAs and Ge) and 230-keV Si^+ (in Si). Implantation was done at room temperature (RT) with a current density of 0.125 $\mu A/cm^2$ and under conditions excluding channeling. Doses ranged from 1×10^{13} atom/cm^2 to 1.2×10^{15} atom/cm^2 for GaAs, 1×10^{13} atom/cm^2 to 7×10^{13} atom/cm^2 for Ge, and 7×10^{13} atom/cm^2 to 7×10^{14} atom/cm^2 for Si. These doses produced modifications in crystal structure measurable by Bragg case double-crystal x-ray diffraction. Well-collimated, low-divergence Fe K_α x rays were obtained with symmetric (400) reflections from nearly perfect ⟨100⟩ monochromators (GaAs for the GaAs and Ge samples, Si for the Si samples). The spot size at the sample was limited to ~1 mm × 1 mm by a set of slits. Typical counting rate for the beam incident on the sample was $\sim10^5$ cps. The diffracted intensity (reflecting power) as a function of angle was measured with a NaI(Tl) detector with pulse height analysis.

Representative diffraction profiles (rocking curves) for the three crystals are shown in Fig. 1. Only the low-angle side of the virgin crystal's Bragg peak is shown. The high-angle side is little changed by implantation. The virgin peak at zero angle, also not shown, is 10 to 100 times more intense than the oscillatory structures shown in the figure. The behavior of the rocking curve with increasing dose for Si [Fig. 1(a)] is similar to that for Ge [Fig. 1(b)]. For both crystals the angular range of nonzero reflecting power increases linearly with dose, the peak farthest from zero angle decreases in relation to other peaks, and the overall reflecting power diminishes. At the highest doses the reflecting power approaches the curve obtained with virgin crystal, indicating that the implanted layer is nearly amorphous. Pronounced

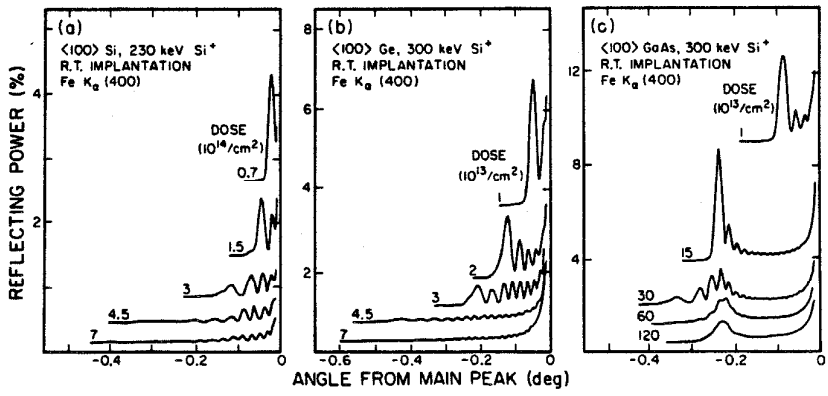

FIG. 1. Rocking curves corresponding to several doses for (a) Si, (b) Ge, and (c) GaAs. The angle is referred to the location of the Bragg peak of virgin crystal. The curves are vertically displaced for clarity. For each curve zero reflecting power occurs at the lowest angle for which the curve is plotted.

[a]IBM predoctoral fellow.

 0003-6951/82/070604-03$01.00

oscillations are maintained over the entire range of doses. The behavior of the GaAs rocking curves [Fig. 1(c)] is very different. As the dose is varied by two orders of magnitude, the range of nonzero reflecting power changes by only a factor of 3. Between 1×10^{13} atom/cm^2 and 1.5×10^{14} atom/cm^2 the principal peak becomes narrower and more intense. Between 1.5×10^{14} atom/cm^2 and 3.0×10^{14} atom/cm^2 the rocking curve broadens, but its shape is different from any obtained in Si or Ge. For doses above 6.0×10^{14} atom/cm^2 the oscillations are smoothed out, although, as indicated by the single peak for the 1.2×10^{15} atom/cm^2 dose, the implanted layer is not amorphous.

The rocking curves of Fig. 1 have been interpreted with the aid of a kinematical model of x-ray diffraction in crystals.[8] The model generates rocking curves for arbitrary depth-dependent distributions of strain, point defects and extended defects. The category of point defects includes individual random atomic displacements as well as highly distorted regions extending over a small number (i.e., one to ten) of unit cells. The category of extended defects covers imperfections that generate small lattice distortions extending over many (i.e., hundreds of) unit cells. Detailed distributions for the strain and the two types of defects are obtainable by fitting experimental rocking curves. The trail-and-error fitting procedure must be performed on a computer. However, several useful parameters are readily found directly from the rocking curve.[8] The total thickness T of the damaged layer is obtained from the most rapid oscillation in the rocking curve, and the maximum strain ϵ_{max} is linearly related to the angle where the rocking curve rises from zero reflecting power.[8] The estimated accuracy for T and ϵ_{max} obtained in this manner is 5%. The number of point defects can be obtained by comparing the areas under rocking curves of damaged and perfect crystals of the same thickness T. Similarly, the presence of extended defects and estimates for their size, amount of random misorientation, and lateral variation of strain are obtainable from the degree of smoothing of the rocking curve.[8,9]

The thickness of the damaged layer is 5200 Å for Si and 5800 Å for Ge and GaAs. Figure 2 shows the maximum strain as a function of dose for the three crystals. Also included is a line of slope one. The maximum strain below the amorphous threshold is around 1% for all three crystals. For Si and Ge, the maximum strain and, by implication, the entire strain distribution, increase nearly linearly with dose. The data for Si and Ge indicate that the number of point defects, describable by a Debye–Waller factor,[8] also increases nearly linearly with dose. Extended defects, as defined above, are absent up to the amorphous threshold.

In GaAs the maximum strain as a function of dose is much more complicated. Here the strain curve can be subdivided into five different regions, as indicated in the figure. Below 10^{13} atom/cm^2 (region I) the strain is assumed to rise linearly with dose. Between 10^{13} atom/cm^2 and $\sim10^{14}$ atom/cm^2 (region II) pronounced saturation sets in. The saturation occurs not only in the maximum strain, but in the entire strain distribution. This is indicated in Fig. 1(c) by the greater sharpness of the principal peak for 1.5×10^{14} atom/cm^2 compared to that for 1×10^{13} atom/cm^2. In region III, between 1×10^{14} atom/cm^2 and 3×10^{14} atom/cm^2, there is a sharp rise in the maximum strain. Between 3×10^{14} atom/cm^2 and $\sim1.2\times10^{15}$ atom/cm^2 (region IV) the maximum as well as the entire strain distribution no longer change with dose. For higher doses (region V) the layer approaches amorphousness. From region I through III, the number of point effects increases with the strain. In region IV it is not clear whether net point defects continue to be created. Instead, extended defects become observable, their density increasing with dose and reaching a value of $\sim1/\mu m^2$ at 1.2×10^{15} atom/cm^2. The rocking curve contains very little information concerning the detailed structure of these extended defects. All that can be said is that they extend throughout most of the implanted layer thickness; the lateral variation in strain is not more than 0.01%, and the variation in orientation is less than ~2 arc min. Attempts to observe the extended defects through x-ray topography have not been successful, probably due to the small variation in orientation compared to the width of the rocking curve.

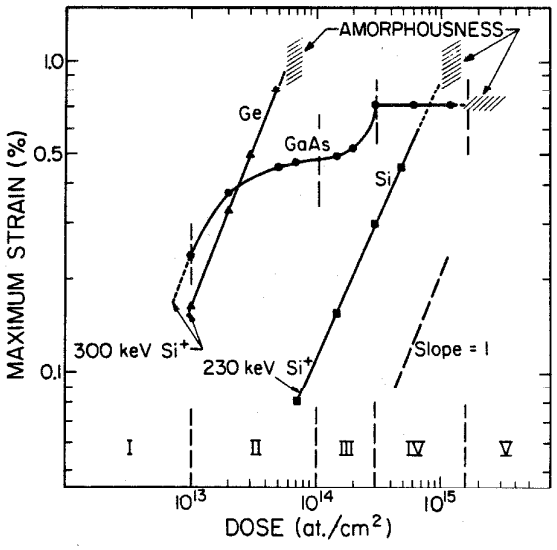

FIG. 2. Maximum strain as a function of dose for Si, Ge, and GaAs. The five dose regions apply to the strain in GaAs.

The mechanism of strain creation in ion-implanted crystals is not very well understood. It has been shown[10] that in garnets the strain distribution is proportional to the energy deposited through nuclear collisions during implantation. It has also been shown[8] that in garnets the strain and damage distributions are proportional to each other. The implanted lattice is constrained by the underlying undamaged crystal to expand only in a direction perpendicular to the surface.[8] This places the implanted layer in lateral compression[11] and gives a Poisson contribution to the strain. As indicated in Fig. 2, for the same strain the dose in Si is about 20 times larger than in Ge. However, the rocking curves show that in both crystals comparable strains correspond to comparable numbers of point defects.

In GaAs pronounced annealing during implantation occurs in region II of Fig. 2. In region III the average strain

reaches its yield value of 0.45%. This number is nearly equal to that obtained[12] for the tensile yield strain of undamaged, externally stressed ⟨110⟩ GaAs. In virgin GaAs the onset of plastic deformation is accompanied by the abrupt creation of 60° dislocations.[12] In lattice-mismatched, epitaxially grown layers, misfit dislocations begin to appear when it is energetically favorable to decrease the macroscopic (coherent) strain at the expense of creating localized distortions.[13] The threshold (yield) strain depends, among other things, on the layer thickness as well as on the depth distribution of the strain.[14]

In region IV of Fig. 2 the strain in GaAs no longer changes with the dose. This is perhaps due to a combination of annihilation of point defects at sinks such as extended defects and/or to the relaxation of strict lattice match with the underlying crystal. The deposited energy goes into the creation of extended defects whose density increases with the dose.

The results presented above imply a different structure of the damaged layer for amorphized GaAs compared to Si and Ge. This difference can explain the observed differences in annealing behavior. For Si and Ge, starting at the deep end of the damage deposition curve, the elastic strain and the number of point defects rise uniformly up to the amorphous threshold.[15] With this structure one expects that, during post-implantation annealing, the regrowth is layer by layer using the good seed at the deep end of the damge, thus resulting in relatively good epitaxy.

In GaAs the implanted layer consists of three regions. At the deep end of the damage the strain is elastic and only point defects are present. Between the elastically strained and amorphous regions is a plastically deformed region. This region, containing extended defects, will present a barrier to epitaxial regrowth. The existence of this barrier depends on whether or not the yield strain is reached, regardless of how it is reached. Thus the regrowth of the amorphized layer will be independent of the implanted ion species, as observed.[5] At elevated implantation temperatures, the rate of self-annealing is probably sufficiently high such that for all doses the strain will remain below the yield value (regions I and II of Fig. 2). Thus the plastically deformed region does not develop. It is probably for this reason that elevated temperature implantations of dopants in GaAs give best regrowth and electrical properties.[7] For room-temperature implantation, the elastically strained portion of the layer will regrow epitaxially. It is in fact observed that amorphized GaAs layers show an initial epitaxial regrowth at the buried crystal/amorphous interface.[5] Subsequently however, the quality of the epitaxy will be impaired by the presence of the plastically deformed region, resulting in a highly defected regrown layer.[16] When implantation does not fully amorphize the layer, good epitaxy is observed.[17] We attribute this to strain levels that are too small to induce plastic deformation. If the implanted layer is thin enough, good regrowth is observed even after full amorphization.[18] We propose that this occurs because for thin layers the yield strain is large,[14] with the result that amorphization occurs before the threshold strain for plastic deformation is reached.

We thank E. Babcock for performing the ion implantation, S. S. Lau for helpful discussions, and L. A. Moudy for technical assistance. This work was supported in part by the Advanced Research Agency of the Department of Defense and was monitored by the Air Force Office of Scientific Research under Contract No. 49620-Tl-C-0087.

[1]L. Csepregi, J. W. Mayer, and T. W. Sigmon, Physics Lett. **54A**, 157 (1975).
[2]L. Csepregi, J. W. Mayer, and T. W. Sigmon, Appl. Phys. Lett. **29**, 92 (1976).
[3]J. W. Mayer, L. Csepregi, J. Gyulai, I. Nagy, G. Mezey, P. Revesz, and E. Kotai, Thin Solid Films **32**, 303 (1976).
[4]K. Gamo, T. Inada, J. W. Mayer, F. H. Eisen, and C. G. Rhodes, Rad. Eff. **33**, 85 (1977).
[5]M. G. Grimaldi, B. M. Paine, M-A. Nicolet, and D. K. Sadana, J. Appl. Phys. **52**, 4038 (1981).
[6]See for example, J. W. Mayer, L. Eriksson, and J. A. Davies, *Ion Implantation in Semiconductors* (Academic, New York, 1970), p. 198.
[7]J. S. Harris, F. H. Eisen, B. Welch, J. D. Haskell, R. D. Pashley, and J. W. Mayer, Appl. Phys. Lett. **21**, 601 (1972).
[8]V. S. Speriosu, J. Appl. Phys. **52**, 6094 (1981).
[9]V. S. Speriosu, B. E. MacNeal, and H. L. Glass, Intermag. 1980 Conf., Boston, paper 22-4 (unpublished).
[10]B. E. MacNeal and V. S. Speriosu, J. Appl. Phys. **52**, 3935 (1981).
[11]E. P. EerNisse, Appl. Phys. Lett. **18**, 581 (1971).
[12]H. Booyens, J. S. Vermask, and G. R. Proto, J. Appl. Phys. **49**, 5435 (1978).
[13]G. A. Rozgonyi, P. M. Petroff, and M. B. Panish, Appl. Phys. Lett. **24**, 251 (1974).
[14]C. A. Ball and C. Laird, Thin Solid Films **41**, 307 (1977).
[15]V. S. Speriosu, B. M. Paine, M.-A. Nicolet, and H. L. Glass (to be published).
[16]S. S. Kular, B. J. Sealy, K. G. Stephans, D. Sadana, and G. R. Booker, Solid-State Electron. **23**, 831 (1980).
[17]J. S. Williams and M. W. Austin, Nucl. Instr. Meth. **168**, 307 (1980).
[18]M. G. Grimaldi, B. M. Paine, M. Maenpaa, M.-A. Nicolet, and D. K. Sadana, Appl. Phys. Lett. **39**, 70 (1981).

Chapter VI

Conclusion

A method for determining depth profiles of lattice parameter and damage level (or structure factor) in monocrystals was presented. The kinematical interpretation of x-ray diffraction in such crystals enables rapid computer calculation of rocking curves corresponding to arbitrary distributions. The distributions for a particular case are obtained by fitting the experimental rocking curve. The sensitivity of the calculated curve to variations in the strain distribution shows that local precision of 2% of peak strain and depth resolution of 50 to 200A are obtainable. The sensitivity to changes in the magnitude of the local structure factor is 10%.

The technique was applied to ion-implanted garnets and semiconductors and to a multilayer laser structure. In terms of sensitivity, information content and experimental facility the rocking curve method compares well with Rutherford backscattering, presently the major tool for studying damage in implanted crystals. Since a variation in chemical composition usually results in a corresponding variation in lattice parameter, the rocking curve may be able to provide as much information as other surface analysis techniques, such as Secondary Ion Mass Spectroscopy (SIMS) or Auger Electron Spectroscopy (AES), both of which are destructive. Future work will show whether or not this is the case.

A drawback of the present x-ray technique is its reliance on trial-and-error fitting procedures. The rocking curve yields directly parameters such as peak strain, total thickness and thickness-averaged structure factor. However, due to lack of phase detection, the curve cannot be simply inverted to yield the corresponding distributions of strain and structure factor. For arbitrary distributions, with some knowledge of the processing steps involved in growing or modifying the crystal, an experienced operator can usually converge to an excellent fit in 20 or fewer iterations. The distribution obtained in this manner has a higher precision than the initial trial distribution based on external information. If this information is not available or if the rocking curve is particularly complex, one can resort to etching and reconstruct the profiles as described in Chapter II. For unimodal distributions created by ion-implantation, the structure of the rocking curve is sufficiently simple to permit determination of strain and damage profiles without external inputs. A major improvement of the technique would be the development of an algorithm guaranteeing convergence to satisfactory fits of arbitrary rocking curves. Work towards this goal is in progress.

Magnetic and crystalline profiles of ion-implanted garnet were obtained by combination of ferromagnetic resonance and x-ray diffraction. The method developed by Wilts was used to analyze FMR spectra corresponding to implantation

with elements (Ne, He, and H) commonly utilized in magnetic bubble memory devices and covering a wide range of doses. Prior to this work, the complexity of the theory of resonance in nonuniform films and also the complexity of experimental FMR spectra had discouraged detailed understanding. By demanding quantitative interpretation of every detail of these spectra we have obtained results with a degree of clarity and certainty never attained before. Much of what we found is at variance with established beliefs. In neon and helium implanted garnet the initial source of the change in uniaxial anisotropy is the strain - not the destruction of growth-induced anisotropy. With increasing strain the uniaxial anisotropy saturates and decreases to zero - it does not merely saturate. Because of this decrease in the region of maximum strain and damage, the field for resonance of the principal surface mode in FMR cannot be used to measure any magnetic property in this region. By comparing the profile of uniaxial anisotropy with the strain profile for hydrogen implantation, we have shown conclusively that the unusually large anisotropy is due to chemical effects - not to qualitatively different damage caused by hydrogen implantation.

We have accomplished these things merely by asking that x-ray rocking curves and ferromagnetic resonance spectra make sense - not by doing any new experiments.